

**Nuclear dependence of the
transverse-single-spin asymmetry for
forward neutron production in
polarized $p+A$ collisions at
 $\sqrt{s_{NN}} = 200 \text{ GeV}$**

Minjung Kim

Under the supervision of
Professor Seonho Choi

A dissertation submitted to
the Graduate Faculty of Seoul National University
in partial fulfillment of the requirement
for the Degree of Doctor of Philosophy

Department of Physics and Astronomy
The Graduate School of Natural Sciences
Seoul National University
Seoul, KOREA

February, 2019

Abstract

In high-energy hadron collisions, most of the energy is distributed in the forward region (the scattering angle is nearly zero). Therefore, studying forward particle production mechanisms is important for understanding overall particle production. However, because of small momentum transfers, pQCD is not applicable, therefore, forward particle production mechanisms are not well understood. Such low momentum transfer interactions at high-energy collisions are studied by the Regge theory.

In case of the forward neutron production in $p+p$, cross-sections were measured at ISR and PHENIX, and the transverse-single-spin asymmetry A_N was measured at IP12 and PHENIX. The results had been well explained by the π and $a_1(1260)$ exchange model in the Regge framework. This model predicted moderate nuclear dependence on A_N .

In 2015, the Relativistic Heavy Ion Collider (RHIC) had the polarized protons and nuclei collisions for the first time in the world. The first measurement of nuclear dependence on A_N in forward neutron production in $p+A$ collisions are presented. Surprisingly, the result contradicts with the Regge theory prediction. The A_N has a strong nuclear dependence: compared to $p+p$ collisions, the sign of A_N is flipped and its magnitude becomes three times larger in $p+Au$. Further measurements to pin down the characteristics of the unknown mechanisms and discussion of different neutron production processes which may explain the result are introduced.

Keywords: Forward neutron, Spin Asymmetry, Proton-Nucleus Collision, RHIC, PHENIX, Regge, UPC

Student Number: **2014-30999**

Contents

| | | |
|----------|---|-----------|
| 1 | Introduction | 2 |
| 1.1 | Background story | 2 |
| 1.2 | A surprise | 4 |
| 1.3 | Afterward | 5 |
| 1.4 | Thesis organization | 5 |
| 2 | Regge theory | 7 |
| 2.1 | Derivation of a scattering amplitude form | 8 |
| 2.2 | Regge trajectory $\alpha(t)$ | 13 |
| 2.3 | Regge phenomenology parameters | 13 |
| 2.3.1 | Inclusive production | 15 |
| 2.4 | Pomeron | 17 |
| 3 | Forward neutron production in $p+p$ | 20 |
| 3.1 | Cross section and one pion exchange (OPE) model | 21 |
| 3.2 | Transverse spin asymmetry A_N | 24 |
| 3.2.1 | Definition of A_N | 24 |
| 3.2.2 | A_N measurements of pion in $p+p$ | 25 |
| 3.2.3 | IP12 experiment | 26 |
| 3.2.4 | PHENIX experiment | 28 |
| 3.2.5 | Regge theory: π and a_1 interference | 28 |
| 3.2.6 | Nuclear dependence | 31 |

| | |
|---|-----------|
| 4 Experiment | 32 |
| 4.1 RHIC | 32 |
| 4.1.1 Overview | 32 |
| 4.1.2 Polarized proton source | 33 |
| 4.1.3 Ion source | 34 |
| 4.1.4 Accelerator chain | 35 |
| 4.1.5 RHIC storage rings | 35 |
| 4.1.6 Spin pattern | 36 |
| 4.1.7 Depolarization and the Siberian snake | 37 |
| 4.1.8 Spin rotator | 39 |
| 4.1.9 Polarimeters | 40 |
| 4.2 PHENIX | 48 |
| 4.2.1 Beam-Beam Counter | 48 |
| 4.2.2 Zero-Degree Calorimeter | 48 |
| 4.2.3 Electronics and Trigger | 53 |
| 4.3 Run-15 operating conditions | 53 |
| 5 Analysis | 56 |
| 5.1 Overview | 56 |
| 5.2 Summary of the previous background study for $p+p$ and the analysis cut | 58 |
| 5.2.1 Previous simulation study | 58 |
| 5.2.2 Analysis cut | 60 |
| 5.3 Data set | 61 |
| 5.3.1 Run quality assurance | 61 |
| 5.3.2 Initial event selection | 62 |
| 5.3.3 Dead channel | 63 |
| 5.3.4 Polarization | 64 |
| 5.4 Calibration | 66 |
| 5.4.1 ZDC pedestal calibration | 66 |

| | | |
|--------|--|-----|
| 5.4.2 | SMD position reconstruction | 67 |
| 5.4.3 | ZDC gain | 74 |
| 5.4.4 | CV MIP peak calibration | 75 |
| 5.5 | BBC taggings | 77 |
| 5.6 | Energy spectra of neutron samples | 79 |
| 5.7 | p_T spectra | 81 |
| 5.8 | Asymmetry measurement | 84 |
| 5.8.1 | Raw asymmetry ϵ_N | 84 |
| 5.8.2 | Polarization normalized asymmetry A_N^{fit} | 84 |
| 5.9 | Background subtraction | 94 |
| 5.9.1 | Proton background simulation for $p+p$ | 94 |
| 5.9.2 | $p+A$ collisions | 98 |
| 5.9.3 | Background fraction | 101 |
| 5.9.4 | “Effective” background fraction | 101 |
| 5.9.5 | Signal and background asymmetries, A^S and A^B | 104 |
| 5.10 | Smearing correction | 105 |
| 5.10.1 | $d\sigma/dp_T$ shape dependence | 107 |
| 5.10.2 | $d\sigma/dx_F$ shape dependence | 109 |
| 5.10.3 | SMD threshold dependence | 109 |
| 5.10.4 | Position resolution | 110 |
| 5.10.5 | $A_N(p_T)$ shape dependence | 111 |
| 5.10.6 | Final C_{smear} and its uncertainty | 119 |
| 5.10.7 | Final asymmetry A_N | 120 |
| 5.11 | Systematic uncertainties | 121 |
| 5.11.1 | Background | 121 |
| 5.11.2 | Smearing | 122 |
| 5.11.3 | Polarization | 123 |
| 5.11.4 | Beam position | 124 |
| 5.11.5 | Calibrations | 130 |

| | |
|--|------------|
| 6 Result | 131 |
| 7 Discussions | 137 |
| 7.1 Regge theory model | 137 |
| 7.2 Electromagnetic process | 138 |
| 7.3 Other contributors? | 145 |
| 8 Conclusion | 147 |
| A Appendix | 159 |
| A.1 Asymmetry calculations | 159 |
| A.1.1 Fill/run raw asymmetry ε_N | 159 |
| A.1.2 Fill/run polarization P | 160 |
| A.1.3 Measured asymmetry A_N^{fit} | 160 |
| A.1.4 Charged background subtracted asymmetry A_N^S for Run-08 | 162 |
| A.1.5 Run-15 A_N^S | 163 |
| A.1.6 A_N | 164 |

List of Figures

| | | |
|-----|--|----|
| 1.1 | Left-right asymmetry of forward neutron production: $p+p$ result, $p+Au$ naive prediction, and $p+Au$ result, from the left to right. The trajectory of the neutron in each drawing indicates its preferred side (left or right) when the proton spin is up. | 3 |
| 2.1 | The contours for the Watson-Sommerfeld transform (from C to C') and a Regge pole $\alpha_i^\eta(t)$ on the complex angular momentum (l) plane. | 11 |
| 2.2 | The Chew-Frautschi plot. Regge trajectories of multiple (ρ, ω, f_2, a_2) families [1]. Each family shares the same quantum numbers except spin. Note that Regge trajectories of multiple families shown in this plot are almost degenerated. | 14 |
| 2.3 | A simple reggeon exchange diagram drawn with couplings. | 15 |
| 2.4 | Triple-Regge diagram for inclusive process. | 16 |
| 2.5 | Compiled total cross section data (CERN and Tevatron [1]) as a function of center of mass energy. Regge theory fits $\sigma \sim s^{\alpha(0)-1}$ are overlaid [1]. | 18 |
| 3.1 | Forward neutron production spectra in $p+p \rightarrow n + X$ [2]. | 22 |
| 3.2 | Forward neutron production spectra in $p+p \rightarrow n + X$ [3]. | 22 |
| 3.3 | One pion exchange (OPE) models for forward neutron production in $p+p$ | 23 |

| | | |
|------|--|----|
| 3.4 | A_N of inclusive pion produced from polarized $p+p$ collisions in at various center of mass energies [4] | 25 |
| 3.5 | A_N of inclusive pion produced from polarized $p+p$ collisions in at various center of mass energies [4] | 26 |
| 3.6 | A_N vs. p_T for EM-jets [5]. The row corresponds to the number of photon, and the A_N is measured as a function of jet p_T . . . | 27 |
| 3.7 | Forward neutron A_N as a function of ϕ measured at IP12 [6]. . | 27 |
| 3.8 | Forward neutron A_N as a function of x_F measured at PHENIX [3]. Top: neutron inclusive, bottom: requiring inelastic event tagging trigger (BBC, see Sec. 4.2.1). | 29 |
| 3.9 | Diagram for the interference between π and a_1 exchanges [7]. . | 29 |
| 3.10 | Forward neutron A_N as a function of p_T . The PHENIX data is drawn with the theory [7]. The A_N comes from the interference between π and a_1 exchanges generate dominantly. | 30 |
| 4.1 | RHIC complex with the beam polarization apparatus. | 33 |
| 4.2 | A layout of the Optically-Pumped Polarized H ⁻ Ion Source (OPPIS): 1 - atomic hydrogen injector; 2- pulsed He-gaseous ionizer cell; 3-optically pumped Rb-vapor cell; 4-Sona-transition; 5-Na-jet ionizer cell [8]. | 34 |
| 4.3 | The Siberian snake operation at $\gamma=25$: the top left plot shows the beam orbit; the top right plot shows the Magnetic field component; the bottom left plot shows the spin component (see $S_{x,z}$ remains unchanged and S_y flips); and the bottom right plot shows the evolution of the vertical polarization inside the Siberian snake. In each plot, the z -axis is along the beam orbit, x and y is the horizontal and vertical [9]. | 39 |
| 4.4 | The side (left) and the top (right) view of the H-jet polarimeter [10]. | 43 |

| | | |
|------|---|----|
| 4.5 | The analyzing power A_N of proton-Carbon scattering in the Coulomb-Nuclear Interference (CNI) region measured at the AGS with the 21.7 GeV/c polarized proton beam [11]. The data is drawn with theory curves [12]. The solid and dotted lines are the theory curve with hadronic spin-flip and its uncertainty, respectively. The dashed line is theory curve without hadronic spin-flip amplitude. The polarization of the data is measured by the H-jet polarimeter. | 44 |
| 4.6 | The proton-Carbon (pC) polarimeter layout (right) [9]. | 45 |
| 4.7 | PHENIX detectors. | 49 |
| 4.8 | PHENIX magnetic field lines. | 50 |
| 4.9 | BBC | 50 |
| 4.10 | A layout of the ZDC and BBC. | 51 |
| 4.11 | Schematic drawing of the ZDC component. | 52 |
| 4.12 | ZDC location and beam orbits of proton (blue) beam and heavy-ion (yellow) beam in the special stores used for this analysis; the z -axis shows the nominal beam direction, and the dashed line represents the zero-degree neutron trajectory. DX and D0 are the RHIC beam bending dipole magnets. | 54 |
| 4.13 | Beam orbits in p +Au physics stores (left), and p +Au local pol dedicated stores (right). Angles are not in scale. | 55 |
| 5.1 | PYTHIA+GEANT: Event structure of main particles (neutrons, photons, and protons) at the ZDC acceptance at 5 GeV threshold. | 59 |
| 5.2 | Polarization of blue beam in Run-08 (top) and Run-15 (down) $p+p$ | 65 |
| 5.3 | ZDC LED pedestal scan results for all eight channels. ADC distributions with ZDC PMT HV of ch1, ch2, ch5, and ch6 off. In this figure, total 8 channels are shown since the south ZDC, which is not used in this analysis, is also included | 66 |

| | | |
|------|---|----|
| 5.4 | SMD pedestal fit. | 68 |
| 5.5 | Eq. 5.2 fitting result of a strip. | 69 |
| 5.6 | X distribution with different threshold cut in Run-15 p+p ZDC inclusive sample. 40 is the threshold of asymmetry analysis. | 70 |
| 5.7 | Before the SMD gain matching. The plots shows the pedestal subtracted ADC distributions of all channels before (after) the gain matching. | 71 |
| 5.8 | After the SMD gain matching. | 72 |
| 5.9 | X position of ZDC \otimes BBC-tag samples of Run-08 and Run-15. . | 73 |
| 5.10 | Y position of ZDC \otimes BBC-tag samples of Run-08 and Run-15. . | 73 |
| 5.11 | ZDC energy distribution at $r < 2.0$ cm of neutron identified events from ZDC inclusive sample. | 74 |
| 5.12 | Charge veto counter (CV) events. | 75 |
| 5.13 | Number of fired PMT distribution of BBC south (left), and BBC north (right) after neutron analysis cut. Figures are for $p+p$, $p+Al$, and $p+Au$ from the top to the bottom. | 78 |
| 5.14 | $p+p$. ZDC energy spectra for inclusive (red), ZDC \otimes BBC-tag (green), and ZDC \otimes BBC-veto (blue). The plots in the left show raw yield, and normalized yields (the integral of a histogram is 1) are drawn in the right for better comparison of shapes between trigger samples. The species of colliding particles are written in each plot. All of the asymmetry analysis cuts in Sec. 5.2.2 except the energy cut are applied in these data. | 80 |
| 5.15 | p_T spectrum of neutron sample. | 82 |
| 5.16 | Neutron yield of each p_T bin. p_T spectrum is equally binned: . | 83 |
| 5.17 | Neutron distribution in $p+Au$ collisions shown with 16 azimuthal bins for raw asymmetry $\epsilon_N(\phi)$ calculation. | 85 |
| 5.18 | A_N^{fit} histogram of each collision system, for ZDC inclusive, ZDC \otimes BBC-tag, and ZDC \otimes BBC-veto samples in Run-15 from the top to bottom. Fit results are in table 5.2. | 86 |

| | |
|--|----|
| 5.19 A_N^{fit} histogram of each collision system, for ZDC \otimes p-dir BBC--veto \otimes A-dir BBC-tag | 87 |
| 5.20 A_N^{fit} histogram of each collision system, for ZDC \otimes p-dir BBC-tag \otimes A-dir BBC-veto | 87 |
| 5.21 A_N^{fit} for different measured p_T bins, Run-15 $p+p$ | 88 |
| 5.22 A_N^{fit} for different measured p_T bins, Run-15 $p+Al$ | 89 |
| 5.23 A_N^{fit} for different measured p_T bins, Run-15 $p+Au$ | 90 |
| 5.24 A_N^{fit} of measured p_T samples of Run-15 $p+p$, $p+Al$, and $p+Au$ from the top to bottom. | 91 |
| 5.25 A_N^{fit} of measured p_T samples, Run-08 $p+p$ | 92 |
| 5.26 A_N^{fit} of measured p_T samples, Run-08 $p+p$ with charge veto cut. | 93 |
| 5.27 PYTHIA+GEANT simulation: x-distribution of the showers in the ZDC reconstructed by the SMD for protons (red), neutrons (blue), and all particles (black) for pp collisions in ZDC inclusive (left) ZDC \otimes BBC-tag (middle) and ZDC \otimes BBC-veto triggered samples. | 95 |
| 5.28 PYTHIA+GEANT simulation: x-distribution of the showers in ZDC reconstructed by the SMD for protons from elastic and single diffractive scatterings leaving beam proton intact (left), and hard scattering and double diffractive processes (right). | 95 |
| 5.29 PYTHIA+GEANT simulation: x-distribution of the showers in ZDC reconstructed by SMD in ZDC \otimes BBC-tag sample (red) and ZDC (ZDC \otimes BBC-veto) sample on the top (bottom) plot; spectra are normalized to the same value in the range $x < 1$ cm. | 97 |
| 5.30 Proton trajectory in pp setup (left) and in pA setup (right) for unscattered beam proton (black), elastically scattered by 4 mrad (red), and by 5 mrad (green); dashed line is for neutron trajectory. | 99 |

| | |
|--|-----|
| 5.31 (Left) Differential cross section for proton elastic scattering vs scattering angle θ ; (Right) Elastically scattered proton contribution in ZDC acceptance, in arb. units, as a function of the minimal angle θ_0 (see text for explanation); pp (black), pAl (red) and pAu (green). | 100 |
| 5.32 Run8 pp: x-distribution of the showers in ZDC reconstructed by SMD in BBC&ZDC sample (red) and ZDC (ZDC&noBBC) sample on the left (right) plot; spectra are normalized to the same value in the range $x < 1$ cm. | 101 |
| 5.33 Run15 pp: x-distribution of the showers in ZDC reconstructed by SMD in BBC&ZDC sample (red) and ZDC (ZDC&noBBC) sample on the left (right) plot; spectra are normalized to the same value in the range $x < 1$ cm. | 102 |
| 5.34 Run8 pp: x-distribution of the showers in ZDC reconstructed by SMD in BBC&ZDC sample (red) and ZDC (ZDC&noBBC) sample on the left (right) plot, after charge veto cut is applied; spectra are normalized to the same value in the range $x < 1$ cm. | 102 |
| 5.35 Comparison between original (true) p_T of neutron and measured (reconstructed) p_T | 106 |
| 5.36 Run-08 ZDC \otimes BBC-tag (left) and (right) r distribution of data (black) and simulation with exponential p_T slope parameter $b = -3.5$ (GeV/c) $^{-1}$ (red) and $b = -4.8$ (GeV/c) $^{-1}$ (blue). . . | 107 |
| 5.37 r distribution of neutron data samples of ZDC \otimes BBC-tag (left) and ZDC \otimes BBC-veto (right) of three collision systems. | 108 |
| 5.38 p_T distribution of neutron sample with simulation with different exponential p_T slope parameter b | 108 |
| 5.39 Distribution of the number of fired SMD hits in x-direction: Run15 pp data (black) vs MC (red) with SMD energy threshold 1 MeV (left), 3 MeV (middle), and 6 MeV (right). | 110 |

| | |
|--|-----|
| 5.40 Distribution for the energy fraction in the maximal energy strip: Run15 pp data (black) vs MC (red) assuming no cross talk (left) and 10% cross talk (right). | 111 |
| 5.41 Input asymmetries. Left: parametrized as $A_N(p_T) \sim p_T^\alpha$ with $\alpha = 0$ (magenta), 0.5 (yellow), 0.8 (blue), 1.0 (green), 1.5 (red) and 2.0 (black). Right: threshold value $p_{T0} = 0.15$ (magenta), 0.12 (yellow), 0.10 (blue), 0.07 (green), 0.05 (red) and 0 (black). | 112 |
| 5.42 Measured asymmetries obtained from simulation. | 112 |
| 5.43 Smearing correction, C_{smear}^{ideal} (blue) and C_{smear}^{actual} (red) vs slope parameter α in the parameterization $A_N(p_T) \sim p_T^\alpha$ (left), and threshold parameter p_{T0} (right). | 113 |
| 5.44 Left: asymmetry vs p_T^{meas} , data (black) vs MC calculation with different α in parameterization $A_N(p_T) \sim p_T^\alpha$: $\alpha = 0$ (magenta), 0.5 (yellow), 0.8 (blue), 1.0 (green), 1.5 (red) and 2.0 (black); MC curves are normalized to get the same average asymmetry as in data; data are Run 15 pp ZDC \otimes BBC-tag triggered sample. Right: χ^2 vs α | 114 |
| 5.45 Left: asymmetry vs p_T^{meas} , data (black) vs MC calculation with different α in parameterization $A_N(p_T) \sim p_T^\alpha$: $\alpha = 0$ (magenta), 0.5 (yellow), 0.8 (blue), 1.0 (green), 1.5 (red) and 2.0 (black); MC curves are normalized to get the same average asymmetry as in data; data are Run 8 pp ZDC \otimes BBC-tag triggered sample. Right: χ^2 vs α | 114 |
| 5.46 Left: asymmetry vs p_T^{meas} , data (black) vs MC calculation with different α in parameterization $A_N(p_T) \sim p_T^\alpha$: $\alpha = 0$ (magenta), 0.5 (yellow), 0.8 (blue), 1.0 (green), 1.5 (red) and 2.0 (black); MC curves are normalized to get the same average asymmetry as in data; data are Run 15 pp ZDC triggered sample. Right: χ^2 vs α | 115 |

-
- 5.47 Left: asymmetry vs p_T^{meas} , data (black) vs MC calculation with different α in parameterization $A_N(p_T) \sim p_T^\alpha$: $\alpha = 0$ (magenta), 0.5 (yellow), 0.8 (blue), 1.0 (green), 1.5 (red) and 2.0 (black); MC curves are normalized to get the same average asymmetry as in data; data are Run 8 pp ZDC triggered sample. Right: χ^2 vs α 115
- 5.48 Left: asymmetry vs p_T^{meas} , data (black) vs MC calculation with different α in parameterization $A_N(p_T) \sim p_T^\alpha$: $\alpha = 0$ (magenta), 0.5 (yellow), 0.8 (blue), 1.0 (green), 1.5 (red) and 2.0 (black); MC curves are normalized to get the same average asymmetry as in data; data are Run 15 pAu ZDC \otimes BBC-veto triggered sample. Right: χ^2 vs α 116
- 5.49 Left: asymmetry vs p_T^{meas} , data (black) vs MC calculation with different α in parameterization $A_N(p_T) \sim p_T^\alpha$: $\alpha = 0.8$ (magenta), 1.0 (yellow), 1.5 (blue), 2.0 (green), 2.5 (red) and 3.0 (black); note, the range of α here is different from all previous plots; MC curves are normalized to get the same average asymmetry as in data; data are Run 15 pAl ZDC \otimes BBC-veto triggered sample. Right: χ^2 vs α 116
- 5.50 Left: asymmetry vs p_T^{meas} , data (black) vs MC calculation with different threshold value p_{T0} in representation of $A_N(p_T)$ as a step-function: $p_{T0} = 0.15$ (magenta), 0.12 (yellow), 0.10 (blue), 0.07 (green), 0.05 (red) and 0 (black); MC curves are normalized to get the same average asymmetry as in data; data are Run 15 pp ZDC \otimes BBC-tag triggered sample. Right: χ^2 vs p_{T0} . 117

| | |
|--|-----|
| 5.51 Left: asymmetry vs p_T^{meas} , data (black) vs MC calculation with different threshold value p_{T0} in representation of $A_N(p_T)$ as a step-function: $p_{T0} = 0.15$ (magenta), 0.12 (yellow), 0.10 (blue), 0.07 (green), 0.05 (red) and 0 (black); MC curves are normalized to get the same average asymmetry as in data; data are Run 8 pp ZDC \otimes BBC-tag triggered sample. Right: χ^2 vs p_{T0} . | 117 |
| 5.52 Left: asymmetry vs p_T^{meas} , data (black) vs MC calculation with different threshold value p_{T0} in representation of $A_N(p_T)$ as a step-function: $p_{T0} = 0.15$ (magenta), 0.12 (yellow), 0.10 (blue), 0.07 (green), 0.05 (red) and 0 (black); MC curves are normalized to get the same average asymmetry as in data; data are Run 8 pp ZDC triggered sample. Right: χ^2 vs p_{T0} . | 118 |
| 5.53 Left: asymmetry vs p_T^{meas} , data (black) vs MC calculation with different threshold value p_{T0} in representation of $A_N(p_T)$ as a step-function: $p_{T0} = 0.15$ (magenta), 0.12 (yellow), 0.10 (blue), 0.07 (green), 0.05 (red) and 0 (black); MC curves are normalized to get the same average asymmetry as in data; data are Run 15 pAu ZDC \otimes BBC-veto triggered sample. Right: χ^2 vs p_{T0} . | 118 |
| 5.54 Left: asymmetry vs p_T^{meas} , data (black) vs MC calculation with different threshold value p_{T0} in representation of $A_N(p_T)$ as a step-function: $p_{T0} = 0.15$ (magenta), 0.12 (yellow), 0.10 (blue), 0.07 (green), 0.05 (red) and 0 (black); MC curves are normalized to get the same average asymmetry as in data; data are Run 15 pAl ZDC \otimes BBC-veto triggered sample. Right: χ^2 vs p_{T0} . | 119 |
| 5.55 Beam position scan for Run-08 $p + p$. | 125 |
| 5.56 Beam position scan for Run-15 $p + p$. | 126 |
| 5.57 Beam position scan for Run-15 $p+Al$. | 127 |
| 5.58 Beam position scan for Run-15 $p+Au$. | 128 |

| | | |
|-----|---|-----|
| 6.1 | Forward neutron A_N in $p+A$ collisions for $A = 1$ (p), 27 (Al) and 197 (Au), for ZDC inclusive (red), ZDC \otimes BBC-tag (green) and ZDC \otimes BBC-veto (blue) triggered samples; color bars show systematic uncertainties, statistical uncertainties are smaller than the marker size; Additional 3% scale uncertainty (not shown) is from polarization normalization. Some data points are shifted horizontally for better visibility. | 133 |
| 6.2 | The illustration of BBC tagged samples. From the top to bottom, ZDC \otimes BBC-tag, ZDC \otimes BBC-veto, ZDC \otimes p-dir BBC--veto \otimes A-dir BBC-tag, and ZDC \otimes p-dir BBC-tag \otimes A-dir BBC-veto. The sum of these four samples becomes the ZDC inclusive sample. As indicated in the figure, the neutron A_N is analyzed by the right side ZDC, where the polarized proton beam is heading. | 134 |
| 6.3 | Forward neutron A_N as a function of atomic mass number in $p+A$ collisions like Fig. 6.1. Two more BBC tagged samples, ZDC \otimes p-dir BBC-veto \otimes A-dir BBC-tag (magenta) and ZDC \otimes BBC-tag (light blue) are analyzed. See the text for analysis differences. | 135 |
| 7.1 | Theory calculation [13] of the forward neutron A_N as a function of atomic mass number A drawn with the data points. The green (red) data points and the dashed (solid) theory curve correspond to the ZDC \otimes BBC-tag (ZDC \otimes p-dir BBC--veto \otimes A-dir BBC-tag) sample. | 138 |
| 7.2 | A_N (=T) of π^+ production in $\gamma p \rightarrow \pi^+ n$ reaction as a function of pion production polar angle in the γp center of mass frame for various photon beam energies. Plots show a comparison with the MAID2007 [14] (red) and the Osaka-Argonne [15] (blue) models with the PHOENICS data [16] (black dots). . . | 140 |

| | | |
|-----|---|-----|
| 7.3 | The invariant mass spectrum [17] of the $\pi^0 + p$ at $t < 10^{-3} \text{GeV}/c^2$. Peaks correspond to the $\Delta(1232)$ and $N(1520)$ resonances. The A_N is zero at the region I ($W < 1.36 \text{ GeV}/c^2$), whereas $A_N \sim 60\%$ at the region II ($1.36 < W < 1.52 \text{ GeV}/c^2$), interference region of those two resonances. | 141 |
| 7.4 | $A_N (=T)$ of π^0 production in $\gamma p \rightarrow \pi^+ n$ reaction as a function of pion production polar angle in the γp center of mass frame for various photon beam energy (center of mass energy is shown in each plot). Plots show a comparison with the combined data from the particle data group (PDG) and the Osaka-Argonne model [15]. | 142 |
| 7.5 | The A_N calculation from the UPC simulation ($\gamma^* p \rightarrow \pi^+ n$) using the MAID2007 model [18]. | 144 |
| 7.6 | Feynman diagrams of two interfering mechanisms which generate A_N for neutron production in $p+A$ hadronic process (a), EM process (b), and for hadronic and EM processes in elastic $p+p$ scattering (c). | 146 |
| 7.7 | Example of hadronic processes which can have final state as same as those of EM processes, therefore may interfere. . . . | 146 |

List of Tables

| | | |
|-----|---|-----|
| 4.1 | The Run-15 spin patterns. B and Y represent the Blue and Yellow beams, respectively. + (-) means the beam polarization direction is up (down) at the polarimeters in the 12'o clock interaction point. Those up and downs of 24 bunches repeat through the whole bunches in a fill. | 37 |
| 4.2 | Beam orbits in mrad. This measurement is done with the special stores. | 55 |
| 5.1 | The number of analyzed events. | 64 |
| 5.2 | Run-08 A_N^{fit} summary with statistical uncertainty and systematic uncertainty from polarization only. The “done” in the “CV cut” column means that the charge veto cut is applied. . . | 92 |
| 5.3 | Summary of background fraction | 103 |
| 5.4 | A^S and A^B of $p + p$ Run-08. | 104 |
| 5.5 | A^S of $p + p$ Run-15, with A^B from Tab. 5.4. | 104 |
| 5.6 | $C_{\text{smear}}^{\text{ideal}} / C_{\text{smear}}^{\text{actual}}$ correction and uncertainties assuming $A_N(p_T) \sim p_T^\alpha$ | 113 |
| 5.7 | $C_{\text{smear}}^{\text{ideal}} / C_{\text{smear}}^{\text{actual}}$ correction and uncertainties assuming $A_N(p_T) = \text{const}$ for $p_T > p_{T0}$ and 0 for $p_T < p_{T0}$ | 113 |
| 5.8 | Forward neutron A_N values and statistical uncertainties in polarized proton-nucleus collisions. | 120 |

| | | |
|------|---|-----|
| 5.9 | Systematic uncertainties from background. | 122 |
| 5.10 | Systematic uncertainties from smearing correction. | 123 |
| 5.11 | Systematic uncertainties from polarization. | 124 |
| 5.12 | Systematic uncertainties from beam position. | 129 |
| 5.13 | Systematic uncertainties from calibrations. | 130 |
| 6.1 | A_N for forward neutron production in $p+p$, $p+Al$, and $p+Au$ collisions, for ZDC inclusive, ZDC \otimes BBC-tag, and ZDC \otimes BBC-veto samples. | 132 |
| 6.2 | Raw yield of each sample in million. Background fractions are not subtracted. From $p+p$ to $p+Au$, one can clearly notice that the fraction of the ZDC \otimes BBC-veto sample becomes increased, whereas the fraction of the ZDC \otimes BBC-tag and the ZDC \otimes p-dir BBC-veto \otimes A-dir BBC-tag samples becomes decreased. The fraction of the ZDC \otimes p-dir BBC-tag \otimes A-dir - BBC-veto sample is not changed significantly. | 136 |

Chapter 1

Introduction

This thesis is based on a kind of serendipity, so I will first describe the background story and the surprise, which contain inevitably a partial spoiler of the final result.

1.1 Background story

This thesis research was conducted in the PHENIX experiment at RHIC. RHIC is the only hadron collider in the world which can run polarized (both transversely and longitudinally) proton beams as well as multiple species of nuclei from light to heavy ones, and PHENIX is a multi-purpose experiment which measures various particles. From 2001, RHIC had provided both longitudinally and transversely polarized $p+p$ collisions, which enables to study the proton helicity structure and transverse spin phenomena. In such experiments, the beam polarization at the collision point must be verified that it is in the intended direction. Therefore, PHENIX operates a local polarimeter to measure the polarization direction at the PHENIX experimental area during

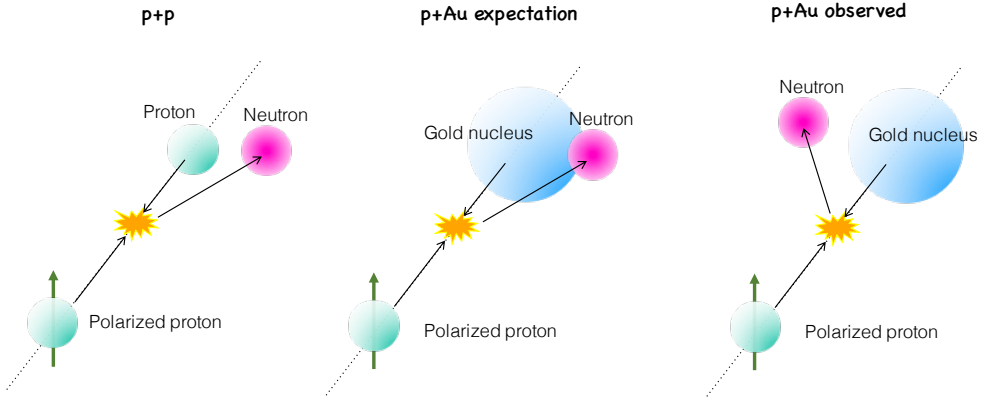


Figure 1.1: Left-right asymmetry of forward neutron production: $p+p$ result, $p+Au$ naive prediction, and $p+Au$ result, from the left to right. The trajectory of the neutron in each drawing indicates its preferred side (left or right) when the proton spin is up.

whole polarized proton runs.

Forward neutron as a local polarimeter in polarized $p+p$

The PHENIX local polarimeter is comprised of hadron calorimeters and a hodoscope for energy and position measurements of neutrons, and located at the very forward rapidity ($\eta < 6.8$), covering the zero-degree. In $p+p$ collisions at RHIC energies, neutrons at the nearly zero-degree region (forward neutrons) are produced at the *right* side more when the polarization direction of the beam is up (see Fig. 1.1 left), and this production mechanism has been well understood (see Sec. 3). The local polarimeter utilizes this property, so that the beam polarization direction is monitored in real time by the observed left-right asymmetry, which is associated with the transverse component of the polarization (see Sec. 4.1.9 for the principle of operation). Consequently, the local polarimeter had been providing successfully this essential information in spin researches at PHENIX for a decade.

Forward neutron in the first polarized $p+A$ collision: a local polarimeter, as in $p+p$

In 2015, RHIC had transversely polarized proton and unpolarized Al/Au collisions at $\sqrt{s_{NN}} = 200$ GeV. This was the unprecedented high-energy polarized proton and nucleus collisions in the world. The main $p+A$ program was to study nuclear effects based on the partonic picture. However, the mechanism of the forward neutron production is based on a kind of meson exchange picture, due to the small momentum transfer of forward kinematics. Therefore, the major motivation of forward neutron A_N measurement in $p+A$ was to monitor the proton beam polarization according to a naive prediction that the forward neutron left-right asymmetry would have moderate nuclear dependence (see Sec. 3.2.6), as depicted in the middle of Fig. 1.1. However...

1.2 A surprise

When we switched from $p+p$ to $p+Au$ collisions, we observed unexpected behavior in the real time monitoring of the local polarimeter. The left-right preference of the forward neutron was flipped, i.e. in $p+Au$, neutrons preferred the *left* side more when the proton spin is up (see Fig. 1.1 right). This result was unbelievable in the beginning, thus it required cross-checks by offline analysis in order to examine whether a monitoring software of the local polarimeter reversed the left-right preference in $p+Au$ by mistake or not. If it were from a mistake, either falsely flipped left-right in the neutron position reconstruction or upside down proton spin information as opposed to the real one in the monitoring software can be a cause.

Consequently, the offline analysis proved the reversed left-right preference between $p+Au$ and $p+p$ was real. 1) the left and right of $p+Au$ was confirmed by one $p+Au$ run which happened to have a significant beam scrapping back-

ground on the left side of the detector, and this was observed in the offline analysis software, 2) the intended and measured (by outside of PHENIX) beam polarization direction was consistent with both monitoring and offline analysis software, and the spin rotators, which control the beam polarization direction locally at the PHENIX experimental hall, was off, and 3) the offline analysis software reproduced the previously measured $p+p$ result. Hence, we confirmed that the observed left-right preference was real, which indicated there was unknown mechanism in forward neutron production.

1.3 Afterward

We started to discuss the origin of the nuclear dependence. In order to pin down the characteristic of the unknown production mechanism, we investigated mainly two mutually exclusive subsets of inclusive neutron sample. We obtained crucial hints from the above measurement, then we found a strong candidate of the neutron production process in $p+A$. To confirm our explanation, further analysis is planned. In addition, we also suggest unexplored mechanisms which might be relevant. The details are described in the rest part of this thesis.

1.4 Thesis organization

Since this research was not originally planned with a specific strong physics motivation, this thesis is written with a slightly unusual flow of contents at the beginning and the end. In the early part this thesis, our understanding of forward neutron production in high-energy $p+p$ based on the Regge theory is explained. For that, first, I will introduce the Regge theory, and then describe forward neutron experiments and theoretical un-

derstandings in the Regge theory. Then in the end of this thesis, the possible explanation of the surprising result is discussed.

Chapter 2

Regge theory

The Regge theory [19] is a specialized meson¹ exchange model, first introduced by T. Regge [19] in 1959. To explain the Regge theory, knowing where the Regge theory is in the chronological table of physics would help understanding. Before the Regge theory, various hadrons were the most elementary particles we ever knew, and the early strong interaction law was described by a meson exchange, first suggested by Yukawa (1930s). After the Regge theory, the quark model (1964) was suggested and the Quantum chromodynamics (QCD) was established through 1970s.

The characteristic of the Regge theory comparing to the QCD and the meson exchange is as follows. Unlike the QCD starts from the fundamental force law, the Regge theory studies the mathematical properties of scattering amplitudes and tries to get the maximum information of the strong interaction from those properties. In comparison with the meson exchange, the force carrier described in the Regge theory is “Regge trajectory”, which are

¹Force carrier is not always a meson in the Regge theory, but meson exchange sounds familiar.

not a fixed species of meson, but a group of particles. This idea gives simple phenomenology fit applicable without knowing information of exchanged particles, then enables obtaining the information of exchanged particles from fits.

In the Regge theory, the mathematical properties of the scattering amplitudes are studied based on the S -matrix framework. The scattering amplitude forms are obtained by extending the partial wave expansion of integer angular momentum l to the complex l -plane in the high-energy limit (more specifically, at $s \gg |t|, m^2$, where m represent mass of scattered particles, and s and t are Mandelstam variables). Since the Regge theory works at low $|t|$ where perturbative QCD is not applicable, it is still useful at high-energy (colliding particles are relativistic $\sqrt{s} \gg mc^2$) experiments. The Regge theory is widely studied for total and elastic cross sections, low- x structure function form in deep inelastic scattering, and diffractive (process involving low Q^2 strong interaction, or Pomeron exchange (see Sec. 2.4) productions.

This chapter is to introduce the Regge theory basics before we apply it in the next chapter. In the following sections, derivation of the Regge theory scattering amplitude and the Regge theory parameters are explained followed. Then generalized treatment of inclusive processes is introduced. Introduction of Pomeron is the major achievement of the Regge theory, and sometimes it will be mentioned. Therefore, I will introduce Pomeron in the end of this section.

2.1 Derivation of a scattering amplitude form

This section is dedicated to derivation of Eq 2.14 as a scattering amplitude form for two particles ($2 \rightarrow 2$) processes. Its physical meaning is explained in Sec. 2.3, after introducing the Regge trajectory in Sec. 2.2.

General properties of S -matrix

In the relativistic S -matrix theory, the S -matrix is a linear operator which connects between the initial state $|i\rangle$ at $-\infty$ and the final state $|f\rangle$ at $+\infty$ of a scattering process

$$|f\rangle = S|i\rangle. \quad (2.1)$$

The S -matrix element S_{if} is defined as

$$S_{if} \equiv \langle f | S | i \rangle. \quad (2.2)$$

Then the probability to find the final state $|f\rangle$ from the initial state $|i\rangle$ becomes

$$P_{i \rightarrow f} = |S_{if}|^2. \quad (2.3)$$

In principle, once we know all of the S matrix elements, we can reconstruct any measurement result. The S -matrix element can be written as

$$S_{if} = \delta_{if} + i(2\pi)^4 \delta^4(p_f - p_i) A(i \rightarrow f) \quad (2.4)$$

where δ_{if} is for no interaction, $\delta^4(p_f - p_i)$ is for four-momentum conservation, and $A(i \rightarrow f)$ is the relativistic scattering amplitude (“relativistic” will be often omitted unless necessary). The initial state is a two particle states and the final state can be any number of particles. The differential cross section for a reaction with n particles at the final state is

$$d\sigma = \frac{1}{\Phi} |A(i \rightarrow f_n)|^2 d\Pi_n \quad (2.5)$$

where Φ is the incident flux and $d\Pi_n$ is the phase space factor for n particles

of the final state. Then the total cross section becomes

$$\sigma_{tot} = \frac{1}{\Phi} \sum_n \int d\Pi_n |A(i \rightarrow f_n)|^2. \quad (2.6)$$

Partial-wave expansion

In case of a two-particles to two-particles process ($1+2 \rightarrow 3+4$), the scattering amplitude becomes a function of two independent Lorentz invariant variables. Like the partial-wave analysis in non-relativistic quantum mechanics, the relativistic amplitude can be decomposed into the basis of the angular momentum l as

$$A(s, t)_{1+2 \rightarrow 3+4} = \sum_{l=0}^{\infty} (2l + 1) a_l(s) P_l(\cos \theta), \quad (2.7)$$

where s and t are Mandelstam variables, θ is the scattering angle, which becomes $\cos \theta = 1 + \frac{2t}{s}$ at high-energy $s \gg m_{1,2,3,4}^2 \sim m^2$, P_l is a Legendre polynomial, and $a_l(s)$ is the partial wave amplitude. Then in the crossed t -channel, the scattering amplitude can be written as

$$A(s, t)_{1+\bar{3} \rightarrow \bar{2}+4} = \sum_{l=0}^{\infty} (2l + 1) a_l(t) P_l \left(1 + \frac{2s}{t} \right). \quad (2.8)$$

From crossing symmetry, both $A(s, t)_{1+2 \rightarrow 3+4}$ and $A(s, t)_{1+\bar{3} \rightarrow \bar{2}+4}$ can be used to describe physical reactions of s -channel at $s > 4m^2$ and t -channel at $t > 4m^2$.

Parametrization using the complex angular momentum

Figure 2.1 shows the complex l -plane drawn with contours and simple poles, which will be explained later. In the Regge theory, we assume that there is a unique function $a(l, t)$ on the complex- l plane for fixed t which becomes $a(l, t) = a_l(t)$ for integer l . Then Eq. 2.8 becomes equivalent to

$$A(s, t) = -\frac{1}{2i} \oint_C dl \frac{(-1)^l}{\sin \pi l} (2l + 1) a(l, t) P\left(l, 1 + \frac{2s}{t}\right) \quad (2.9)$$

for the blue contour C at Fig. 2.1, where $P\left(l, 1 + \frac{2s}{t}\right)$ is a hypergeometric function, which becomes $P_l\left(1 + \frac{2s}{t}\right)$ for integer l .

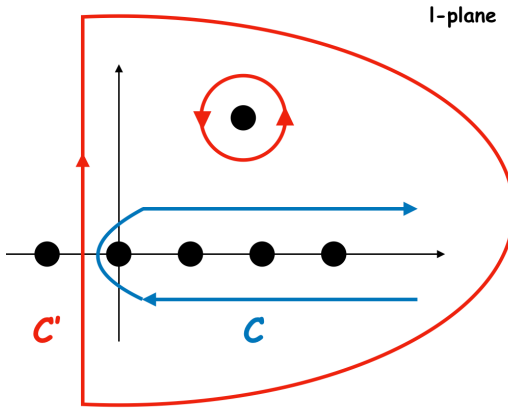


Figure 2.1: The contours for the Watson-Sommerfeld transform (from C to C') and a Regge pole $\alpha_i^\eta(t)$ on the complex angular momentum (l) plane.

Let's change the contour from C to infinitely large half circle runs through $-1/2 - i\infty$ to $-1/2 + i\infty$ C' (the Watson-Sommerfeld transformation), and let's assume that $a(l, t)$ has a simple pole, or a Regge pole, at $l=\alpha(t)$, therefore,

$$a(l, t) \sim \frac{\beta(t)}{l - \alpha(t)} \quad (2.10)$$

at the vicinity of the pole, where $\beta(t)$ is the residue. Then Eq 2.9 becomes

$$A(s, t) = \frac{(-1)^{\alpha(t)}}{\sin \pi \alpha(t)} (2\alpha(t) + 1) \beta(t) P\left(\alpha(t), 1 + \frac{2s}{t}\right) \quad (2.11)$$

$$- \frac{1}{2i} \int_{-1/2-i\infty}^{-1/2+i\infty} dl \frac{(-1)^l}{\sin \pi l} (2l + 1) a(l, t) P\left(l, 1 + \frac{2s}{t}\right). \quad (2.12)$$

In the $s \gg t, m^2$ limit, $P\left(l, 1 + \frac{2s}{t}\right) \sim \left(\frac{s}{t}\right)^l$, then the integral in Eq. 2.11 becomes zero. Then more simply, Eq. 2.11 becomes

$$A(s, t) \sim \frac{(-1)^{\alpha(t)}}{\sin \pi \alpha(t)} (2\alpha(t) + 1) \beta(t) \left(\frac{s}{t}\right)^{\alpha(t)}. \quad (2.13)$$

Actually, there can be more poles at $l=\alpha_1(t), \alpha_2(t), \dots$, however, because of $\left(\frac{s}{t}\right)^{\alpha_i(t)}$ contribution in Eq. 2.13, only one $\alpha_i(t)$ with the largest $\text{Re } \alpha_i(t)$ will survive at $s \gg t$.

In fact, $a(l, t)$ is not uniquely determined. $a(l, t)$ can be uniquely determined for even $a^{+1}(l, t)$ and odd $a^{-1}(l, t)$ angular momenta separately, then everything should be separately done for even and odd l from Eq. 2.8. This gives a modification of $(-1)^{\alpha(t)}$ to $(\xi + e^{-i\pi\alpha(t)})$, where $\xi = 1(-1)$ for even (odd) angular momentum. Then Eq. 2.13 should be modified to

$$A(s, t) \underset{s \gg t, m^2}{\sim} \beta(t) \frac{e^{-i\pi\alpha(t)} \pm 1}{\sin \pi \alpha(t) s^{\alpha(t)}} \quad (2.14)$$

where $\beta(t)$ incorporates a residue of the Regge pole, t dependence, and all constants. Although we started from the t -channel scattering amplitude, we assume that the function form is valid at s -physical ($s > 4m^2$) channel.

We have dealt with a pole as a singularity. However, the singularity in the complex l -plane is not only limited to poles (Regge pole). There are also branch points, which corresponds to multi-reggeons exchanges (Regge cut).

2.2 Regge trajectory $\alpha(t)$

To remind, $\alpha(t)$ in Eq. 2.14 is the angular momentum. Unlike a meson exchange has a fixed angular momentum, the angular momentum in the Regge theory moves continuously as t changes. This $\alpha(t)$ is called as the “Regge trajectory” or “reggeon”.

$\alpha(t)$ can be obtained from Chew-Frautschi plots, which draws a graph of the spin J of a particle against its mass square M^2 , as Fig. 2.2 [1]. One can notice that a *family* of particles with the same quantum numbers except spin happens to lie on a straight line.^{II} The function α_{family} connecting this line of each family is called a Regge trajectory. Each trajectory is named by the lowest mass particle of the family.

To see Fig. 2.2 more closely, it seems those four (ρ, ω, f_2, a_2) Regge trajectories are degenerated. In the view of the QCD with string models (for example, [21]) of hadrons, a meson is a rotating quark-antiquark pair connected by a massless string, and the rotation generates the spin of the hadron. Then the universality of the slopes of the Regge trajectories is explained by a universal string tension, i.e. linear QCD potential.

Coming back to Eq. 2.14, in this scattering amplitude form, the Regge trajectory $\alpha(t)$ in this equation represents the group of exchanged particles. Therefore, the difference between the Reggeon exchange and the meson exchange seems to be clear by now.

2.3 Regge phenomenology parameters

^{II} There is a discussion that this “quasi”-linearity is broken for the most recent particles data [20]. However, those particles are not relevant with this thesis.

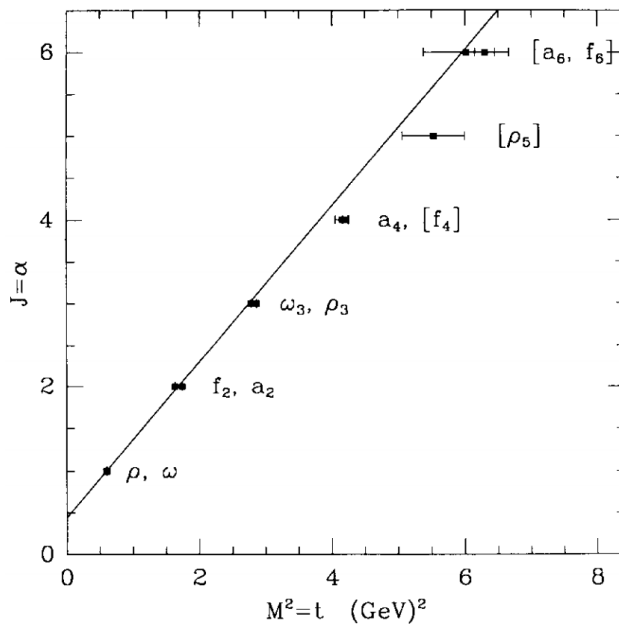


Figure 2.2: The Chew-Frautschi plot. Regge trajectories of multiple (ρ, ω, f_2, a_2) families [1]. Each family shares the same quantum numbers except spin. Note that Regge trajectories of multiple families shown in this plot are almost degenerated.

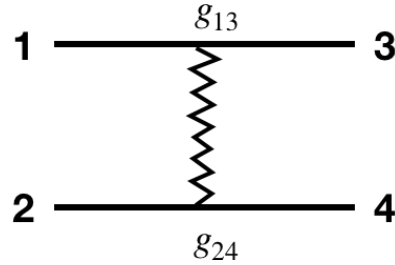


Figure 2.3: A simple reggeon exchange diagram drawn with couplings.

In Sec. 2.1, we derived two particles process and obtained Eq. 2.14 as the scattering amplitude form. Such process is depicted in Fig. 2.3, a Reggeon exchange diagram. To simplify and factorize Eq. 2.14, it becomes

$$A(s, t) \sim \beta(t)\eta(t)s^{\alpha(t)}. \quad (2.15)$$

Here are the properties of each parameter.

- $\alpha(t)$ is the Regge trajectory and we know it from Chew-Frautschi plot (real)
- $\beta(t) = g_{13}(t)g_{24}(t)$ factorizes by the couplings at each vertex of the diagram and we know nothing about its form, only accessible from data (real)
- $\eta(t) = [e^{-i\pi\alpha(t)} \pm 1]/[\sin \pi\alpha(t)s^{\alpha(t)}]$ is a signature factor (complex), $+(-)$ sign for the Reggeon with even (odd) value of spin, and we know if we know $\alpha(t)$

2.3.1 Inclusive production

In case of the single inclusive process, $1 + 2 \rightarrow 3 + X$, the scattering amplitude is calculated by so called the triple-Regge diagram (see Fig. 2.4). Due to simplified diagram, the inclusive cross section can be calculated out of

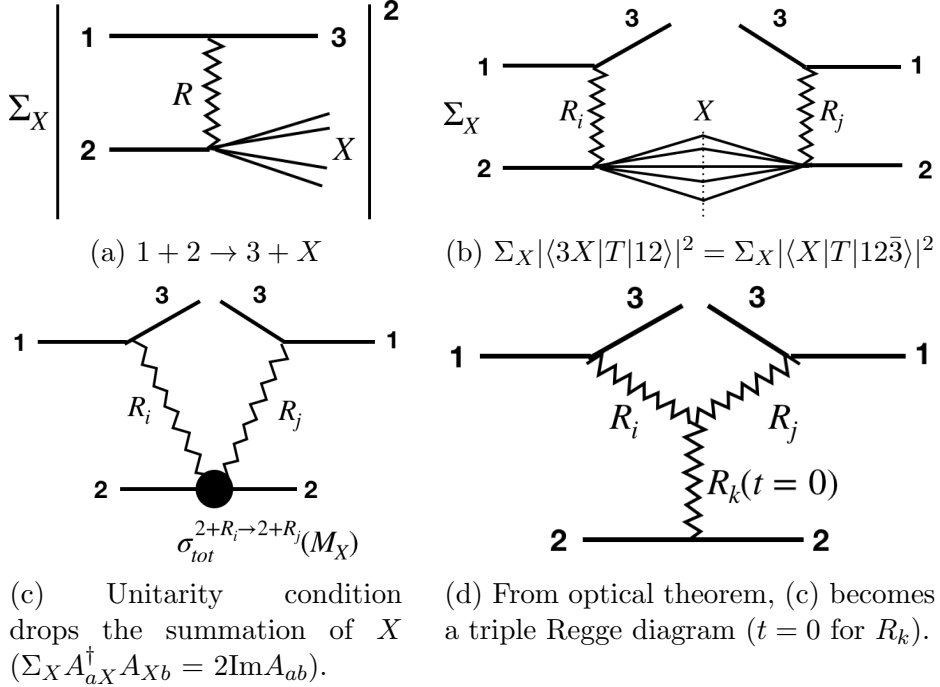


Figure 2.4: Triple-Regge diagram for inclusive process.

the scattering amplitude form for two particles processes. This gives a cross section form as

$$\frac{d^2\sigma}{dM^2dt} = \Sigma_{ijk} g_{13}^i(t) g_{13}^{j*}(t) g_{22}^k(0) g^{ijk}(t) \eta_i(t) \eta_j^*(t) s^{\alpha_i(t)+\alpha_j(t)-1} (M^2)^{\alpha_k(0)-\alpha_i(t)-\alpha_j(t)}, \quad (2.16)$$

where M is the invariant mass of the system X . If we obtain vertex couplings other data, the rest terms can be trivially calculable. Using $x_F \approx 1 - M^2/s$ at $x_F \rightarrow 1$ (x_F is the Feynman x , defined as $2p_\parallel/\sqrt{s}$, where p_\parallel is the longitudinal momentum in the center of mass frame), for $R_i=R_j$, Eq. 2.16 can be simplified as

$$\frac{d^2\sigma}{dx_F dt} \sim G_{iik}^2(t) |\eta_i(t)|^2 (1 - x_F)^{\alpha_k(0)-2\alpha_i(t)} \sigma_{tot}^{2R_i}(M^2). \quad (2.17)$$

2.4 Pomeron

One of the important object developed in the Regge theory is the Pomeron. Pomeron has vacuum quantum numbers, and it is in charge of elastic scatterings. We are trying to implement the Pomeron in QCD as (at least) two gluon exchange, which conserves quantum numbers in reactions. The Pomeron is suggested while explaining the total cross section data.

With the optical theorem, Eq. 2.15 gives the total cross section form written as

$$\sigma_{tot} = \frac{1}{s} \text{Im}A(s, t=0) \sim s^{\alpha(0)-1}. \quad (2.18)$$

If more than one pole contribute,

$$\sigma_{tot} \sim \sum_i A_i s^{\alpha_i(0)-1}, \quad (2.19)$$

where A_i is a constant fit parameter of i -th Reggeon exchange. The intercept $\alpha(0)$ of low mass mesons are below 1, therefore, the decrease of total cross section as increase of s can be expected. Before high-energy data became available, there was a prediction that at high-energy limit, charge exchange would be vanished and the isospin conserving reaction will be increased (Pomeranchuk, Okun 1956). Also, there was a consistent prediction that if the cross section does not decreases at high-energy limit, the scattering process should be dominantly from the vacuum quantum number exchanges [22].

Figure 2.5 [1] shows the compiled total cross section data of $p + \bar{p}$ and $p + p$ collisions (left) and $\pi + p$ collisions (right) as a function of center of mass energy. Experimentally, the total cross section can be measured [23] as

$$\sigma_{tot} = \frac{16\pi}{1 + \rho^2} \frac{(dN_{el}/dt)|_{t=0}}{N_{el} + N_{in}} \quad (2.20)$$

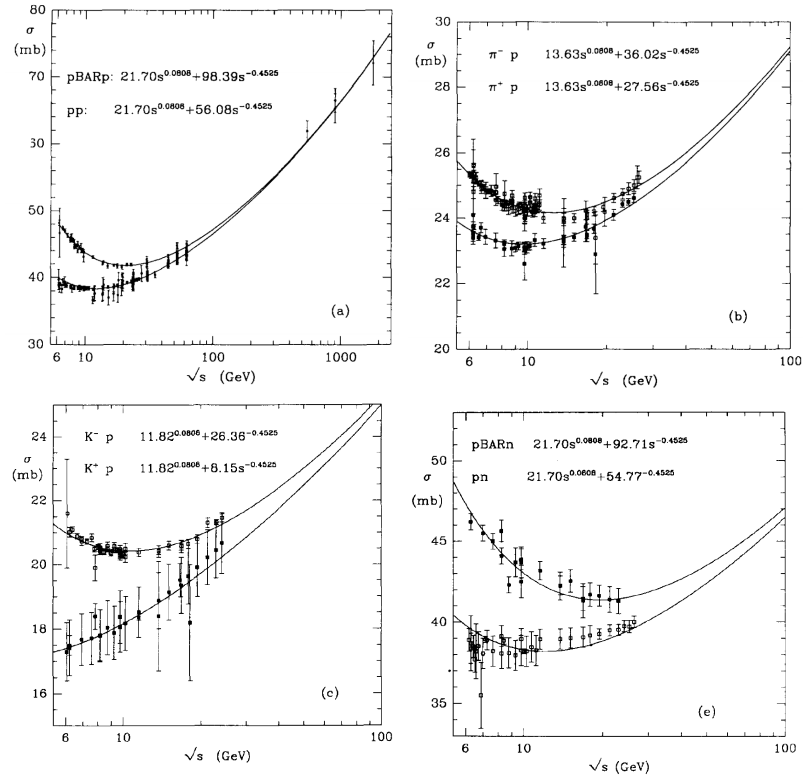


Figure 2.5: Compiled total cross section data (CERN and Tevatron [1]) as a function of center of mass energy. Regge theory fits $\sigma \sim s^{\alpha(0)-1}$ are overlaid [1].

where the ρ -parameter is $\rho = \frac{\text{Re}A(s,t=0)}{\text{Im}A(s,t=0)} = -\frac{\xi + \cos \pi\alpha(t)}{\sin \pi\alpha(t)} \sim 0.15$ in the interested region, $N_{el(in)}$ are number of elastic (inelastic) events tagged by detectors. From Fig 2.5, the total cross sections of all particles increase as their energies increase. As a result, the Regge theory fits (Eq. 2.18) requires a new object whose intercept $\alpha(0)$ is 1.08. This particle is the Pomeron. From the fit in Fig 2.5, one can notice that all total cross sections are well explained by two Regge trajectory values, one from the Pomeron ($\sim s^{0.08}$) and the other $\sim s^{-0.45}$ is shared by multiple Regge trajectories of low mass mesons (see Fig. 2.2), and as energy increases, reactions become dominated by the Pomeron exchange.

Chapter 3

Forward neutron production in $p+p$

Studying particle production mechanisms and measurements of cross sections provide a fundamental test of QCD and particle production models, and their inputs are crucial in various Monte Carlo simulation development. In case of forward particle production at high-energy hadron collisions, its understanding is important because most of particles are produced at forward. This is particularly crucial in ultrahigh-energy cosmic ray physics because direct measurement of ultrahigh-energy cosmic ray is difficult due to its small flux, so primary cosmic ray particles are indirectly detected through air shower measurement, and the interpretation of data depends on forward particle production models for primary particles scattering off nuclei in the air [24–26]. In spite of its importance, however, understanding forward particle production mechanisms is difficult because pQCD is not applicable due to small momentum transfer in this kinematics. Therefore, experimental data are essential in forward production model developments.

The inclusive forward neutron production at high-energy has been studied for $p + p \rightarrow n + X$ at ISR [27, 28] and PHENIX [3], and for $e + p \rightarrow n + X$ at HERA [29–32]. The dominant process for such production is pion exchange. Since pion exchange is primary in low momentum transfer hadronic interaction, studying properties of pion exchange in the Regge framework has significant importance. This makes studies of forward neutron production crucial. Based on the Regge theory, cross section data of those experiment had been well explained by the one pion exchange (OPE) model [7, 33–35].

In case of the forward neutron production in $p+p$, transverse-single-spin asymmetry, A_N (see Sec. 3.2.1 for definition), was measured at IP12 [6] and PHENIX [3] for the forward neutron production in $p+p$. Both experiments observed large A_N values, order of several percents. This result contradicts with the OPE model, which predicted almost zero asymmetry [7]. In order to explain the large asymmetry data, the OPE model introduced a_1 exchange in addition to OPE [7]. The interference between the π and a_1 exchange amplitudes generates the large A_N . As a result, the A_N data were well explained. Therefore, forward neutron production mechanism in $p+p$ is well understood.

3.1 Cross section and one pion exchange (OPE) model

Figure 3.1 shows the forward neutron cross sections in $p+p$ collisions as a function of x_F measured for various center of mass energies ($\sqrt{s} = 20\text{--}50$ GeV) and p_T (0-0.6 GeV/ c) [2].

The coverage of $p_T = 0$ bin corresponds to the 0 ± 1 mrad. One can notice that for the $p_T = 0$ bin, the cross section has a peak around $x_F \sim 0.8$. This cannot be explained by the neutron production as fragmentation from parton-parton scatterings in the QCD framework, which gives a cross section

3.1. CROSS SECTION AND ONE PION EXCHANGE (OPE) MODEL 22

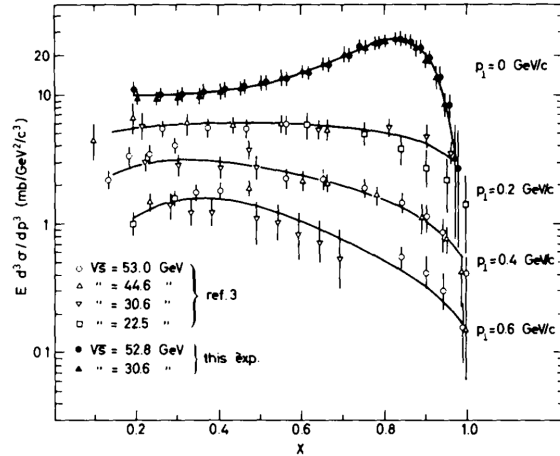


Figure 3.1: Forward neutron production spectra in $p+p \rightarrow n + X$ [2].

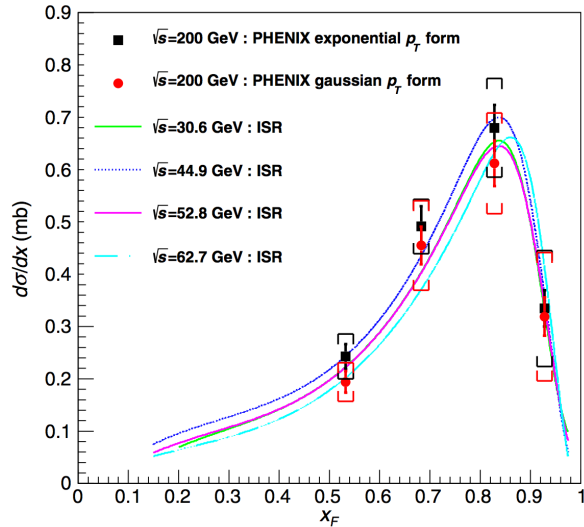


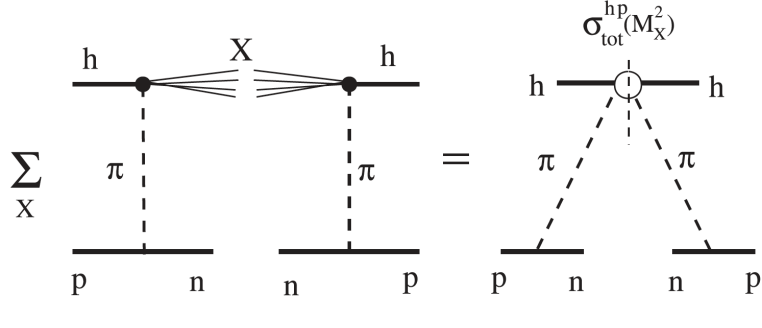
Figure 3.2: Forward neutron production spectra in $p+p \rightarrow n + X$ [3].

decreases as a function of x_F and p_T . The cross section measurement for the same scattering angle was done at PHENIX [3] at $\sqrt{s} = 200$ GeV. The result is shown in Fig. 3.2 drawn with the ISR result. The cross section $d\sigma/dx_F$ from both PHENIX and ISR show x_F scaling. For $p_T \sim 0$, t becomes a function of x_F , then x_F scaling is explained by Eq. 2.17.

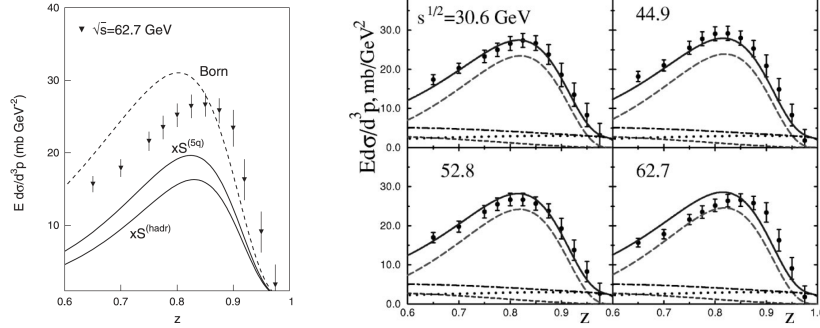
From simple calculation of t for the diagram shown in Fig 3.3, $-t$ at the

3.1. CROSS SECTION AND ONE PION EXCHANGE (OPE) MODEL 23

pion mass square corresponds to $x_F \sim 0.8$. Therefore, we can notice that pion exchange is in charge of the very forward neutron production, and in fact, one pion exchange (OPE) models [7, 34, 36] well explain the forward neutron cross section data. These are shown in Fig. 3.3.



(a) Graphical representation of OPE [36] (see Fig. 2.4).



(b) Born approximation (dashed curve) and with corrections absorption of initial or final state particles (two solid lines for different correction models) drawn with ISR data [36]. Absorptive effect suppress cross section.

(c) Pion exchange (long dashed curve) plus contribution from backgrounds (dotted lines from ρ , a_2 , and dashed line for $p \rightarrow \Delta \rightarrow n$ [34].

Figure 3.3: One pion exchange (OPE) models for forward neutron production in $p+p$.

3.2 Transverse spin asymmetry A_N

3.2.1 Definition of A_N

The transverse single spin asymmetry A_N is defined as

$$A_N = \frac{d\sigma^\uparrow - d\sigma^\downarrow}{d\sigma^\uparrow + d\sigma^\downarrow}, \quad (3.1)$$

where the arrow indicates the polarization direction of a beam or a target. From rotational symmetry, this can be also expressed as left-right asymmetry

$$A_N = \frac{d\sigma_L^\uparrow - d\sigma_L^\downarrow}{d\sigma_L^\uparrow + d\sigma_L^\downarrow} = \frac{d\sigma_L^\uparrow - d\sigma_R^\uparrow}{d\sigma_L^\uparrow + d\sigma_R^\uparrow}. \quad (3.2)$$

For an inclusive process $a + b \rightarrow c + X$, using transition matrix, A_N can be written as

$$\begin{aligned} A_N &= \frac{\sum_X |\langle cX|T|\uparrow\rangle|^2 - \sum_X |\langle cX|T|\downarrow\rangle|^2}{\sum_X |\langle cX|T|\uparrow\rangle|^2 + \sum_X |\langle cX|T|\downarrow\rangle|^2} \\ &= \frac{-2\text{Im} \sum_X \langle cX|T|-\rangle \langle +|T^\dagger|cX\rangle}{\sum_X |\langle cX|T|+\rangle|^2 + \sum_X |\langle cX|T|-\rangle|^2} \end{aligned} \quad (3.3)$$

where $+/-$ is the helicity states, with $|\uparrow\rangle = \frac{1}{\sqrt{2}}(|+\rangle + i|-\rangle)$ and $|\downarrow\rangle = \frac{1}{\sqrt{2}}(|+\rangle - i|-\rangle)$. In the last line of Eq. 3.3, the denominator becomes the unpolarized cross-section, and the numerator shows the interference effect. From the numerator, the A_N is non-zero only if there is an interference between spin flip and non-flip amplitudes having a non-zero phase shift. As a result, if some process has undetectable cross-section but large phase shift, it may be detected in the A_N measurement. Therefore, A_N provides another

important test independent from the unpolarized cross-section measurement.

3.2.2 A_N measurements of pion in $p+p$

The summary of pion A_N is introduced in this section because large pion A_N was the motivation of IP12 experiment, where forward neutron A_N was first measured.

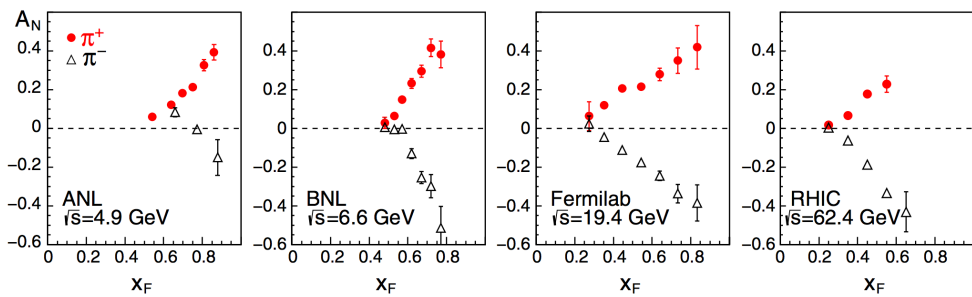


Figure 3.4: A_N of inclusive pion produced from polarized $p+p$ collisions in at various center of mass energies [4]

A_N of forward meson production in $p+p$ have been measured for various energies from $\sqrt{s} = 4.9$ to 500 GeV [37–50]. Figure 3.4 shows the A_N of pion measured at various energies. The A_N seems to be scaled by x_F , and its magnitude becomes increased as x_F increases. As beam energy grows, the kinematic range covers pQCD region. That is the case of E704 experiment at Fermilab [42–44] shown at Fig. 3.4, and also at even higher energies at RHIC [4, 46, 48, 49] as shown in Fig. 3.5.

On the contrary to the observation, the $2 \rightarrow 2$ free parton scattering QCD calculation with collinear picture expects too small asymmetry $A_N \sim \alpha_s m_q / \sqrt{s} < O(10^{-2})$ compare to the data, where m_q is mass of a quark. In order to understand the results, theories include the parton transverse momentum, and gluon field interaction with parton. Currently, three major mechanisms, Sivers [51], Collins [52], and Twist-3 effects [53, 54], are discussed as the possible origin of generating the A_N , but yet large A_N is not explained.

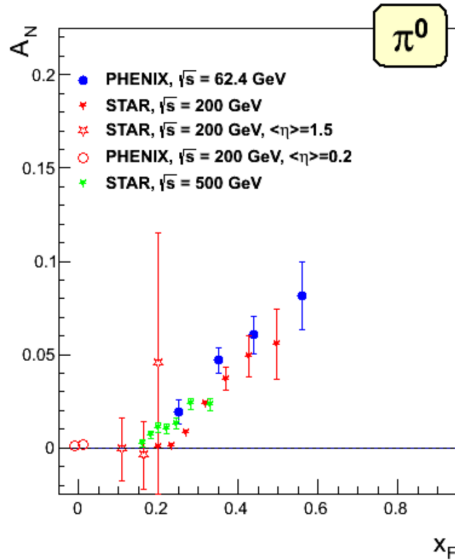


Figure 3.5: A_N of inclusive pion produced from polarized $p+p$ collisions in at various center of mass energies [4] .

Meanwhile, the correlation between the A_N and the photon multiplicity for forward electromagnetic (EM) jet at pseudorapidity $2.5 < \eta < 4.0$ in $p+p$ at $\sqrt{s} = 500$ GeV is measured at STAR [5]. The result is shown in Fig. 3.6. As one can see from the figure, the A_N is large for photon multiplicity of 1 and 2, which mainly comes from isolated π^0 events. The result indicates that the origin of the A_N for π^0 production in $p+p$ may significantly from diffractive processes, whose characteristic is large rapidity gaps.

3.2.3 IP12 experiment

First A_N measurement of forward neutron was done in IP12 experiment [6] at RHIC with the early polarized $p+p$ run. The motivation of this experiment was to development a local polarimeter at RHIC by finding a probe which gives sizable A_N to monitor transverse polarization of proton beam (see principles at Sec. 4.1.9). Three neutral particles, π^0 , γ , and neutron, were measured at the very forward rapidity.

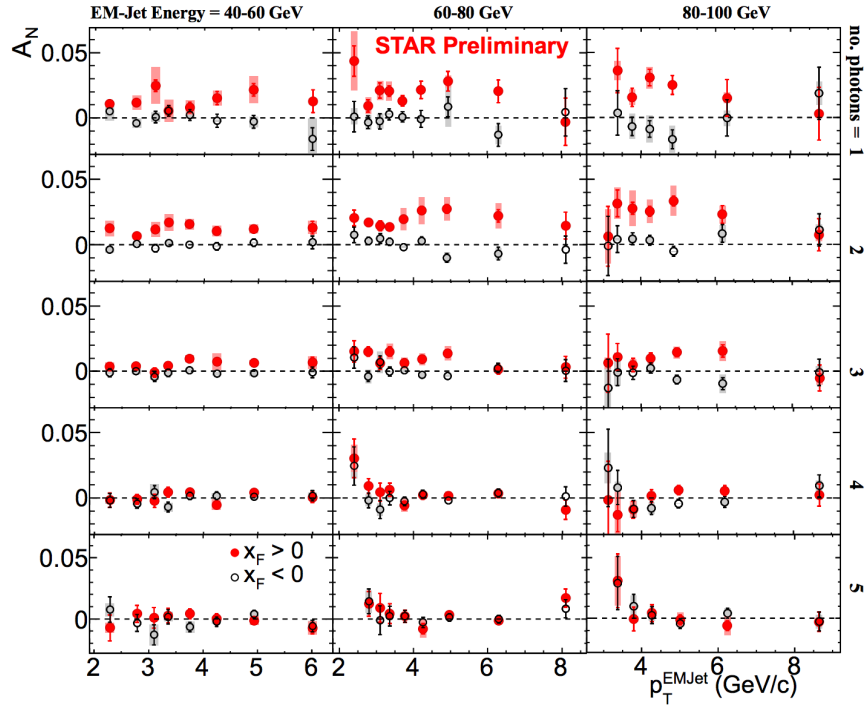


Figure 3.6: A_N vs. p_T for EM-jets [5]. The row corresponds to the number of photon, and the A_N is measured as a function of jet p_T .

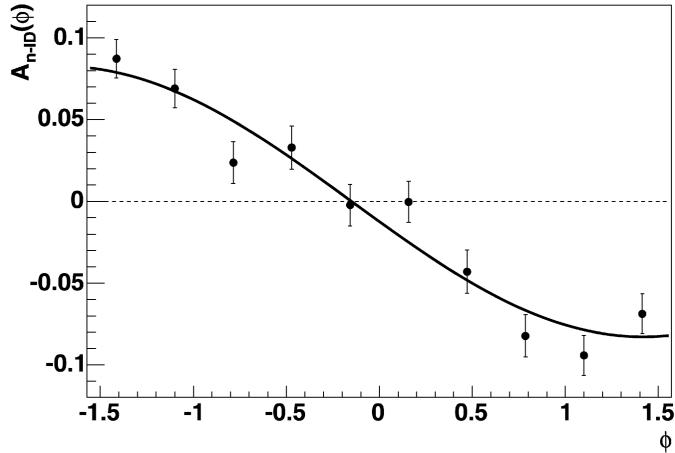


Figure 3.7: Forward neutron A_N as a function of ϕ measured at IP12 [6].

Originally, this experiment was designed to detect photon inspired by large forward π^0 asymmetries introduced in the previous section. The detector was composed of EMCAL, preshower counter for veto charged particles, and postshower counters to veto hadrons. Against expectations, the observed A_N of π^0 was smaller than the uncertainty (however, sizable A_N was measured in the recent RHICf experiment [55]), whereas large A_N was observed for the neutron, as shown in Fig. 3.7, which were originally treated as background events. This result was not expected because the A_N of forward neutron production from the OPE model is nearly zero [7].

3.2.4 PHENIX experiment

Motivated by the IP12 experiment, more precise measurement was done at PHENIX [3] with hadron calorimeter having better energy resolution (25 – 20% for 100-50 GeV neutron). The large negative A_N was reproduced. With better energy resolution, the x_F dependence of A_N was analyzed as well. The result is shown in Fig. 3.8. Sizable A_N was observed in the forward rapidity, whereas zero A_N was observed in the backward.

3.2.5 Regge theory: π and a_1 interference

As explained in Sec. 3.2.1, non-zero A_N requires interference between the spin flip amplitude and the spin non-flip amplitude having non-zero phase shift. From Eq. 2.15, the phase factor of the scattering amplitude depends on the signature factor. Then the Eq. 3.3 can be rewritten in the Regge theory description as

$$A_N \sim \text{Im} [\eta_{\text{non-flip}}(t)\eta_{\text{flip}}^*(t)]. \quad (3.4)$$

Since $\eta(t) = [e^{-i\pi\alpha(t)} \pm 1]/[\sin \pi\alpha(t)s^{\alpha(t)}]$ is a function of Regge trajectory, for the same kind of particle exchange, the $\eta(t)$ will be same for both spin flip and non-flip, therefore A_N becomes zero. This is the case for OPE models.

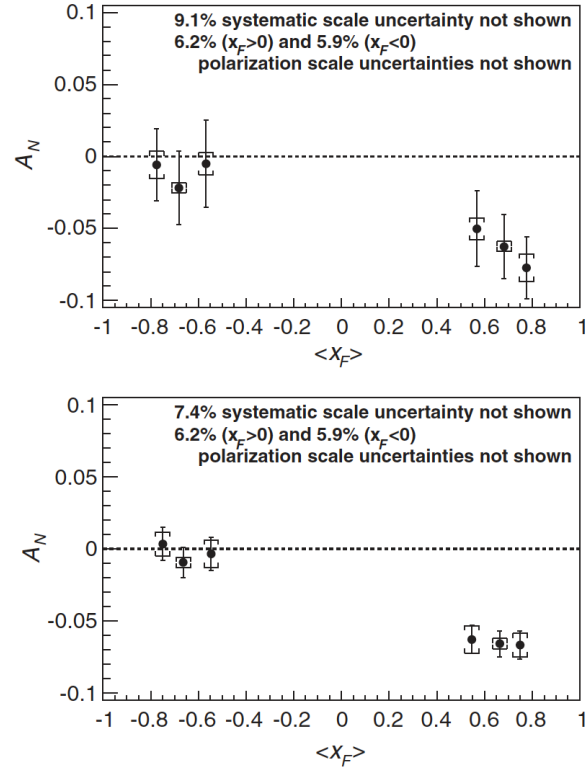


Figure 3.8: Forward neutron A_N as a function of x_F measured at PHENIX [3]. Top: neutron inclusive, bottom: requiring inelastic event tagging trigger (BBC, see Sec. 4.2.1).

The absorptive correction [36], for interaction between the initial protons or final state neutron with other particle(s), modifies the scattering amplitude, however, it generates an order of smaller A_N [7].

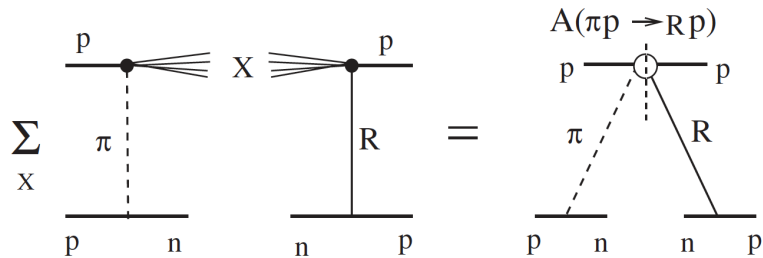


Figure 3.9: Diagram for the interference between π and a_1 exchanges [7].

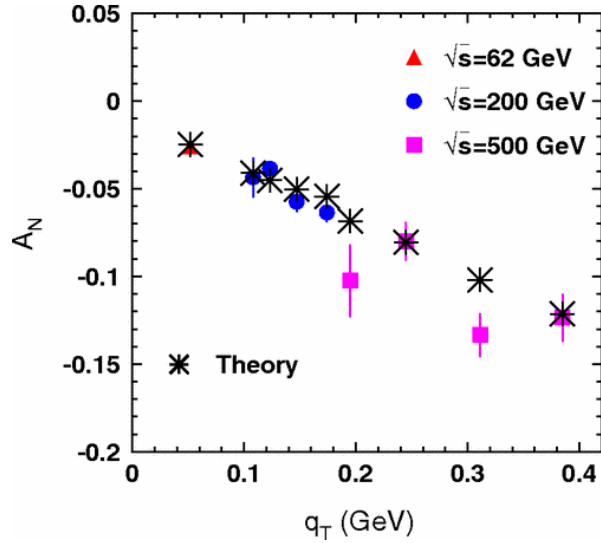


Figure 3.10: Forward neutron A_N as a function of p_T . The PHENIX data is drawn with the theory [7]. The A_N comes from the interference between π and a_1 exchanges generate dominantly.

In order to explain the A_N , the OPE introduced exchanging $a_1(1260)$, which has unnatural parity and interfere with pion as depicted in Fig. 3.9. As can be seen in Fig 3.9, the calculation requires $p + \pi \rightarrow p + R$ production, and in RHIC energies, its total cross section comes from Pomeron exchange dominantly, therefore, other natural parity Reggeon exchanges are suppressed. In order to conserve both total angular momentum and parity in πpn or a_1pn vertex, π exchange flips spin and a_1 does not. Since a_1 spin is odd, and π spin is even, their $\eta(t)$ has different function form, $e^{-i\pi\alpha(t)} + 1(-1)$ for even (odd) spin. Then the Eq. 3.4 can be rewritten as

$$A_N \sim \text{Im} [(i - \cot[\frac{\pi\alpha_\pi(t)}{2}])^* (-i - \tan[\frac{\pi\alpha_{a_1}(t)}{2}])]. \quad (3.5)$$

The Regge trajectory of pion is $\alpha_\pi = \alpha'(t - m_\pi^2)$, where $\alpha' \simeq 0.9 \text{ GeV}^{-2}$. a_1 is effectively replaced by two particles, π and ρ , exchange due to smallness of a_1 production. Then effective a_1 trajectory becomes $\alpha_{a_1}(t) = -0.5 + 0.45\text{GeV}^{-2} t$. As a result, the interference between the spin flip π and spin

non-flip a_1 exchange amplitudes generates large A_N , and well explain the PHENIX data as shown in Fig. 3.10.

3.2.6 Nuclear dependence

Based on the models in the previous sections, the naive prediction for nuclear dependence of A_N was made. The A_N comes from interference between π and a_1 , as explained in Sec. 3.2.5. Then in $p+A$ collisions, the nucleus will provide more π and a_1 , and their interference will generate still negative A_N .

The calculation [56] was done after the A_N measurement in $p+A$. Without nuclear effect, the A_N becomes moderately smaller as A grows, due to absorption of the final state neutron in the nucleus. If the neutron is produced inside the nucleus, the interaction between them smears the A_N .

The nuclear dependence on A_N in the perturbative region has been studied theoretically. While enhanced gluon saturation effects (at low x , gluon density does not infinitely grows, but the density starts to saturate by recombination) in nucleus predicted decreased hadronic A_N as A increases [57–61], some theory based on the pQCD factorization expected approximately no nuclear dependence on A_N [62]. However, almost no theory prediction existed for diffractive production before this measurement.

Although neutrons are mostly produced from diffractive mechanisms, due to forward kinematics, there should be contribution of low- x parton scattering. In fact, in the PYTHIA simulation study [3], 30% of forward neutrons come from gluon scatterings. Therefore, we may not ignore gluon saturation effect as nuclei becomes heavier. Not only the nuclear effects, as the nucleus charge grows, increased electromagnetic processes should be also considered. Due to small momentum transfers in forward kinematics, there can be contribution from electromagnetic production. However, before this measurement, those effects on the forward neutron A_N was almost not studied.

Chapter 4

Experiment

4.1 RHIC

4.1.1 Overview

The Relativistic Heavy Ion Collider (RHIC) [9] at Brookhaven National Laboratory is the only collider which can provide polarized beam. RHIC is designed to study properties of quark-gluon plasma and cold nuclear matter through high-energy light and heavy nuclei collisions, disentangle the proton spin contribution of gluons and sea quarks through longitudinally polarized proton beam, and transverse spin effects through transversely polarized proton beam. From 2000, RHIC has provided polarized protons up to 255 GeV and various nuclei, from light to heavy species up to 100 GeV. Col-

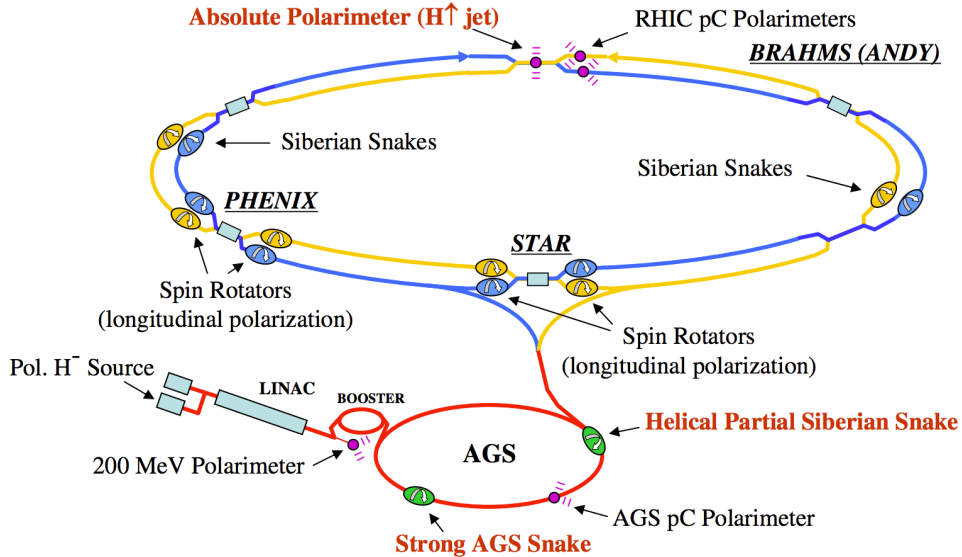


Figure 4.1: RHIC complex with the beam polarization apparatus.

colliding two beams of different species with different rigidity is also possible at RHIC. In 2015, RHIC accomplished the world's first high-energy polarized proton-nuclei collisions. RHIC collided transversely polarized protons with unpolarized aluminum, and gold nuclei.

Figure 4.1 shows a bird's eyes view of RHIC accelerator complex. There are total 6 interaction points at RHIC. Two of them are used for the PHENIX experiment at 8 o'clock and the STAR experiment at 6 o'clock. At the 12 o'clock interaction point, there are two polarimeters (see Sec. 4.1.9).

4.1.2 Polarized proton source

The polarized proton source at RHIC is called Optically-Pumped Polarized Ion Source (OPPIS) [8] [63]. Figure 4.2 shows the layout of the OPPIS. To make polarized protons, first the hydrogen molecule H₂ gas becomes plasma H⁺ by Electron Cyclotron Resonance (ECR) technique. In the ECR source H⁺ has high beam divergence. In order to increase the brightness of

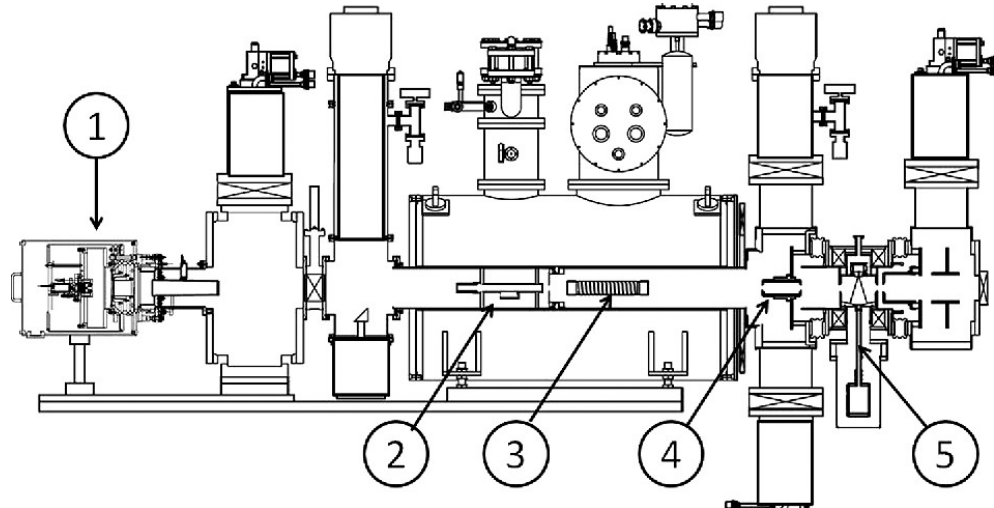


Figure 4.2: A layout of the Optically-Pumped Polarized H^- Ion Source (OP-PIS): 1 - atomic hydrogen injector; 2- pulsed He-gaseous ionizer cell; 3-optically pumped Rb-vapor cell; 4-Sona-transition; 5-Na-jet ionizer cell [8].

the beam, the ECR source H^+ passes a spherically shaped multi-aperture molybdenum grid for the “geometrical” focusing and passes a hydrogen neutralizer cell then becomes a beam of neutral hydrogen atom H^0 . The H^0 loses the electron in the He-ionizer cell then becomes H^+ .

The H^+ beam becomes the electron spin polarized H^0 beam by picking up polarized electrons in the optically pumped vaporized Rb cell. The Rb cell resides in an axial 2.5T field in order to keep polarization, and the valence electrons of the Rb vapor are excited from $5S_{1/2}$ to $5P_{1/2}$ state by a 795 nm wavelength laser. Then the electron polarized H^0 beam becomes nuclear polarized \vec{H}^0 beam through the Sona transition. The nuclear polarized \vec{H}^0 beam pick up electron by passing Na-jet, then this nuclear-polarized hydrogen ion \vec{H}^- beam is transferred to accelerator chain.

4.1.3 Ion source

Ion beam is generated by the electron beam ion sources (EBIS) [64] since 2012. The EBIS generates ions of 17 keV per nucleon. Before 2012, heavy ion beam had been generated by the Tandem Van de Graaff accelerator.

4.1.4 Accelerator chain

The nuclear polarized \tilde{H}^- beam is transferred to RFQ (radio-frequency quadrupole) followed by 200 MHz LINAC, and accelerated to 200 MeV. The electrons are stripped off during acceleration and then injected into the Booster Synchrotron. Then the proton is accelerated to 1.5 GeV in the Booster, injected to the Alternating Gradient Synchrotron (AGS), accelerated to 25 GeV, and then transferred to the RHIC storage ring. On the other hand, the ions are transferred to 100 MHz RFQ, followed by 100 MHz Linac with their output energies being 300 KeV, and 2 MeV per nucleon, respectively. Then the ion sources are transferred to the Booster, and 4 pulses are merged into a single bunch of 105 MeV per nucleon, then transferred to the AGS. The AGS accelerate the ions to 8.9 GeV per nucleon, then send them to the RHIC storage ring.

4.1.5 RHIC storage rings

The RHIC double storage rings are 3.8 km in circumference, and one of the rings is named as the Yellow ring and another is the Blue ring. The beam running counter-clockwise is called the *Yellow beam* and clockwise is the *Blue beam*. The beam controlling magnets can be manipulated separately from each ring. Positively charged nuclei beams collide the zero crossing angle and at the almost equal momenta $\sqrt{s}/2$ (or per nucleon $\sqrt{s_{NN}}/2$) with the possible small variation if two beams have different rigidities.

Total 120 bunches can be stored at maximum with the 106 ns interval time between bunches. In Run-15, total 109 bunches were filled because 9 consecutive bunches were empty to gain time to raise abort kicker magnet current at the beam dump, and two additional bunches were empty to cross-check the bunch patterns. Those empty bunches are called *abort gap*.

The beam luminosity of Run-15 was $10^{29} \sim 10^{32} \text{cm}^{-2}\text{s}^{-1}$. The integrated luminosity at the PHENIX interaction point is 196.7 pb^{-1} , 2.33 pb^{-1} , and 0.63 pb^{-1} ; and the average polarization is 55%, 54%, and 60% for the Run-15 $p+p$, $p+\text{Al}$, and $p+\text{Au}$ collisions, respectively. Typically once beams are stored, they run about 8 hours. The beam dump can be earlier than that if the beam condition is bad (such as low intensity or low polarization) or by accident. The one cycle of the beam storage is called as a *fill*. Each fill is identified by its *fillnumber*.

4.1.6 Spin pattern

For each spin running, several spin patterns of the proton beam bunches are predetermined at the beginning. The spin patterns are designed to cover all possible combination of up and downs ($+, +, -, -$) of Yellow and Blue beams and almost equally distributed in order to minimize any spin relevant systematic effect. Every fill has one of the preassigned spin patterns.

For the Run-15, eight spin patterns were assigned for the proton beam. They are listed in the Tab. 4.1.

| Pattern name | Beam | Bunch spin pattern |
|--------------|------|--------------------------|
| P1 | B | +--+---+---+---+---+ ... |
| | Y | ++---+---+---+---+--- |
| P2 | B | -+---+---+---+---+--- |
| | Y | ++---+---+---+---+--- |
| P3 | B | +--+---+---+---+---+--- |
| | Y | -+---+---+---+---+--- |
| P4 | B | -+---+---+---+---+--- |
| | Y | -+---+---+---+---+--- |
| P5 | B | ++---+---+---+---+--- |
| | Y | +---+---+---+---+--- |
| P6 | B | -+---+---+---+---+--- |
| | Y | +---+---+---+---+--- |
| P7 | B | ++---+---+---+---+--- |
| | Y | -+---+---+---+---+--- |
| P8 | B | -+---+---+---+---+--- |
| | Y | -+---+---+---+---+--- |

Table 4.1: The Run-15 spin patterns. B and Y represent the Blue and Yellow beams, respectively. + (-) means the beam polarization direction is up (down) at the polarimeters in the 12'o clock interaction point. Those up and downs of 24 bunches repeat through the whole bunches in a fill.

The direction is opposite at PHENIX because the Siberian snake (Sec. 4.1.7) between the 12'o clock and the PHENIX experimental hall reverses the spin direction.

4.1.7 Depolarization and the Siberian snake

In presence of a magnetic field, the polarization of protons follows the

Thomas-BMT equation [65, 66],

$$\frac{d\vec{P}}{dt} = -\frac{e}{\gamma m} [G\gamma \vec{B}_\perp + (1+G)\vec{B}_\parallel] \times \vec{P}, \quad (4.1)$$

where \vec{P} is the polarization vector in the proton's rest frame, $G = 1.7928$ is the proton anomalous magnetic moment, and $\vec{B}_{\perp(\parallel)}$ is the magnetic field perpendicular (parallel) to the momentum of the proton. In case of RHIC, the term with the parallel magnetic field is negligible. Considering the circular motion of the proton in the RHIC ring

$$\frac{d\vec{v}}{dt} = -\frac{e}{\gamma m} [\vec{B}_\perp] \times \vec{v}, \quad (4.2)$$

assuming the magnetic field is purely vertical, the proton spin precesses $G\gamma$ times per one revolution. This number $G\gamma$ is called the spin tune, ν_{sp} .

If all of the magnetic fields are vertical relative to the accelerator plane, the vertical polarization will be stable. However, there are always non-vertical magnetic fields, which cause depolarization, because of following reasons: the imperfection of operation, such as magnet errors or misalignment, and the intrinsic one, focusing magnets. Such conditions can cause depolarizing resonances.

Imperfection depolarizing resonances take place when $\nu_{sp} = G\gamma = n$ is an integer, i.e. whenever the proton beam crosses the imperfect magnetic field in each revolution, the phase of the spin precession is kept same. The energy interval of this condition corresponds to 523 MeV. The intrinsic depolarizing resonances arise when $\nu_{sp} = G\gamma = kP \pm v_y$, where k is an integer, P is the superperiodicity, and v_y is the betatron tune, i.e. when the proton beam passes the horizontal component of the quadrupole magnetic field having the same precession phase. $P = 12$ and $v_y \approx 8.8$ at RHIC. If the spin tune ν_{sp} gets closer to the resonance condition, the faster the proton beam loses

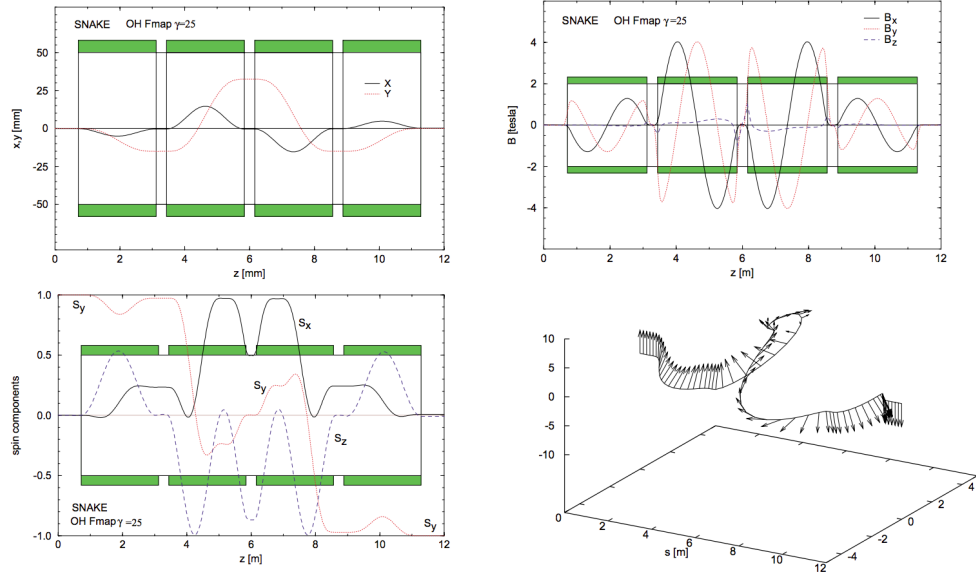


Figure 4.3: The Siberian snake operation at $\gamma=25$: the top left plot shows the beam orbit; the top right plot shows the Magnetic field component; the bottom left plot shows the spin component (see $S_{x,z}$ remains unchanged and S_y flips); and the bottom right plot shows the evolution of the vertical polarization inside the Siberian snake. In each plot, the z -axis is along the beam orbit, x and y is the horizontal and vertical [9].

polarization.

In order to avoid such depolarizing resonances, Siberian snakes are introduced. The two Siberian snakes in the each RHIC ring keep the spin tune to be a half-integer by rotating spin by 180 degree about a horizontal axis every half revolution. In the AGS, two partial Siberian snakes rotate spin a few degrees in order to keep the spin tune away from integer values. Figure 4.3 shows the magnetic field, beam orbit, and the evolution of the spin inside the Siberian snake.

4.1.8 Spin rotator

Since the most stable polarization is the vertical direction relative to the accelerator plane, in order to run the longitudinally or horizontally polarized proton program, Spin rotators adjacent to the experimental halls rotate the polarization direction to the desired direction in the upstream of the interaction point, and then put it back to the vertical direction in downstream. The operation of the spin rotator is similar to that of the Siberian snake (Sec. 4.1.7).

4.1.9 Polarimeters

The RHIC 12'o clock (see location at Fig. 4.1) polarimeters are composed of two complementary ones, the pC polarimeter (carbon target) and the H-jet polarimeter (polarized atomic hydrogen jet target), which measure the polarization in the storage rings. Also, there are the local polarimeters at PHENIX and STAR, which measure the polarization at the collision point of each experiment.

In principle, the beam polarization can be determined by colliding the polarized beam with a target and measuring the left-right asymmetry in the scattering with a known analyzing power A_N :

$$P_{beam} = \frac{\epsilon_N}{A_N} = \frac{1}{A_N} \frac{N_L - N_R}{N_L + N_R}, \quad (4.3)$$

where P_{beam} is the beam polarization, A_N is the analyzing power (left-right asymmetry with the 100% beam polarization), ϵ_N is called as the raw asymmetry, and $N_{L(R)}$ is the number of particles scattered to the left (right). Therefore, the uncertainty of the polarization measurement is affected by how precisely we know the A_N of the specific process experimentally, and how precisely the raw asymmetry $(N_L - N_R)/(N_L + N_R)$ can be measured during the operation. The former is the main uncertainty of the pC polarime-

ter, and the latter is that of the H-jet polarimeter. Therefore, the polarization is measured by those two polarimeters to compensate each uncertainty.

H-jet polarimeter

Figure 4.4 shows the layout of the H-jet polarimeter [10]. The H-Jet polarimeter measures the beam polarization based on the left-right asymmetry of $p+p \rightarrow p+p$ elastic scattering in the Coulomb-Nuclear Interference (CNI) region. Even though the A_N is not precisely known in this process, the H-jet polarimeter still can measure the absolute polarization by using the following techniques.

The H-jet polarimeter is composed of polarized Atomic Beam Source (ABS), scattering chamber, and Breit-Rabi polarimeter. The ABS provides vertically polarized beam by passing the beam to inhomogeneous magnetic field and RF transition. The polarization direction flips every 10 minutes. The absolute polarization of the ABS is measured by the Breit-Rabi polarimeter. The typical polarization of the APS is about 92%.

The beam protons scatter off the ABS protons, and the scattered protons at the ~ 90 degrees are measured in the horizontal plane (See Fig. 4.4). The polarization of both blue and yellow beams can be measured separately by having timing shift between the two beams. Since both beam and the ABS protons have the same analyzing power

$$A_N^{pp} = \frac{\epsilon_N^{beam}}{P_{beam}} = \frac{\epsilon_N^{target}}{P_{target}}, \quad (4.4)$$

the beam polarization can be measured as

$$P_{beam} = \frac{\epsilon_N^{beam}}{\epsilon_N^{target}} P_{target}. \quad (4.5)$$

The beam and target raw asymmetries (ϵ_N) can be measured separately by classifying samples by beam or target spin. This way enables the measurement of the absolute polarization value.

However, the uncertainty of the raw asymmetry ϵ_N of each fill is large ($\sim 5\%$) because the low target density ends up with the large statistical uncertainty even though the measurement is done during the whole storage time. Therefore, the fill-by-fill polarization is measured by the fast pC polarimeter, and the H-jet polarization averaged over multiple fills are used to normalize the pC polarimeter results.

pC polarimeter

The proton-Carbon (pC) polarimeter [9] applies the left-right asymmetry of $p+C \rightarrow p+C$ elastic scattering in the Coulomb-Nuclear Interference (CNI) region to the polarization measurement. Figure 4.5 shows the analyzing power A_N of proton-Carbon scattering in the Coulomb-Nuclear Interference (CNI) region measured at the AGS with the 21.7 GeV/c polarized proton beam [11]. Figure 4.6 shows the layout of the pC polarimeter.

The polarization is measured as

$$P_{beam} = -\frac{\epsilon_N^{target}}{A_N^{pC}} \quad (4.6)$$

The pC polarimeter scans a solid string carbon target to get a polarization profile, and it accumulates enough statistics (2~3 % of statistical uncertainty) in a few minutes. Therefore, the measurement can be done multiple times within a store, which runs for 8 hours typically. The polarization is measured three times per each fill: in the beginning, in the middle, and at the end of a store. This measurement gives fill-by-fill polarization P as well as its decay as a function of time dP/dt . However, the analyzing power A_N is not rigorously

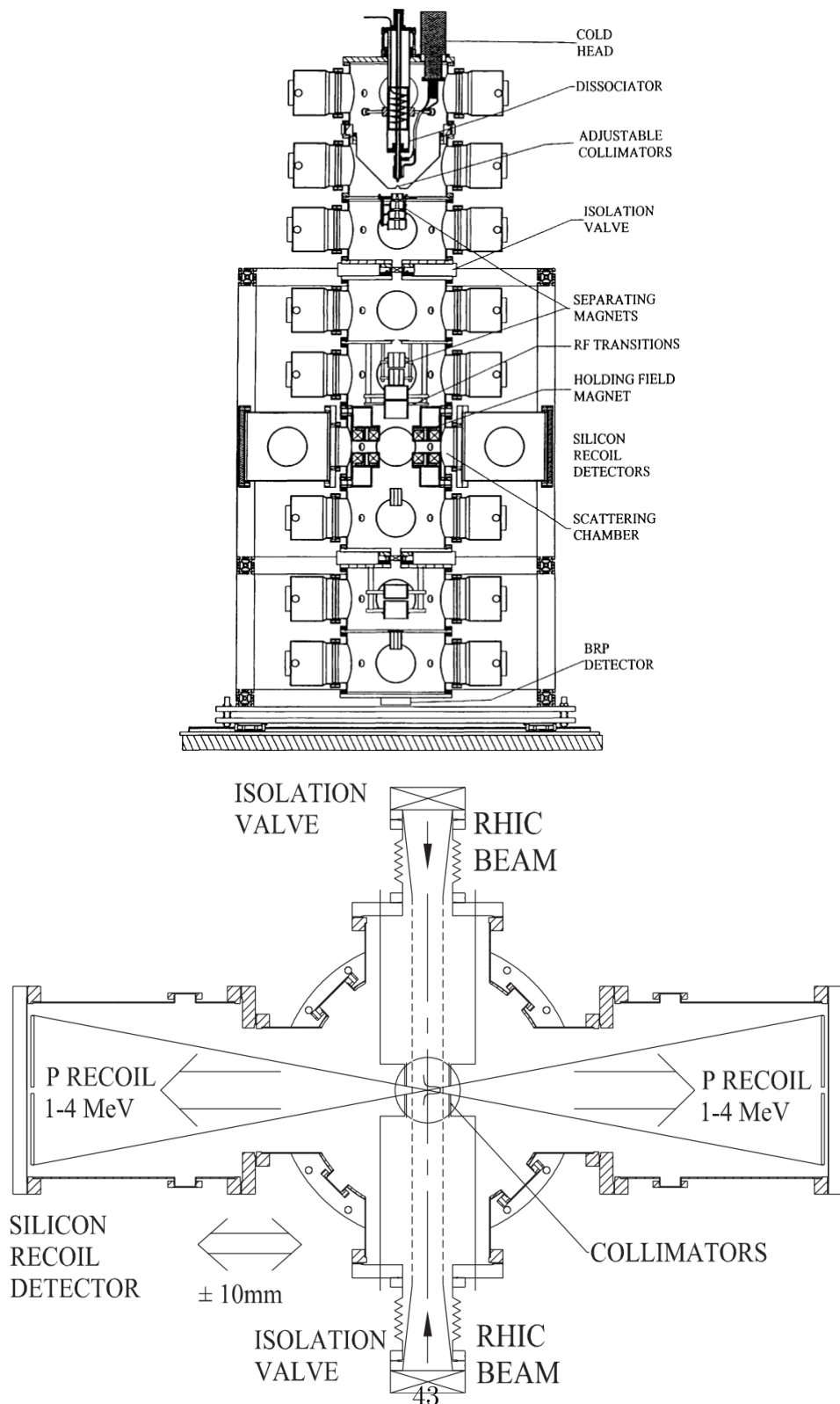


Figure 4.4: The side (left) and the top (right) view of the H-jet polarimeter [10].

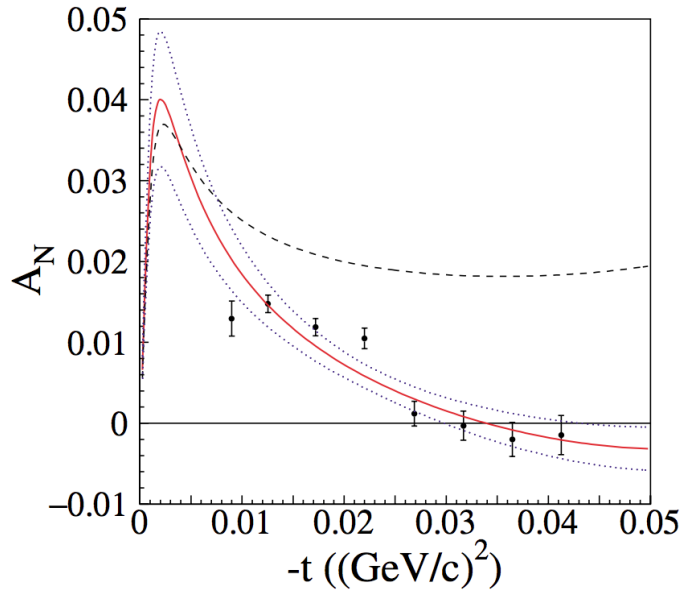


Figure 4.5: The analyzing power A_N of proton-Carbon scattering in the Coulomb-Nuclear Interference (CNI) region measured at the AGS with the 21.7 GeV/c polarized proton beam [11]. The data is drawn with theory curves [12]. The solid and dotted lines are the theory curve with hadronic spin-flip and its uncertainty, respectively. The dashed line is theory curve without hadronic spin-flip amplitude. The polarization of the data is measured by the H-jet polarimeter.

calculated or measured, this measurement cannot give absolute polarization. To get the absolute polarization, the pC polarization is normalized by the H-jet polarization.

Local polarimeter

The nucleon spin physics is one of the major program at RHIC. We study parton helicity structure through longitudinally polarized proton beam and transverse spin effects through transversely polarized proton beam. In such study, we measure spin asymmetries, describing asymmetries of production

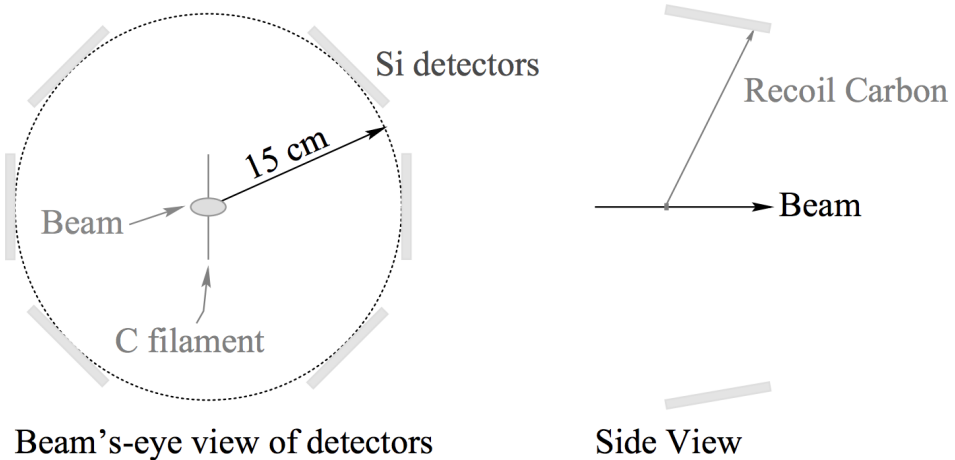


Figure 4.6: The proton-Carbon (pC) polarimeter layout (right) [9].

cross section depending on beam polarization direction. Such measurements inevitably require information of beam polarization, its magnitude and direction. Therefore, as described in the previous sections, RHIC has two polarimeters at 12'o clock for measuring beam polarization.

However, there are reasons to have another kind of polarimeter to monitor beam polarization at each experimental area (one at 8'o clock, the other at 6'o clock), which we call as local polarimeter. The main reasons are:

- The local polarimeter measures the transverse component of beam polarization at experimental hall, which is crucial in helicity asymmetry measurement, however, cannot be provided by the 12'o clock polarimeters.
- The local polarimeter provides direct polarization measurement for the dedicated experiment, so it is much safer than relying on the 12'o clock polarimeters only. For example, it will detect any possible incorrect operation of spin rotators, which changes the polarization at the experimental hall, therefore, but may not be detected at 12'o clock polarimeters. If this case is not detected, it will give the wrong physics result.

- The local polarimeter provides the real-time monitoring of beam polarization with good precision without disturbing experiment.

The operation principle is as follows. When we measure the raw transverse spin asymmetry, or left-right spin asymmetry, of particle production relative to the beam polarization direction,

$$\epsilon_N = \frac{N_L - N_R}{N_L + N_R}, \quad (4.7)$$

this value is proportional to the real physics asymmetry A_N multiplied by the beam polarization in the transverse direction P_\perp

$$\epsilon_N = P_\perp A_N. \quad (4.8)$$

Therefore, particles with known A_N , we can monitor P_\perp at the collision point by monitoring ϵ_N . The PHENIX local polarimeter measures ϵ_N of forward neutron because of its large A_N and statistics.

In case of transversely polarized proton beam, the beam polarization is equal to its transverse polarization component $P_\perp = P$. This value is provided by the 12'o clock polarimeters and supposed to be same at the experimental hall unless misoperation. Then the ϵ_N measured by the local polarimeter provides the azimuthal angle of polarization direction at the experimental hall, and it cross-checks polarization decay with the 12'o clock polarimeters.

In case of longitudinally polarized proton beam, the local polarimeter plays a crucial role in measurement. One of the major program at RHIC is the measurement of helicity distribution of gluon and sea quarks inside the proton. This is done by measurement of the asymmetry of particle production cross section depending on the helicity state of colliding proton beam(s). Therefore, any transverse polarization component will dilute the asymmetry value.

For the longitudinally polarized run, the beam polarization is kept vertical

in the ring in order to keep the polarization in the strong vertical magnetic fields along the ring, then spin rotators up/downstream of experimental halls rotate polarization direction 90 degrees, therefore, beam polarization direction is longitudinal only at the experimental hall. However, in real experiments, beam polarization direction at the experimental halls is not perfectly longitudinal; tiny transverse component P_{\perp} may remain. The local polarimeter measures this fraction P_{\perp}/P and then real longitudinal component P_{\parallel}/P , then enable to calculate systematic from the polarization on asymmetry.

The measurement principle is that we measure ϵ_N in Eq. 4.7 for runs with both transversely (run1) and longitudinally (run2) polarized beams. Since the physical A_N values are same for both

$$A_N = \frac{\epsilon_N^{run1}}{P_{\perp}^{run1}} = \frac{\epsilon_N^{run2}}{P_{\perp}^{run2}}, \quad (4.9)$$

the polarization can be obtained as

$$\frac{P_{\perp}^{run2}}{P_{\perp}^{run1}} = \frac{\epsilon_N^{run2}}{\epsilon_N^{run1}} \frac{P_{\perp}^{run1}}{P_{\perp}^{run2}} \quad (4.10)$$

where we can obtain P_{\perp}^{run1} and P_{\perp}^{run2} from the 12'o clock polarimeters. Then calculate $\frac{P_{\parallel}}{P}$ as

$$\frac{P_{\parallel}}{P} = \sqrt{1 - \left(\frac{P_{\perp}}{P}\right)^2}. \quad (4.11)$$

4.2 PHENIX

The Pioneering High Energy Nuclear Interaction eXperiment (PHENIX) detector [67–73] is designed to measure diverse probes produced from p-p, p/d/h-A, and A-A collisions in order to study the properties of hot and cold nuclear matter and proton spin structure. The PHENIX detector is optimized to measure rare processes with high energy resolution by fine granularity, high rate capability, and advanced trigger systems. To achieve such conditions, the acceptance is sacrificed. Figure 4.7 and 4.8 shows the layout of the PHENIX detector and magnetic field. The composing detectors are categorized as the global detectors for characterizing the collision, the central arm for various particles, the forward muon arm, and the silicon vertex detectors.

4.2.1 Beam-Beam Counter

The beam-beam counter (BBC) [72] is an array of čerenkov radiators. An element of the BBC consists of a photomultiplier and a 3 cm thick quartz čerenkov radiator, and 64 elements compose one BBC. Two BBCs are located at ± 144 cm from the collision point surrounding the beam pipe. The coverage is $3.0 < \eta < 3.9$ in pseudo-rapidity, and full azimuth. The BBC detects charged particles with velocity $\beta > 0.7$. The timing resolution of one element is 54 psec. A coincidence between two BBCs are used as a minimum bias trigger. This trigger detects about 50% of inelastic collisions at 200 GeV $p+p$ collisions.

4.2.2 Zero-Degree Calorimeter

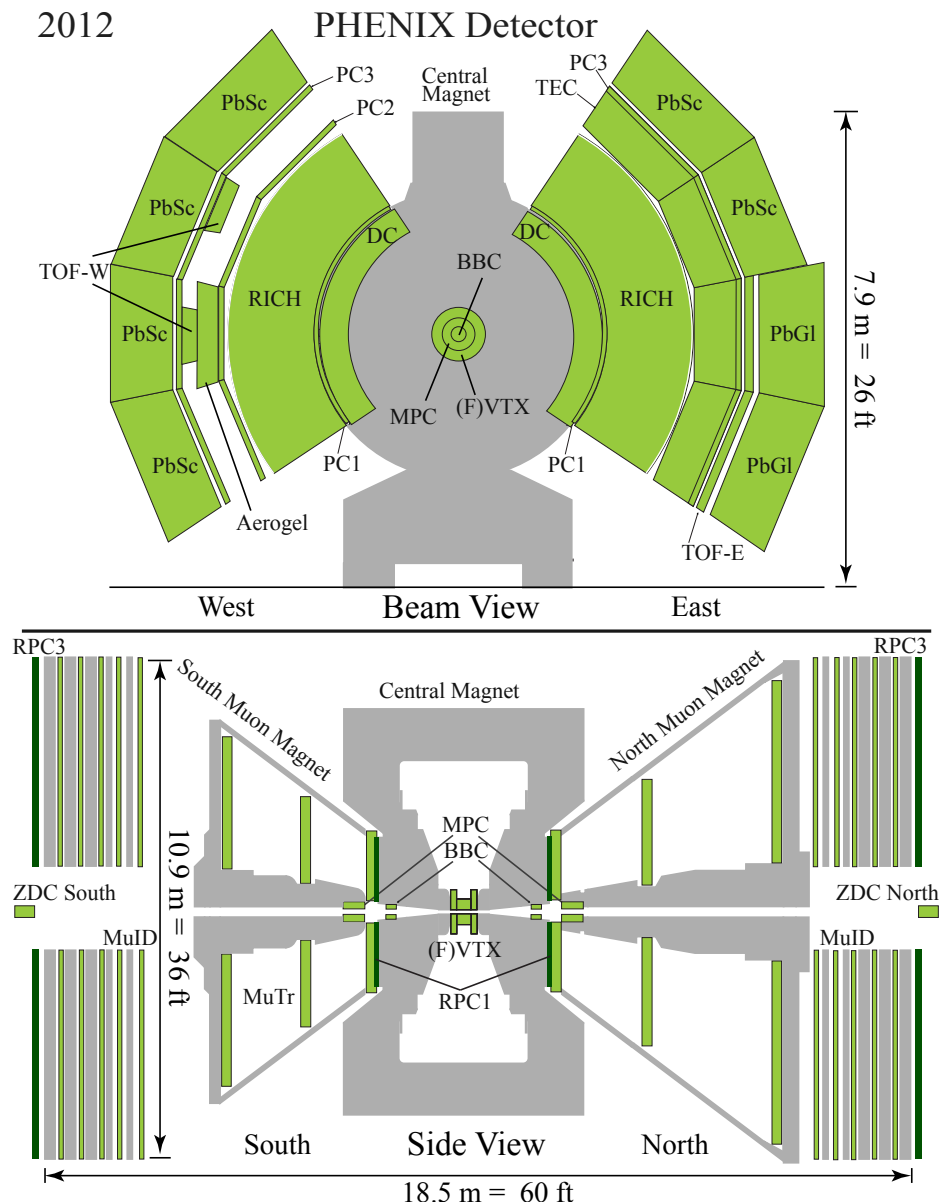
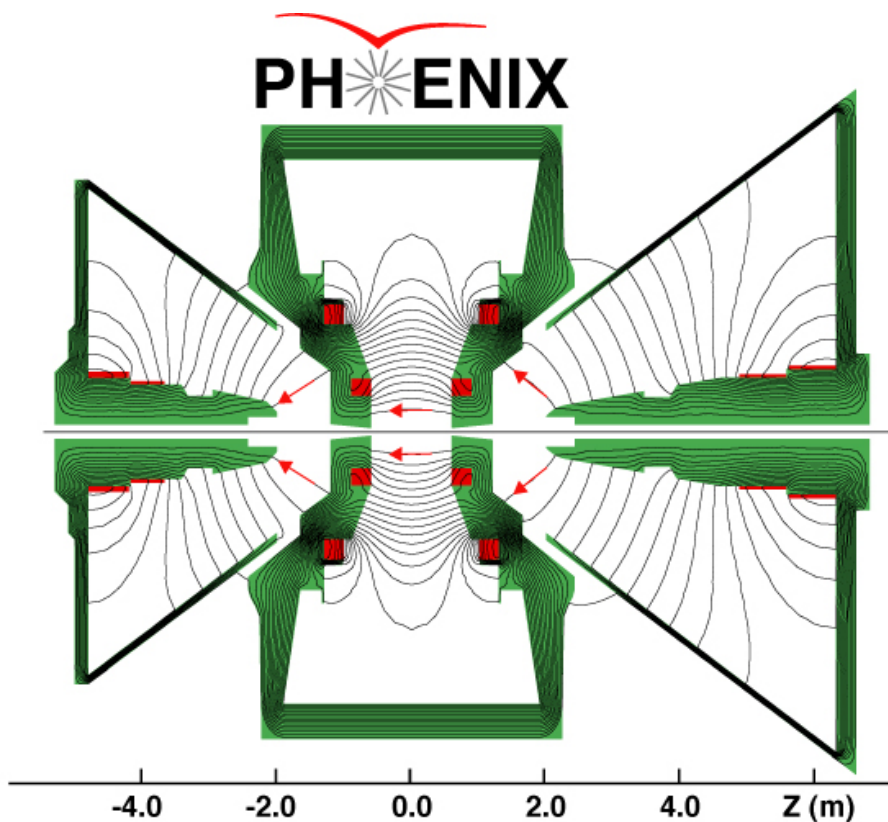


Figure 4.7: PHENIX detectors.



Magnetic field lines for the two Central Magnet coils in combined (++) mode

Figure 4.8: PHENIX magnetic field lines.



Figure 4.9: BBC

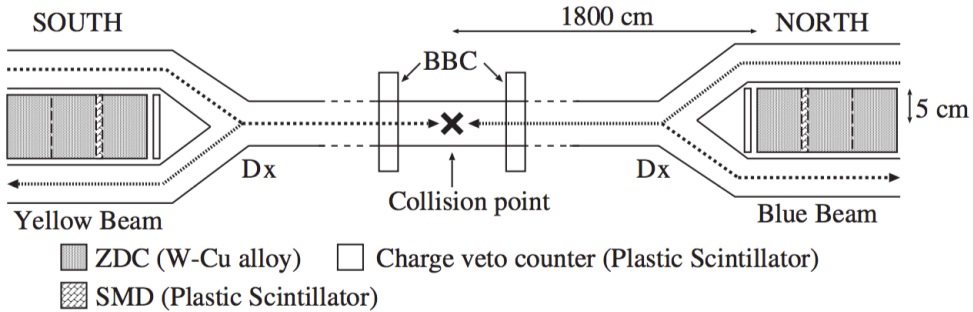


Figure 4.10: A layout of the ZDC and BBC.

The Zero-Degree Calorimeter (ZDC) [74] is a Čerenkov sampling hadron calorimeter. ZDC is designed to detect neutrons around zero-degree in order to identify peripheral collisions by measuring its characteristic spectator neutrons. ZDC is located in a narrow space between the two beam pipes as shown in Fig. 4.10, covering 10 cm x 10 cm in transverse plane. Three ZDC modules are located in series at ± 18 m away from the collision point, each side of the beam direction.

As shown in Fig. 4.11, the ZDC comprises of alternate multiple layers of two kinds of plates. The W-Cu alloy layers generate particle showers, and the layers comprised of the PMMA based optical fibers transmit Čerenkov light produced by the charged shower secondaries. Those plates are tilted by 45 degrees relative to the beam orbit, which is about the Čerenkov angle for $\beta \sim 1$ particles in PMMA. The length of one ZDC module is 23 cm, which corresponds to 1.7 nuclear interaction length and 51 radiation length. The energy resolution of three ZDC modules is $\sim 25\text{--}20\%$ for 50–100 GeV neutrons, and the timing resolution is 150 ps.

The Shower Max Detector (SMD) is a scintillator strip hodoscopes. SMD comprises of 7 strips in vertical direction for x position and 8 strips in horizontal direction for y position measurement. SMD is inserted between the first and second ZDC modules, where hadronic shower is approximately maximum. The position resolution is ~ 1 cm for 50–100 GeV neutrons.

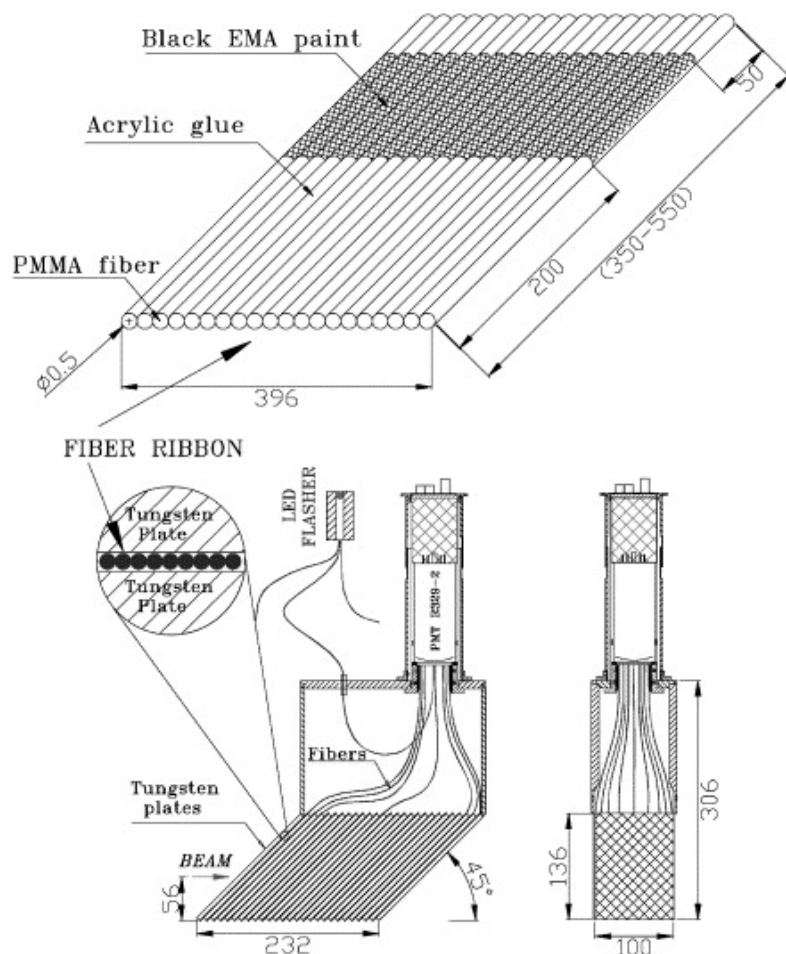


Figure 4.11: Schematic drawing of the ZDC component.

As can be seen in Fig. 4.10, the RHIC beam splitting dipole magnet (DX) is located upstream of these neutron detectors therefore, charged particles are expected to be swept out of the ZDC acceptance. A pair of scintillator paddles with matching acceptance with ZDC was implemented upstream and downstream of ZDC, respectively. It is called charge veto (CV) counters. However, these counters were not used in Run15 analysis due to their operation issues.

4.2.3 Electronics and Trigger

The ZDC has 4 (3 modules + 1 analog signal sum) channels, and the SMD has 16 (15 strips + 1 analog signal sum) channels. Each channel has 1 ADC and 2 TDCs (TDC0, TDC1). The signal in each channel begins to be processed if it passes the discriminator with 15 GeV of threshold. The ADC gate signals of all channels of the ZDC and SMD are generated by the ZDC analog sum signal.

The ZDC trigger is operated based on the TDC bit and set to be fired for ZDC summed energy > 15 GeV. This threshold is implemented at the TDC discriminator. The TDC start signal is given by the Global Timing Module (GTM) of the ZDC, which delivers the beam clock signal with a shift optimized for the beam particle timing at ZDC; and the TDC stop signal is generated by the pulse at each channel individually. If there is no hit in the ZDC for a given collision timing window, the TDC has overflow bit. The ZDC trigger fires whenever there is no overflow bit.

4.3 Run-15 operating conditions

As in the Fig. 4.10, before the Run-15 $p+A$, the alignment of detector and beam orbit were symmetric. However, in order to adapt two beams with

different rigidity in $p+A$ collisions, the DX magnets were moved horizontally from its original position [75]. In the nominal $p+A$ run, both proton and Au (Al) beams were angled off by $\sim 3.6(3.0)$ mrad relative to the beam direction in $p+p$. ZDC was also moved in order to accommodate the zero-degree line into the acceptance. However, the movement of ZDC was only 2 mrad (3.6 cm). It was limited by the narrow space between the two beam pipes around ZDC. As a result, the beam axis was located at the edge of ZDC in the nominal $p+A$ setup.

Therefore, in the special setup for this measurement, the proton beam orbit was adjusted to the center of the ZDC. The proton beam was angled off by ~ 2 mrad relative to the beam direction in $p+p$ with beam opening angle of $\sim 2(1.1)$ mrad between Au (Al) (see Fig. 4.12). The beam orbit is summarized in Tab. 4.2. As a result, the beam center was at the center of ZDC in the special stores. This measurement is done with the special stores.

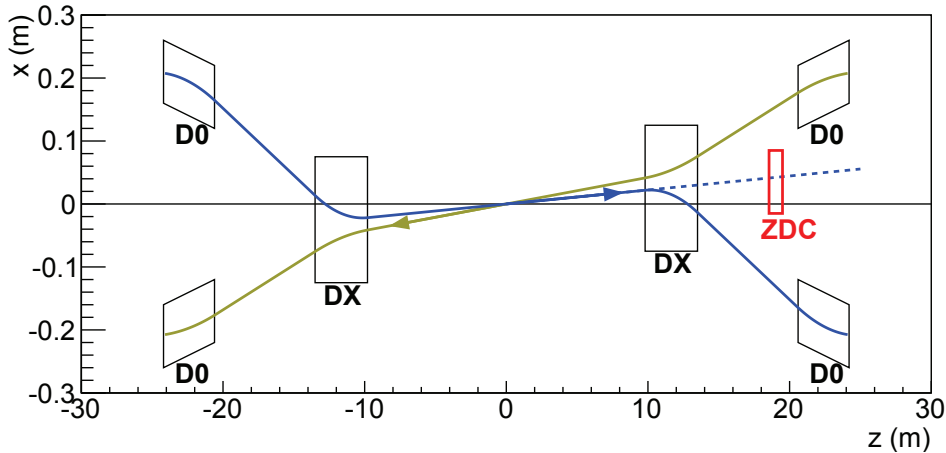


Figure 4.12: ZDC location and beam orbits of proton (blue) beam and heavy-ion (yellow) beam in the special stores used for this analysis; the z -axis shows the nominal beam direction, and the dashed line represents the zero-degree neutron trajectory. DX and D0 are the RHIC beam bending dipole magnets.

The north ZDC was moved longitudinally from $Z=1800$ cm to $Z=1856$

Table 4.2: Beam orbits in mrad. This measurement is done with the special stores.

| Beam | p+p | p+Al nominal | p+Al special | p+Au nominal | p+Au special |
|--------|-----|--------------|--------------|--------------|--------------|
| Blue | 0 | 2.951 | 2.227 | 3.624 | 2.222 |
| Yellow | 0 | 2.951 | 3.317 | 3.624 | 4.222 |

cm, during the maintanence in 2014, then moved transversely by 3.5 cm during the Run-15 $p + p$ to $p+A$ transition period.

Figure 4.13 shows changes of beam orbits between physics stores and local pol dedicated stores in $p+Au$.

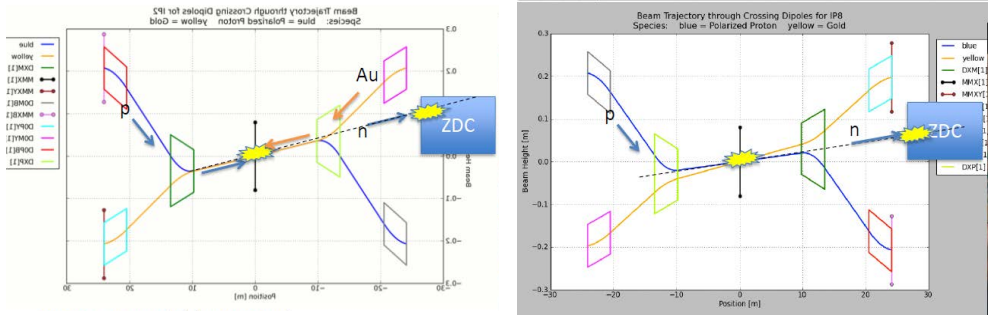


Figure 4.13: Beam orbits in $p+Au$ physics stores (left), and $p+Au$ local pol dedicated stores (right). Angles are not in scale.

Chapter 5

Analysis

5.1 Overview

The analyzed $\sqrt{s_{NN}} = 200$ GeV $p+p$ and $p+A$ collisions data are categorized into four data sets; Run-08 $p+p$, Run-15 $p+p$, Run-15 $p+Al$, and Run-15 $p+Au$. The data taking period of Run-08 and Run-15 nominal $p+p$ collisions were approximately one month and two months, respectively. However, only the last ~ 10 days of the data taking period for both sets matched the analysis condition. Otherwise, the Charge veto counter (CV) was not available in case of Run-08, and the inclusive neutron trigger was not available in case of Run-15. Therefore, those partial period of data were analyzed. One 3 hours of special store was taken for $p+Al$, and another 2 hours of special store was taken for $p+Au$.

The data were collected by the ZDC inclusive trigger. Various BBC tagging samples in addition to the ZDC inclusive trigger, were also analyzed in order to study different neutron production mechanisms. The neutron asym-

metry was analyzed for the north ZDC, which faced the polarized proton beam.

The data were segmented as a “run”, which corresponds to one cycle of DAQ data-taking, typically takes one hour. Each run was identified by its “runnumber”. The data quality was assured for run-by-run initially, and then done for event-by-event.

The detector calibration was done with three steps. First, the ZDC pedestal was calibrated with an LED flasher before collision data taking. Then, the SMD pedestal and gain matching calibrations for position reconstruction were done with collision data. Finally, the absolute energy scale of the ZDC was done using the $d\sigma/dx_F$ peak of forward neutron at $r < 2$ cm (even more forward than the analyzed neutrons $r < 4$ cm) after the neutron identification in the next paragraph was done.

The neutron identification was done for photon. In addition, proton background was rejected in Run-08 $p+p$ only, where CV was available. The background after the identification was mainly proton. The background fraction could be estimated by data based on its characteristic x -distribution, based on the simulation study.

The raw asymmetry ε_N was calculated by square-root formula (Eq. 5.6), then normalized by polarization (A_N^{fit}). The background asymmetry A_N^B was calculated by the Run-08 $p+p$ data, then subtracted to get the signal asymmetry A_N^s of Run-15 $p+p$ data. The estimated background fraction was not significant in case of $p+A$, so background asymmetry was not subtracted.

The detector resolutions affect asymmetry measurement. The reconstructed energy and position of a neutron are smeared by the detector resolutions. Therefore, they affect data sampling and smear asymmetry of a given sample. The final asymmetry A_N should be corrected by smearing factor C_{smear} as $A_N = /C_{\text{smear}}$, where C_{smear} represents all of the detector characteristics.

Since one of the biggest variations in the smearing correction comes from the assumed $A_N(p_T)$ shape, the p_T dependent A_N^S was analyzed as the same

way. Finally, the systematic uncertainties were estimated for uncertainties from charged background asymmetry, smearing, beam position, calibration, and polarization. The final result is published at Phys. Rev. Lett. [76].

5.2 Summary of the previous background study for *p*+*p* and the analysis cut

Background event structure in $\sqrt{s} = 200\text{GeV}$ *p*+*p* collisions was studied in the previous publication [3] of Run-05 data, and the result is summarized in Sec. 5.9.1. Our analysis cuts are based on this study (see Sec. 5.2.2. However, we could not apply the same background treatment to our case because a running condition was changed. One major reason is that the charge veto counter, which significantly suppressed the charged background in the previous analysis, is not available in our analysis. Another main reason is that the background fraction is sensitive to the transverse shift of the beam center position relative to the ZDC, which can be different between runs. Therefore, we developed another way to estimate a background fraction, which are explained in Sec. 5.9.

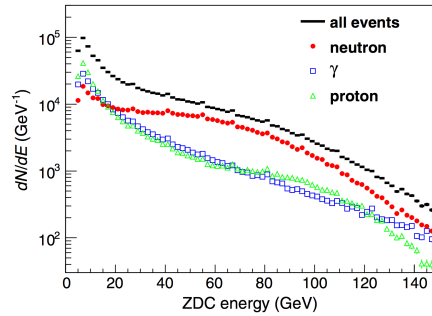
5.2.1 Previous simulation study

The background structure at ZDC in *p*+*p* collisions at $\sqrt{s} = 200\text{ GeV}$ was examined by PYTHIA6 [77] event generator with GEANT3 [78] for the previous publication [3] of Run-05 neutron A_N in *p*+*p* collisions. The apparatus in the simulation included the neutron detectors, the beam pipe, BBC, and the Dx magnet in front of the ZDC. Since there is a beam bending magnet in front of the ZDC, charged particles having nearly beam momenta are ex-

pected to be swept away from the ZDC acceptance, and only neutral particles are expected to be detected naively. However, some scattered protons could hit the ZDC as well.

At the 5 GeV ZDC energy threshold, 92% of events deposit a single particle at the ZDC. Multi-particles events are mainly consist of one neutron and one photon. This kind of events do not affect neutron position measurement because electromagnetic shower of photon stops in the first ZDC module, in front of the SMD, and they only increase the measured energy from the original neutron energy. This multi-particle effect is neglected in this analysis.

| Physics process | Neutron (μb) | γ (μb) | Proton (μb) |
|---------------------------------|---------------------|----------------------|--------------------|
| $qq \rightarrow qq$ | 35 | 46 | 14 |
| $q\bar{q} \rightarrow q\bar{q}$ | <1 | <1 | <1 |
| $q\bar{q} \rightarrow gg$ | <1 | <1 | <1 |
| $gg \rightarrow gg$ | 268 | 358 | 95 |
| $gg \rightarrow q\bar{q}$ | 9 | 12 | 3 |
| $gg \rightarrow gg$ | 352 | 468 | 114 |
| Elastic scattering | 0 | 0 | 446 |
| Single diffractive (XB) | <1 | 2 | 387 |
| Single diffractive (AX) | 462 | 527 | 107 |
| Double diffractive | 328 | 413 | 92 |
| Low- p_T scattering | 551 | 651 | 137 |
| Total | 2006 | 2479 | 1395 |



(a) Production processes [79]. (b) ZDC energy distributions [3].

Figure 5.1: PYTHIA+GEANT: Event structure of main particles (neutrons, photons, and protons) at the ZDC acceptance at 5 GeV threshold.

Single particle events are mainly neutron, proton, and photon. Figure 5.1a summarizes their production processes. Figure 5.1b shows their ZDC energy distributions. Photons are suppressed over 20 GeV. Since one ZDC module corresponds to 51 radiation length, when more than one SMD scintillator above threshold are required for both x and y positions (#SMD: $nx > 1$ and $ny > 1$), the photon events become negligible. In order to reduce the proton background, events deposit more charge than 1/2 MIP peak at the CV was rejected.

The main background after neutron identification, are protons and K^0 s at the energy over 20 GeV. The K^0 contamination is estimated by both ISR

experiment [27] and PYTHIA simulation and they give a consistent result that the K^0 contamination is 10% at $x_F = 0.2$ and below 4% at $x_F > 0.4$. The proton background is estimated to be 5% in the inclusive neutron sample used for the asymmetry analysis.

5.2.2 Analysis cut

The neutron kinematic cuts for A_N calculation in this analysis are identical to the previous publication[3]

Kinematic cut

- SMD radial position: $0.5 \text{ cm} < r < 4.0 \text{ cm}$ ($0.3 < \theta < 2.2$)
- ZDC digital sum (ch5+ch6+ch7) energy: $40\text{-}120 \text{ GeV}$ ($x_F > 0.5$)

Based on the studies in the previous section, following neutron identification cuts are applied.

Neutron identification

- Photon rejection
 - #SMD: nx , and $\text{ny} > 1$
 - ZDC: ZDC 2nd module energy / ZDC total energy > 0.03
- Proton rejection (only for Run-08)
 - Charge veto counter: $\text{ADC-pedestal} < 50$ ($=1/2 \text{ MIP peak}$)

5.3 Data set

The $p+p$ data sample was taken from the (original) physics data taking period of the Run-08 and Run-15, and the $p+Al$ and $p+Au$ data samples were taken from the special stores (one store for each) in the Run-15, which was dedicated for this measurement. The ZDC inclusive trigger, requiring minimum 15 GeV energy deposit at the ZDC, collected the inclusive neutron data. A segment of the PHENIX DAQ data taking is called a “run”, and one run corresponds to 90 min. typically. The number of physics runs available for the Run-08 $p+p$ and Run-15 $p+p$ are 170 and 123, respectively.

5.3.1 Run quality assurance

For the run quality assurance, runs having problem in the neutron detectors, trigger, BBC, DAQ, and the spin related systems were rejected.

DAQ

The DAQ stops automatically after 90 minutes of data taking by default. However, the DAQ can be forced to stop earlier whenever any crucial problem which can spoil the data quality is detected online. In order to avoid such data, runs with short DAQ running time were rejected by requiring minimum 5M recorded events (about 15 minutes).

Spin

The spin database records the information of the proton beam(s) online. The information includes the spin pattern and polarization provided by the 12'0

clock polarimetry and bunch-by-bunch luminosity measured by the PHENIX detectors. Runs with following conditions are rejected.

- Spin information is not recorded or flagged as bad.
- The blue beam polarization is zero or nonphysical.
- The shift of the bunch numbering between the PHENIX and RHIC is not 5, which is the default setup so that further cross check is required.
- The intended spin pattern and the measured one mismatch.

Detectors and other operation problems

Runs having logs of ZDC, SMD, and BBC problems in the DAQ database or in the e-logbook were also rejected. These runs have problems such as accidentally disabled high-voltage or malfunction of the electronics.

Result

After the run QA in the above, total 119, 87, 3, and 3 runs were analyzed for Run-08 $p+p$, Run-15 $p+p$, Run-15 $p+Al$, and Run-15 $p+Au$, respectively. The analyzed runs for $p+p$ would be smaller than the other analysis done for the same running because the ZDC inclusive trigger was operated partial period of Run-15, and there were some period that the CV was not functional in Run-08.

5.3.2 Initial event selection

Trigger requirement

The data were collated by the ZDC inclusive trigger, $ZDCN \parallel ZDCS$ (hit at the north ZDC or south ZDC) for $p+p$ and $ZDCN$ (hit at the north ZDC) for $p+A$, which requires minimum ~ 15 GeV energy deposit at the ZDC. In addition, $BBCLL1 \& (ZDCN \parallel ZDCS)$ trigger sample for $p+p$ runs in 2008 was analyzed, which requires hit at both BBCs in addition to the ZDC inclusive trigger. This trigger ran with lower prescale, therefore has relatively large statistics.

BBC requirement

The $ZDC \otimes BBC$ -tag sample requires at least one PMT hit at both the north and the south BBCs, and the $ZDC \otimes BBC$ -veto sample requires no hit at both BBCs. Note that these two sets are mutually exclusive but not complete subsets of the ZDC inclusive sample.

ADC quality cut

As mentioned in Sec. 4.2.3, the ADC gate signals of all channels of the ZDC and SMD are generated by the ZDC analog sum signal. Therefore, any event which has no hit at the ZDC analog sum channel should be rejected in order to falsely measured ADC bit. To reject such events, 30 GeV minimum energy deposit and the TDC non-overflow bit, $TDC0 < 3800$ and $TDC1 < 3800$, at the ZDC analog sum channel were required.

After the Run QA and the ADC quality cut, the number of analyzed events are shown in Table 5.1.

5.3.3 Dead channel

For the whole Run-08 data, among the eight horizontal SMD strips, which gives the y -position reconstruction, the most bottom strip was disabled. Since

| Data | Sample | # events |
|--------------|------------------------|----------|
| p+p (Run8) | | 5.4 M |
| p+p (Run8) | ZDC \otimes BBC-tag | 18 M |
| p+p (Run8) | ZDC \otimes BBC-veto | 1.7 M |
| p+p (Run15) | | 35 M |
| p+p (Run15) | ZDC \otimes BBC-tag | 140 M |
| p+p (Run15) | ZDC \otimes BBC-veto | 8.0 M |
| p+Al (Run15) | | 12 M |
| p+Al (Run15) | ZDC \otimes BBC-tag | 4.6 M |
| p+Al (Run15) | ZDC \otimes BBC-veto | 3.4 M |
| p+Au (Run15) | | 5.9 M |
| p+Au (Run15) | ZDC \otimes BBC-tag | 1.2 M |
| p+Au (Run15) | ZDC \otimes BBC-veto | 3.4 M |

Table 5.1: The number of analyzed events.

it gives y -position, significant effect was not expected on the left-right asymmetry. This effect was estimated by enabling and disabling the same channel with the Run-15 data. As a result, it gave 0.3% of differences on the $p+p$ ZDC inclusive A_N , which is an order smaller than the other uncertainties. Therefore, no correction was done for this disabled channel.

5.3.4 Polarization

The beam polarization is measured by the carbon target polarimeter and then normalized by the H-jet polarimeter in the RHIC. The average polarization values are 0.515 ± 0.002 for $p+p$, 0.59 ± 0.02 for $p+Al$, and 0.59 ± 0.04 for $p+Au$. Fig. 5.2 shows the fill-by-fill polarization values of Run-08 $p+p$, and the run-by-run polarization values of Run-15 $p+p$. The run-by-run polarization values are available in Run-15 because not only the store-averaged-polarization, but also the decay of the polarization (dP/dt) by the time is provided. This information is useful in Run-15 where a running time of one store became longer because there is a possibility that a run polarization value becomes different significantly from a store-averaged-polarization value. As a

result, shown in Fig. 5.2, run polarization values in a store vary within 20%.

The global uncertainty of polarization is 3% [80, 81]. This uncertainty is from the normalization of the pC polarimeter measurement.

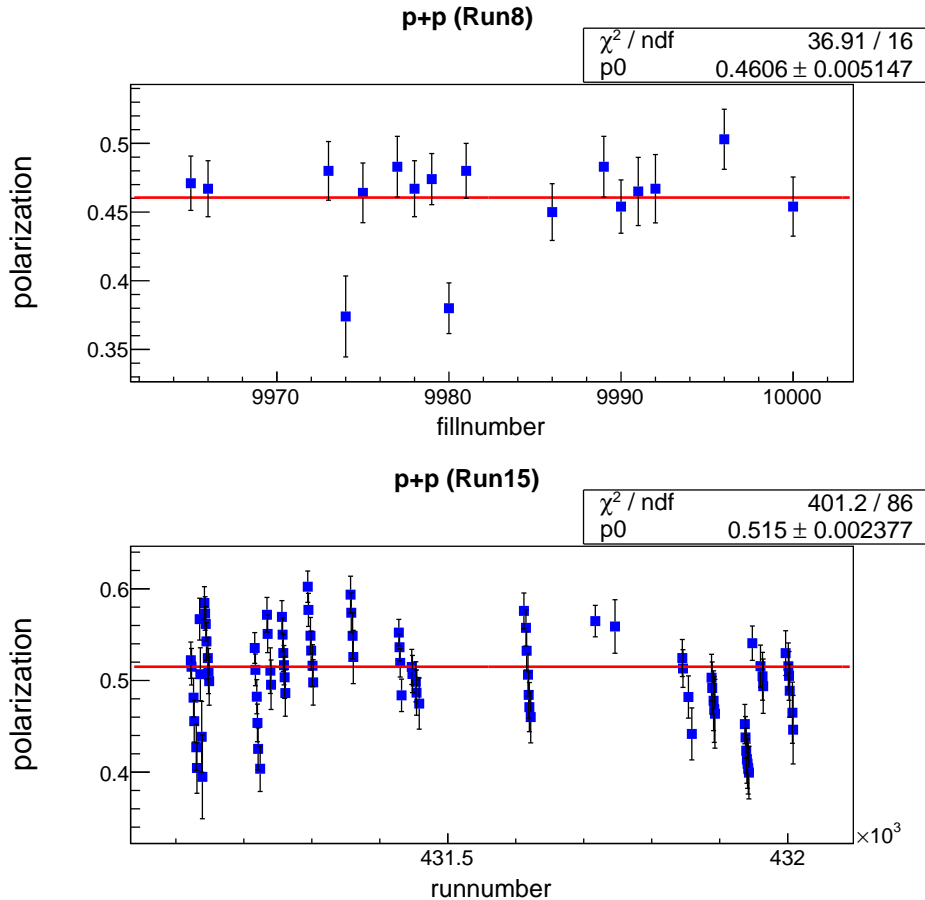


Figure 5.2: Polarization of blue beam in Run-08 (top) and Run-15 (down) $p+p$.

5.4 Calibration

See Sec. 5.11.5 for the systematic uncertainties from calibrations.

5.4.1 ZDC pedestal calibration

The pedestal of each channel is scanned by the LED. The LED signal is required at least one channel of the ZDC module in order to get correct ADC values for all channels (see Sec. 4.2.3). To get pedestal values, the PMT HV was on for only one channel and off for the rest two channels, and the pedestal values of the rest two channels were measured. The pedestal peak can be seen in Fig. 5.3.

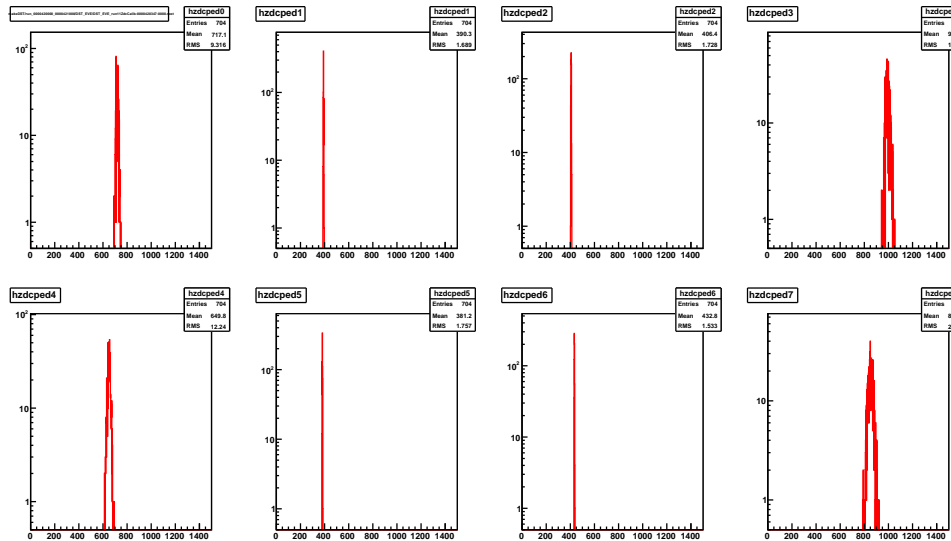


Figure 5.3: ZDC LED pedestal scan results for all eight channels. ADC distributions with ZDC PMT HV of ch1, ch2, ch5, and ch6 off. In this figure, total 8 channels are shown since the south ZDC, which is not used in this analysis, is also included

5.4.2 SMD position reconstruction

Pedestal calibration

To select SMD pedestal events, following cuts are applied on the ZDC trigger samples with the initial event selection (Sec. 5.3.2).

- $\text{zdc_ene}[6] < 10$ (2nd ZDC module) for EM shower selection
- $\text{zdc_rawadc}[39] < 710$ (SMD analog sum channel, pedestal+pedestal rms)

These cuts enhance electromagnetic shower events, which mostly lose all energy in the first ZDC module, before the SMD.

Fig. 5.4 shows ADC distribution of the pedestal events and fit result of an SMD channel.

Position reconstruction principle

The neutron position is calculated as

$$x = \frac{\sum_i^{\#SMD} E(i) \cdot x(i)}{\sum_i^{\#SMD} E(i)} \quad (5.1)$$

where $E(i)$ and $x(i)$ are energy and position of i -th SMD scintillator strip, and $\#SMD$ are the number of strips with signals over the threshold cut, which is about one MIP peak (1~3 MeV) of a strip. The position of i -th strip is calculated as

- Vertical strip: $x(i) = (i-3.0)*(1.5*11.0/10.5)$ cm (lower i is at the left)
- Horizontal strip: $y(i) = (i-3.5)*(2.0*11.0/10.5/\sqrt{2})$ cm (lower i is at the bottom)^I

^IFor Run-08, channel map was different (see ZDC elog entry 88).

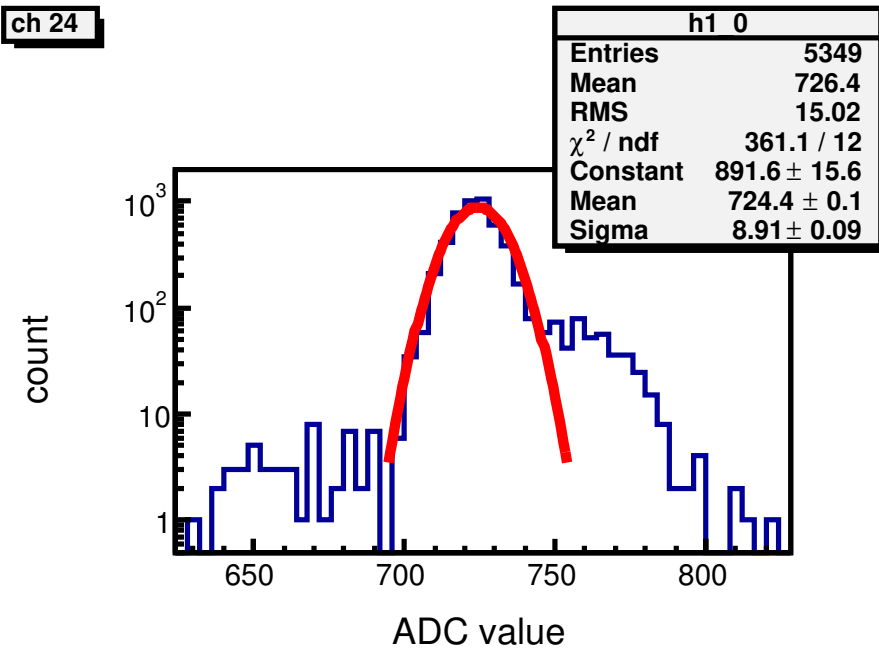


Figure 5.4: SMD pedestal fit.

where 1.5 (2.0) is one vertical (horizontal) strip width, 11.0/10.5 is correction for [total width]/[1.5 x 7 total strips], and $\sqrt{2}$ is for 45 degrees tilt.

Relative gain matching between channels

From Eq. 5.1, absolute gain calibration of SMD is not necessary, but relative gain between all vertical (horizontal) strips should be done. SMD gain calibration is done by fitting ADC distribution of each strip with a function

$$h_{\text{narrow}} \exp\left(-\frac{(x - x_0)}{w_{\text{narrow}}}\right) + h_{\text{wide}} \exp\left(-\frac{(x - x_0)}{w_{\text{wide}}}\right) \quad (5.2)$$

where h_{narrow} (h_{wide}) and w_{narrow} (w_{wide}) are fitting parameters of fastly (slowly) dropping exponential function, and x is ADC value of an event, and

x_0 is ADC value of pedestal peak. Fig. 5.5 shows fitting for gain matching.

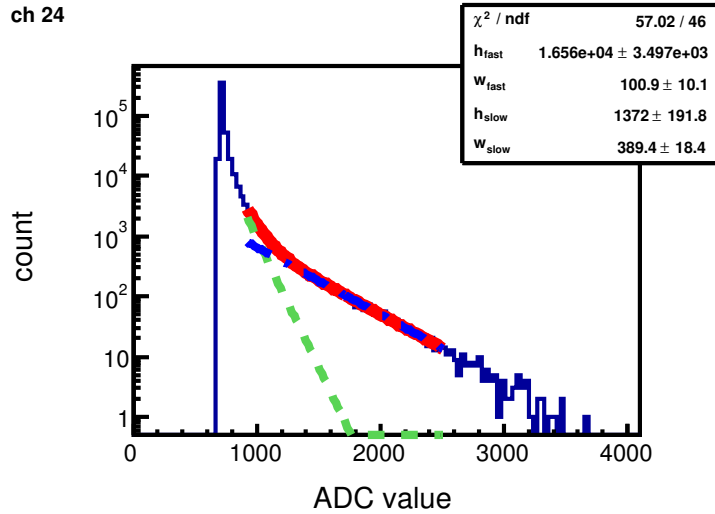


Figure 5.5: Eq. 5.2 fitting result of a strip.

We assumed w_{narrow} ($\propto w_{wide}$ my) is proportional to the gain of each strip within all vertical (horizontal) strips. The SMD charge of each strip is then calculated as

$$E(i) = (\text{ADC} - \text{pedestal}) \frac{1}{w_{narrow}}. \quad (5.3)$$

II

Gain matching between Run-08 and Run-15

Figure 5.6 shows the x-distributions depending on the SMD threshold cut. Different threshold gives different x-distribution. The gain matching between the Run-08 and Run-15 is required in order to apply the same physical SMD threshold value. As shown in the Fig. 5.7, the SMD gain of Run-08 is higher than that of Run-15. Relative gain between Run-08 and Run-15 are matched

^{II}There is a study which compared SMD gain between one from this fitting, and another from the radiation source calibration during the Run15 maintainance, done for north SMD vertical strips. The result shows a correlation.

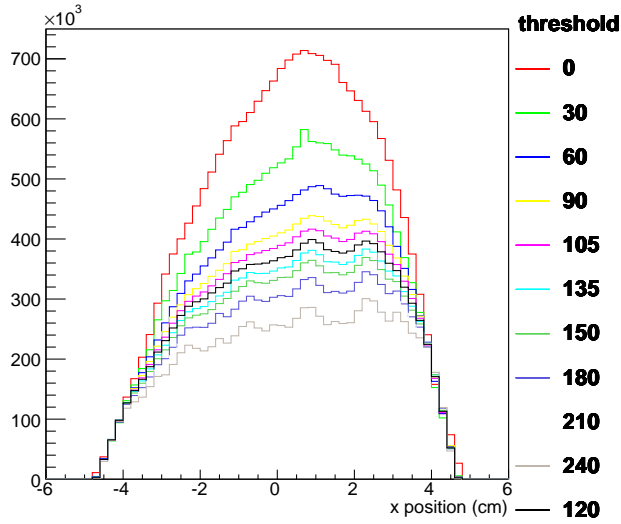


Figure 5.6: X distribution with different threshold cut in Run-15 p+p ZDC inclusive sample. 40 is the threshold of asymmetry analysis.

by matching the average charge sum of all strips between that of Run-08 and Run-15.

Fig. 5.7 (Fig. 5.8) shows ADC distribution of each SMD channel of neutrons before (after) the gain matching. Fig. 5.9 and Fig. 5.9 shows x and y distribution of Run-08 and Run-15 after their relative gain matching. Compare Fig. 5.6, the relative gain of both x and y positions are well matched between Run-08 and Run-15. The difference in the y position shape between the Run-08 and Run-15 comes from one dead channel in Run-08 at the most negative y .

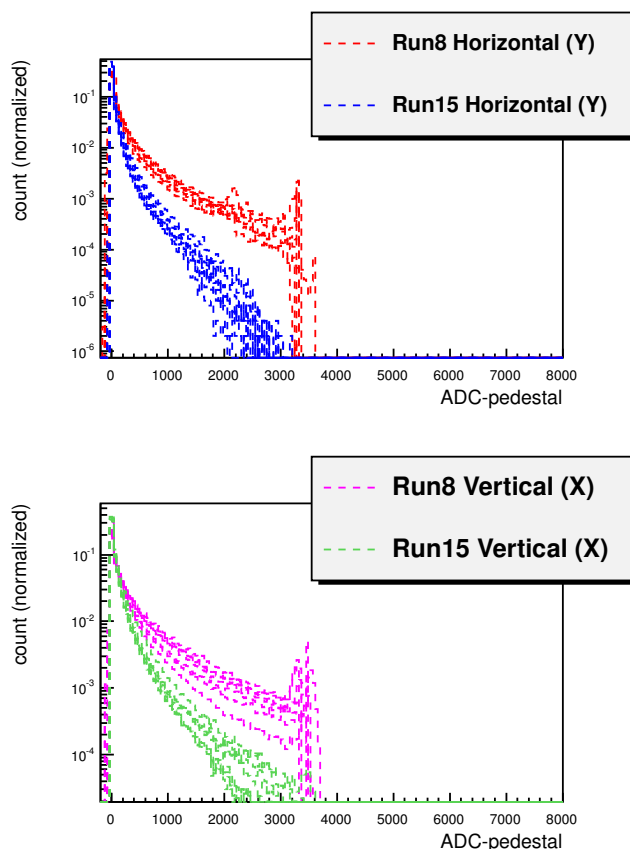


Figure 5.7: Before the SMD gain matching. The plots shows the pedestal subtracted ADC distributions of all channels before (after) the gain matching.

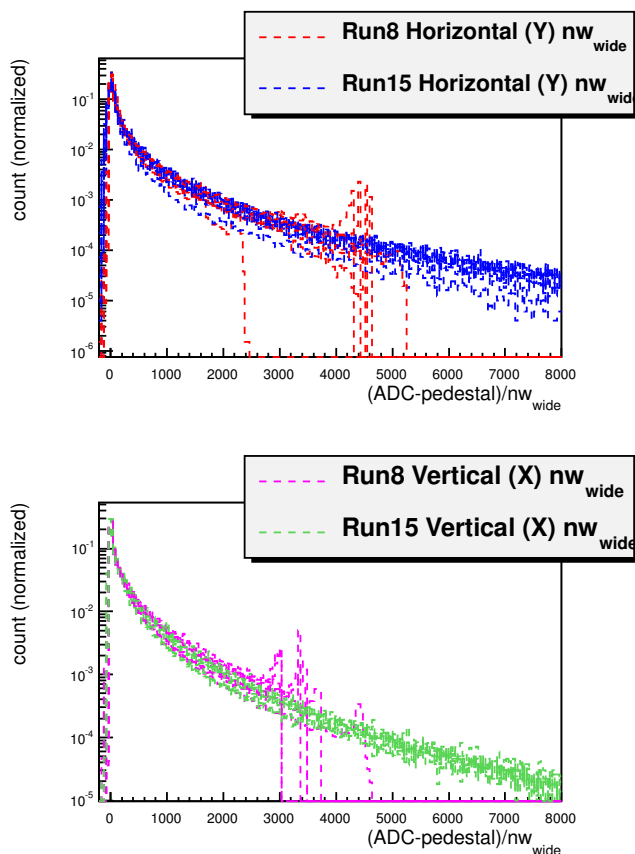


Figure 5.8: After the SMD gain matching.

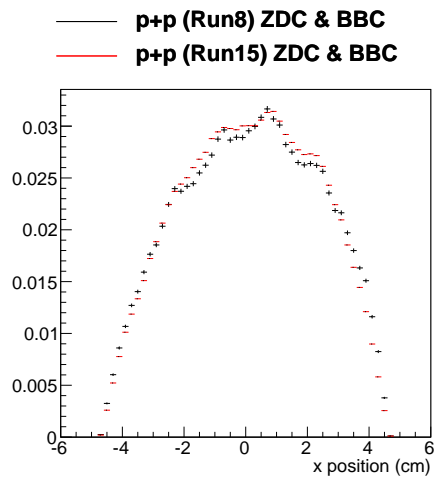


Figure 5.9: X position of ZDC \otimes BBC-tag samples of Run-08 and Run-15.

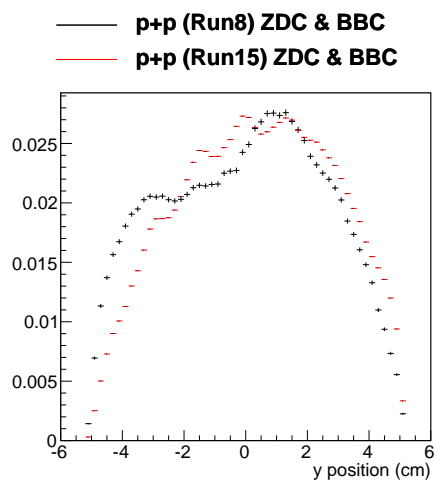


Figure 5.10: Y position of ZDC \otimes BBC-tag samples of Run-08 and Run-15.

5.4.3 ZDC gain

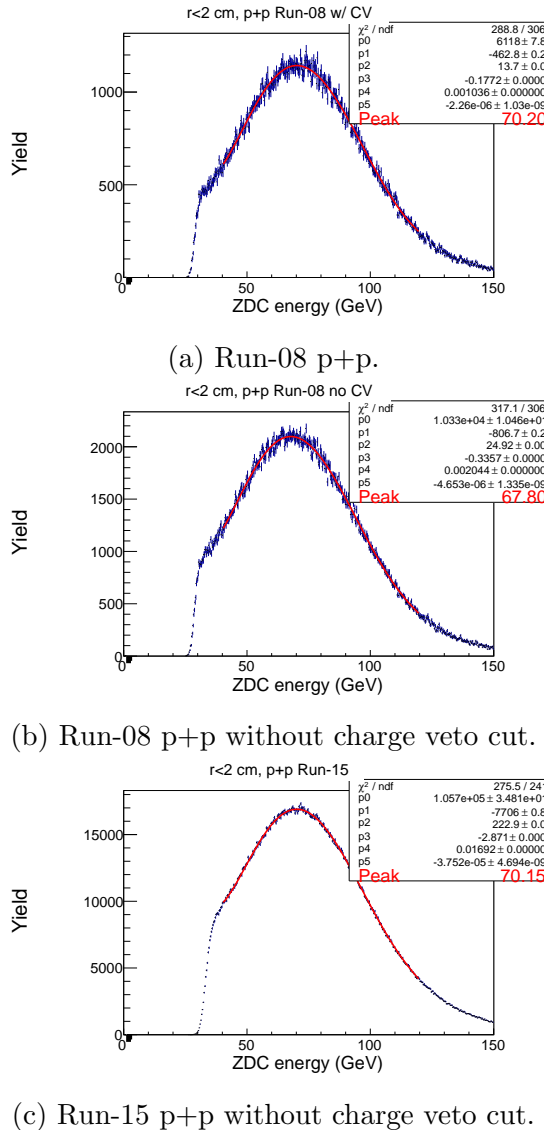


Figure 5.11: ZDC energy distribution at $r < 2.0$ cm of neutron identified events from ZDC inclusive sample.

The absolute ZDC energy scale is normalized by 70 GeV measured energy

peak of ZDC inclusive sample at $r < 2.0$ cm acceptance in $p+p$ collisions after neutron identification [3]. The energy distribution is fitted with polynomials. Fig. 5.11 shows calibration result of Run-08 and Run-15. Since we cannot apply charge veto cut on Run-15 data, the energy distribution of Run-08 without charge veto cut is also shown in order to examine if the proton background contamination change the peak position. The peak is changed only by 2 GeV. This can be explained by Fig. 5.1b that proton energy distribution continuously drops as its energy grows whereas neutron shows peak around 70 GeV, therefore, proton backgrounds do not change neutron peak position significantly. According to background estimation in Sec. 5.2, we have fewer proton background in Run-15, so we adjust Run-15 ZDC energy peak at 70 GeV.

5.4.4 CV MIP peak calibration

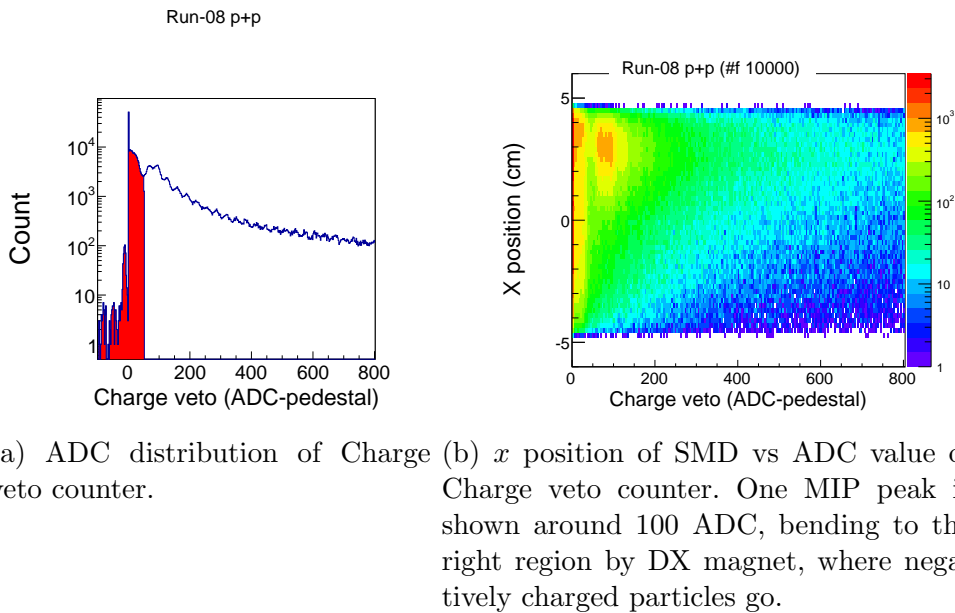


Figure 5.12: Charge veto counter (CV) events.

Fig. 5.12a shows the ADC distribution of Charge veto counter (CV) for “BBC vetoed” sample. The red region ($\text{ADC} < 50$) corresponds to the “charge vetoed” events. From Fig. 5.12b, one MIP peak is shown around 100 ADC, which comes from single proton that bending to the right region by DX magnet, where negatively charged particles go. The $\text{ADC}=50$ cut corresponds to the half of one MIP peak.

5.5 BBC taggings

Figure 5.13 shows number of fired PMT distributions of BBC south (left), and BBC north (right) after neutron analysis cuts.

For the BBC correlation study, following BBC tagging samples are made in the publication of this analysis [76]. “Hit (veto)” means at least one PMT is fired (no PMT is fired) at the corresponding side of BBC.

1. ZDC inclusive: no BBC taggings (inclusive neutron)
2. ZDC \otimes BBC-tag: hit at both BBCs
3. ZDC \otimes BBC-veto: veto both BBCs

In addition, two more samples are also presented in Sec. 6.

4. ZDC \otimes p-dir BBC-veto \otimes A-dir BBC-tag: hit at south BBC (A beam going direction, further BBC from the ZDC) and veto north BBC
5. ZDC \otimes p-dir BBC-tag \otimes A-dir BBC-veto: hit at north BBC (proton beam going direction, nearer BBC to the ZDC) and veto south BBC

Compare to 1-3 BBC tagging samples, the preliminary analysis of 4-5 samples was identical except two steps. One is that the background is not subtracted, but assigned as 20% of the systematic uncertainty. The number came from attributing the \sim 20% smaller Run-15 ZDC inclusive and ZDC \otimes BBC-tag A_N^{fit} values than those of Run-05 to the contribution of zero charged background asymmetry in Run-15, then assumed to be same for all samples. The other was different smearing correction factor (we applied Run-05 value for the 4-5 samples), but the difference was covered by the systematic uncertainty. Note that those four BBC tagging samples (2-5) are mutually exclusive and complete subsets of the ZDC inclusive sample (1).

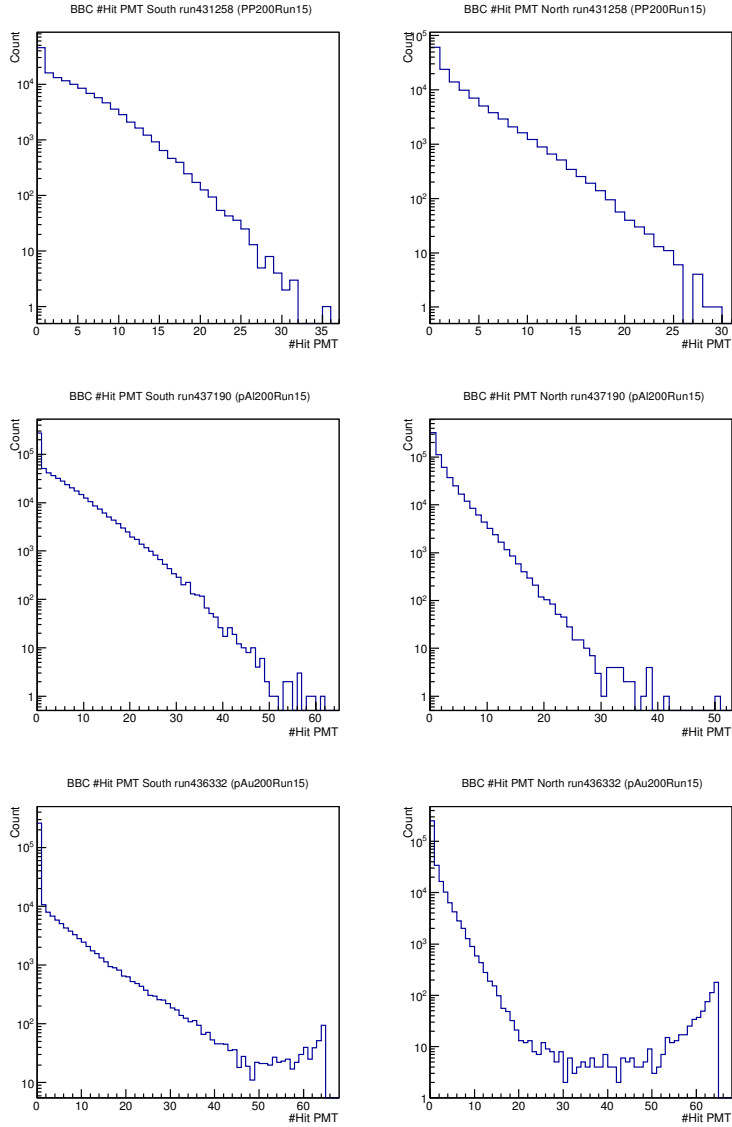


Figure 5.13: Number of fired PMT distribution of BBC south (left), and BBC north (right) after neutron analysis cut. Figures are for $p+p$, $p+Al$, and $p+Au$ from the top to the bottom.

5.6 Energy spectra of neutron samples

Figure 5.14 shows the ZDC energy spectra of inclusive (red), $ZDC \otimes BBC$ -tag (green), and $ZDC \otimes BBC$ -veto (blue) samples of Run-15 data after all of the asymmetry analysis cuts in Sec. 5.2.2 except the energy cut are applied. From comparing the shape of the histogram to that of $ZDC \otimes BBC$ -tag ($ZDC \otimes BBC$ -veto) for each system, it is observed that as A increases, the contribution from $ZDC \otimes BBC$ -veto sample increases in sample. We can notice that the analyzed energy distribution of each sample is different each other. Comparing to the energy distributions of $ZDC \otimes BBC$ -veto samples, that of $ZDC \otimes BBC$ -tag samples are more shifted to the lower energy for all collision systems. This can be interpreted as neutrons from small momentum transfer processes are enhanced in $ZDC \otimes BBC$ -veto sample, whereas neutrons from hard scattering, which distribute relatively less energy to neutrons, are enhanced in $ZDC \otimes BBC$ -tag sample, which are consistent to the simulation study.

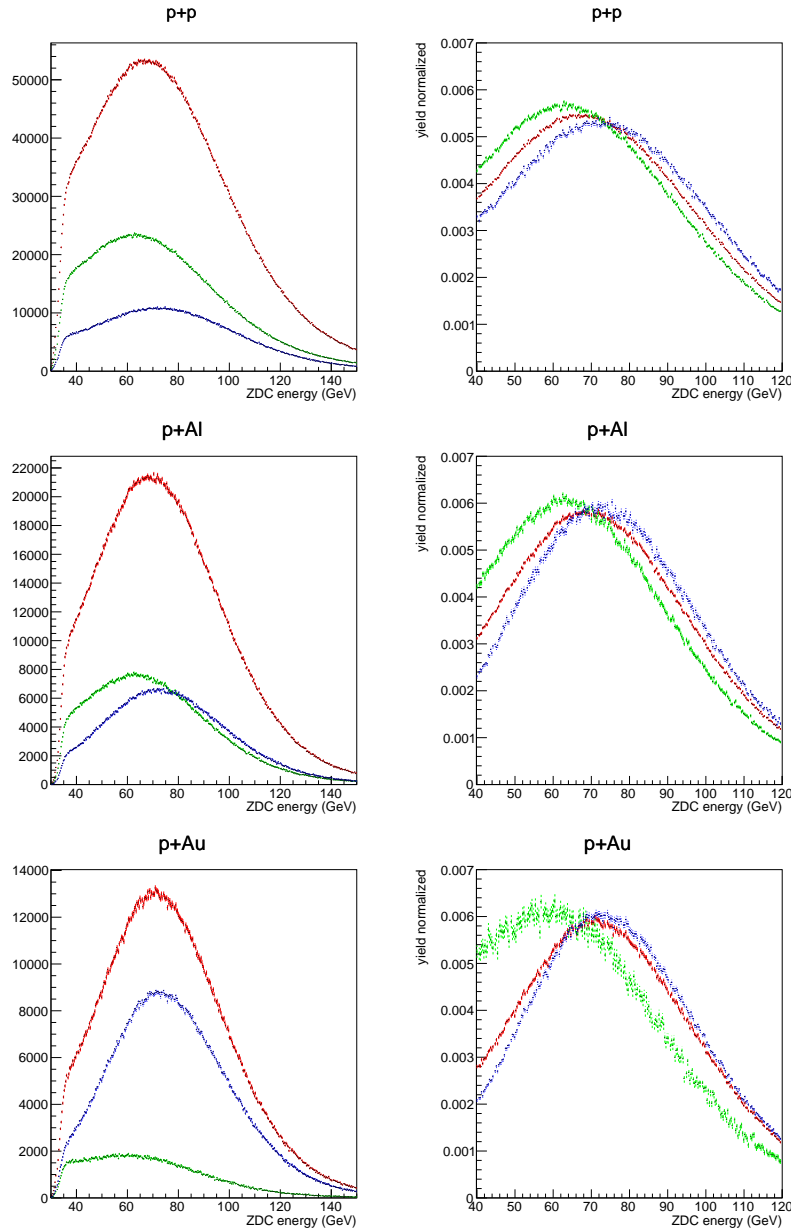


Figure 5.14: $p+p$. ZDC energy spectra for inclusive (red), ZDC \otimes BBC-tag (green), and ZDC \otimes BBC-veto (blue). The plots in the left show raw yield, and normalized yields (the integral of a histogram is 1) are drawn in the right for better comparison of shapes between trigger samples. The species of colliding particles are written in each plot. All of the asymmetry analysis cuts in Sec. 5.2.2 except the energy cut are applied in these data.

5.7 p_T spectra

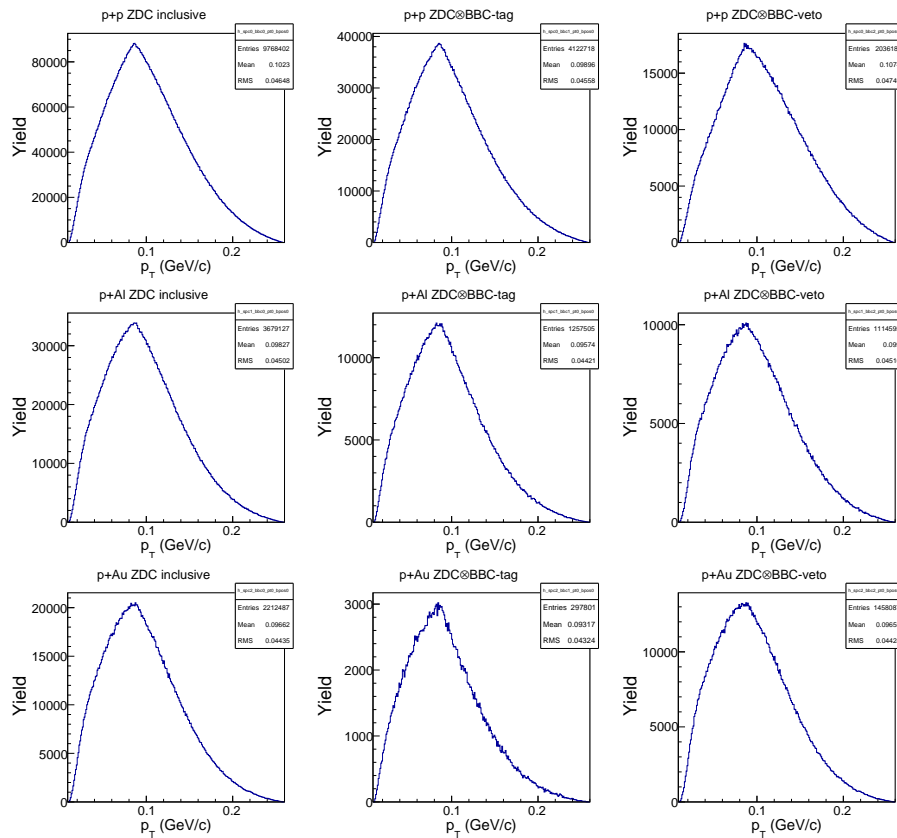
Figure 5.15 shows p_T spectrum of each sample. Transverse momentum p_T in lab frame is calculated as

$$p_T = \sqrt{E^2 - m_n^2} \sin \theta. \quad (5.4)$$

where θ is the scattering angle. In the nearly zero-degree region, θ can be obtained as

$$\theta \approx r/d \quad (5.5)$$

where r is radial distance from the beam axis, and d is the distance between the ZDC and collision point. From the ZDC position survey, d is 1856 cm in $p+A$ runs. The range of p_T with the kinematic cuts corresponds to 0.01-0.26GeV/c. The p_T distribution of each sample is slightly different between each other. For the p_T dependent A_N^S calculation, we divided the p_T bins into four with equal intervals. Number of neutrons in each bin can be found in Fig. 5.21.

Figure 5.15: p_T spectrum of neutron sample.

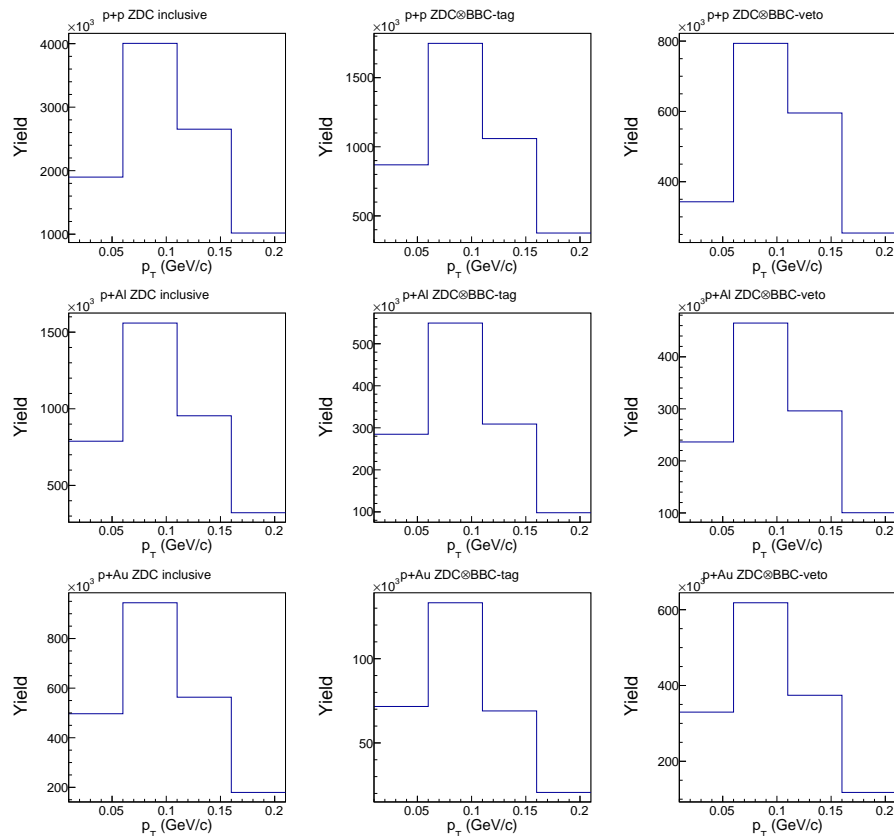


Figure 5.16: Neutron yield of each p_T bin. p_T spectrum is equally binned:

5.8 Asymmetry measurement

5.8.1 Raw asymmetry ϵ_N

The raw asymmetry is measured by using the square-root formula as

$$\epsilon_N(\phi) = \frac{\sqrt{N_\phi^\uparrow N_{\phi+\pi}^\downarrow} - \sqrt{N_{\phi+\pi}^\uparrow N_\phi^\downarrow}}{\sqrt{N_\phi^\uparrow N_{\phi+\pi}^\downarrow} + \sqrt{N_{\phi+\pi}^\uparrow N_\phi^\downarrow}} \quad (5.6)$$

where $N_{\phi(\phi+\pi)}^{\uparrow(\downarrow)}$ is the number of neutrons detected at azimuthal angle ϕ ($\phi + \pi$) bin when the beam polarization direction is up (down). The acceptance area is divided into 16 azimuthal bins for this calculation as shown in Fig. 5.17. With this square-root formula, possible systematic uncertainties from the left-right asymmetric detector efficiency and relative luminosity between beams with up and down polarizations can be ignored.

5.8.2 Polarization normalized asymmetry A_N^{fit}

The raw asymmetry $\epsilon_N(\phi)$ is proportional to the beam polarization value P . As shown in Fig. 5.2, the P varies. To get physically meaningful asymmetry, $\epsilon_N(\phi)/P$ is separately measured for each polarization measurement.

From Fig. 5.18 to 5.20, $\epsilon_N(\phi)/P$ results are shown. ZDC inclusive samples shows clear nuclear dependence of A_N^{fit} , including a sign change from negative in $p+p$ collisions to positive in $p+\text{Au}$ collisions. Also, the behaviour is very different between each BBC tagging sample. Each histogram is fit by sin function in order to get the polarization normalized asymmetry A_N^{fit} as

$$\frac{\epsilon_N(\phi)}{P} = A_N^{\text{fit}} \sin(\phi - \phi_0) \quad (5.7)$$

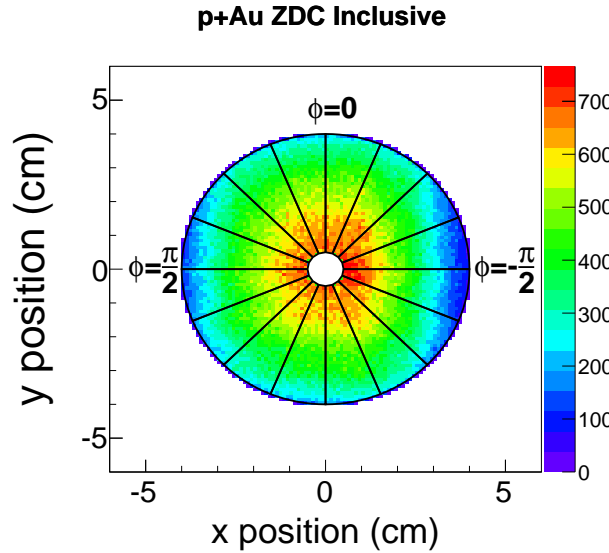


Figure 5.17: Neutron distribution in $p+\text{Au}$ collisions shown with 16 azimuthal bins for raw asymmetry $\epsilon_N(\phi)$ calculation.

where ϕ_0 is the transverse polarization direction. ϕ_0 is zero within statistical uncertainty in 2015, and 0.32 rad in Run-08 PHENIX forward π^0 analysis [82].

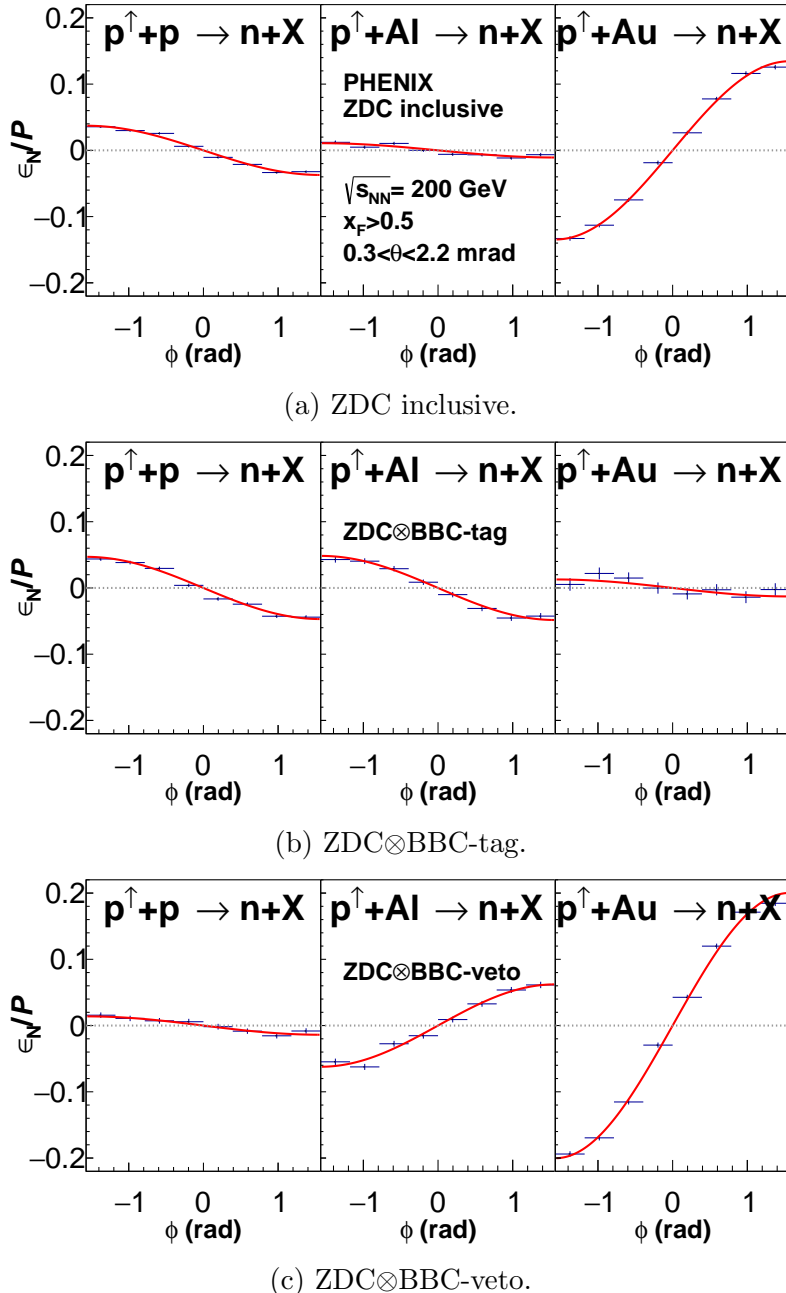


Figure 5.18: A_N^{fit} histogram of each collision system, for ZDC inclusive, ZDC \otimes BBC-tag, and ZDC \otimes BBC-veto samples in Run-15 from the top to bottom. Fit results are in table 5.2.

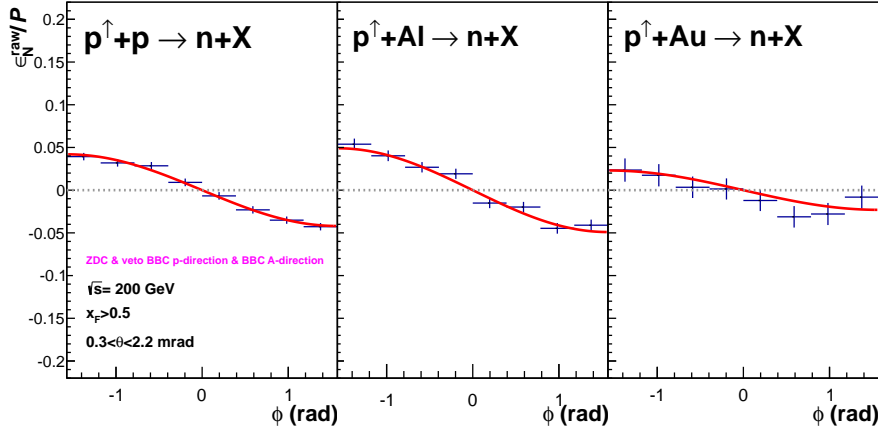


Figure 5.19: A_N^{fit} histogram of each collision system, for ZDC \otimes p-dir BBC--veto \otimes A-dir BBC-tag

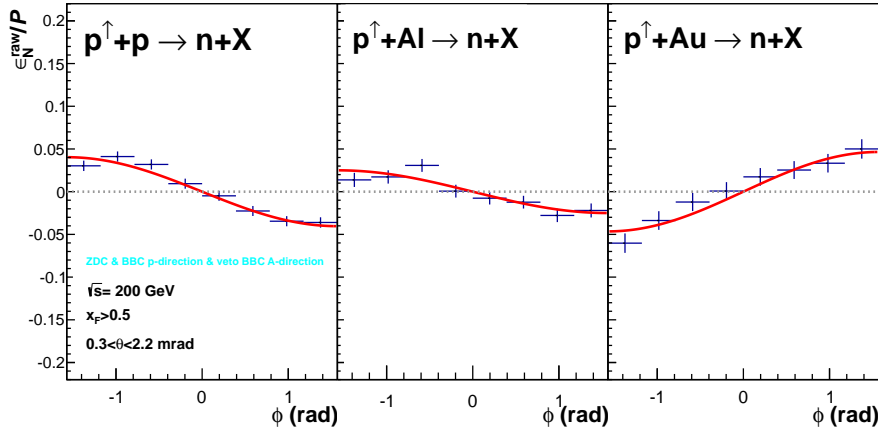


Figure 5.20: A_N^{fit} histogram of each collision system, for ZDC \otimes p-dir BBC--tag \otimes A-dir BBC-veto

p_T dependence

From Fig. 5.21 to 5.23, $\epsilon_N(\phi)/P$ results of different p_T bins are shown for ZDC inclusive, ZDC \otimes BBC-tag, and ZDC \otimes BBC-veto samples.

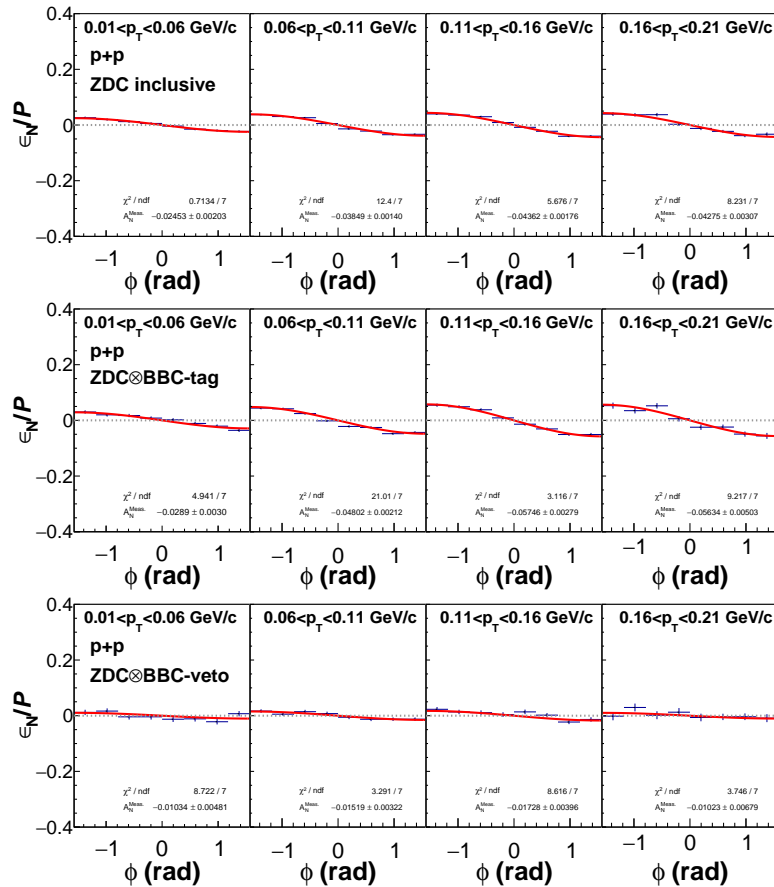
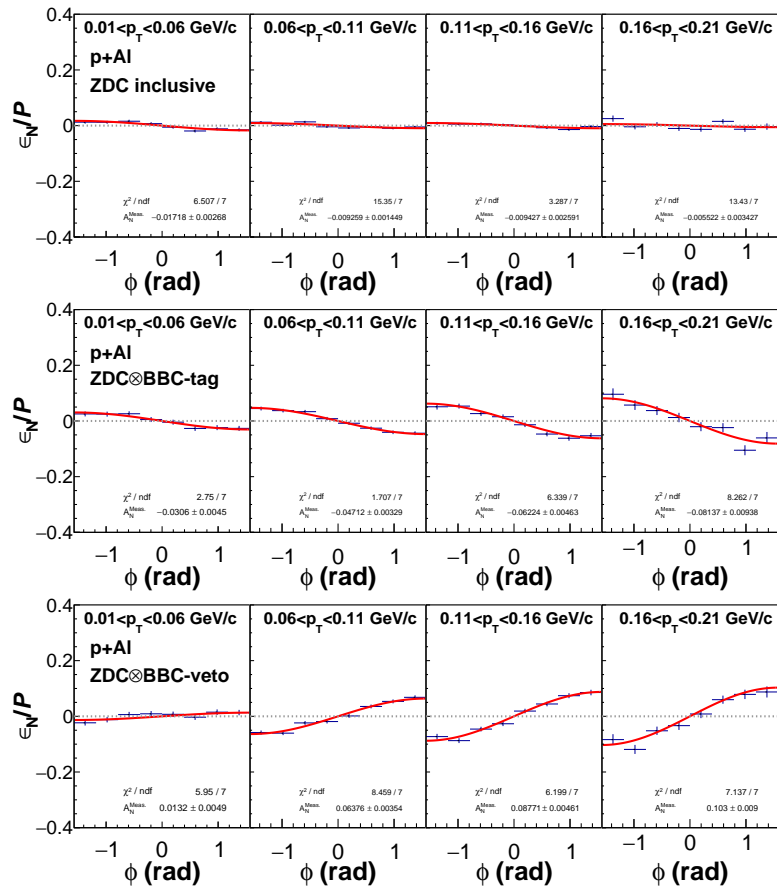
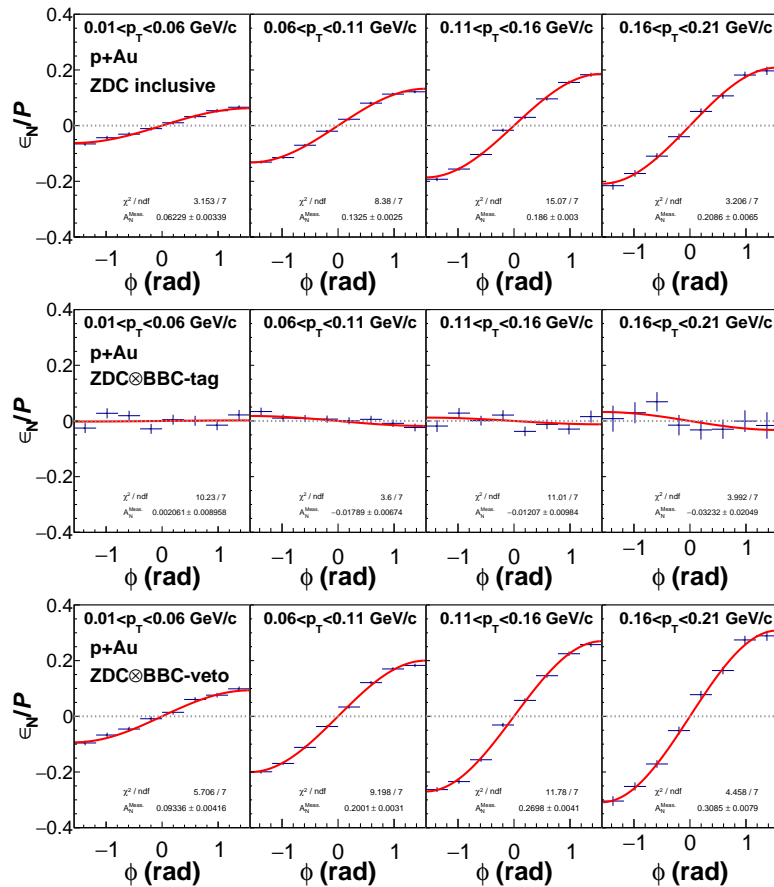


Figure 5.21: A_N^{fit} for different measured p_T bins, Run-15 $p+p$.

Figure 5.26 shows the A_N^{fit} as a function of p_T . A p_T data point represents average p_T value of each bin.

Figure 5.22: A_N^{fit} for different measured p_T bins, Run-15 $p+\text{Al}$.

Figure 5.23: A_N^{fit} for different measured p_T bins, Run-15 $p+\text{Au}$.

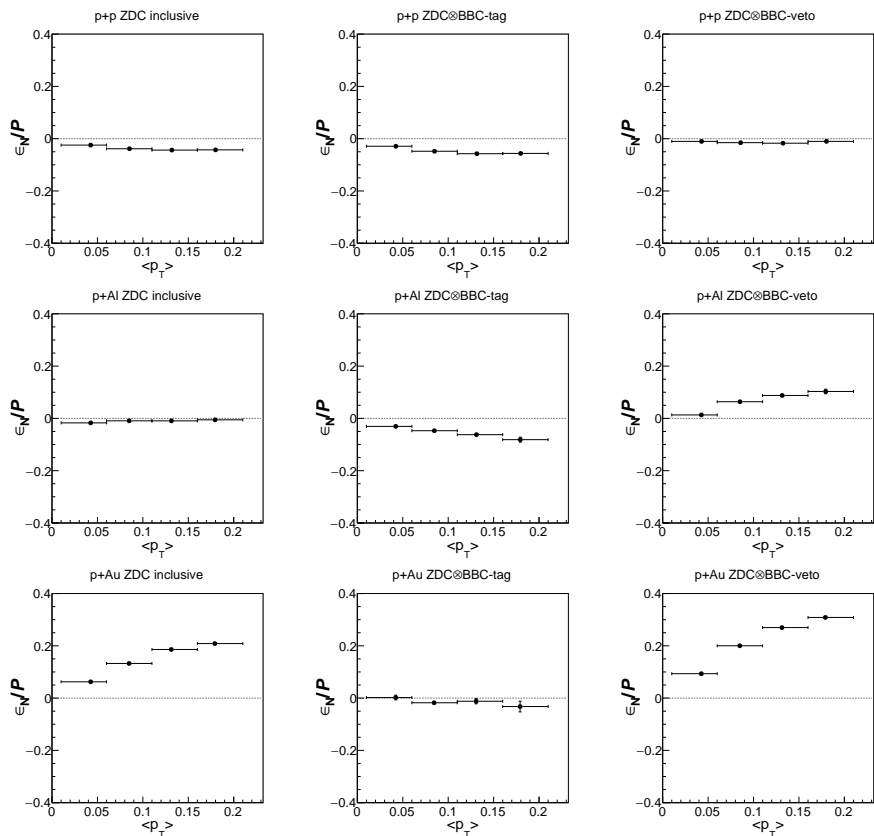


Figure 5.24: A_N^{fit} of measured p_T samples of Run-15 $p+p$, $p+Al$, and $p+Au$ from the top to bottom.

With and without charge veto cut in Run-08

For the background asymmetry measurement, all Run-08 samples are measured for the with and without the charge veto cut for comparison. Both p_T binned and integrated A_N^{fit} are analyzed for ZDC inclusive, ZDC \otimes BBC-tag, and ZDC \otimes BBC-veto samples. Results are summarized in Table 5.2 and Fig. 5.26. The subtraction of background is explained in Sec. 5.9.

| samples | CV cut | $A_N^{fit} \pm stat.$ | syst. polarization |
|------------------------|--------|-----------------------|---------------------|
| ZDC | done | -0.0439 ± 0.0034 | ± 0.0007 (1.7%) |
| ZDC | | -0.0321 ± 0.0025 | ± 0.0006 (1.7%) |
| ZDC \otimes BBC-tag | done | -0.0642 ± 0.0058 | ± 0.0012 (1.8%) |
| ZDC \otimes BBC-tag | | -0.0460 ± 0.0014 | ± 0.0006 (1.3%) |
| ZDC \otimes BBC-veto | done | -0.0231 ± 0.0071 | ± 0.0011 (5.0%) |
| ZDC \otimes BBC-veto | | -0.0141 ± 0.0050 | ± 0.0008 (5.9%) |

Table 5.2: Run-08 A_N^{fit} summary with statistical uncertainty and systematic uncertainty from polarization only. The “done” in the “CV cut” column means that the charge veto cut is applied.

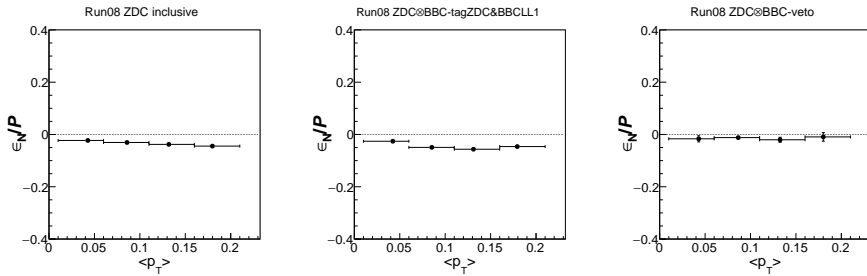


Figure 5.25: A_N^{fit} of measured p_T samples, Run-08 $p+p$.

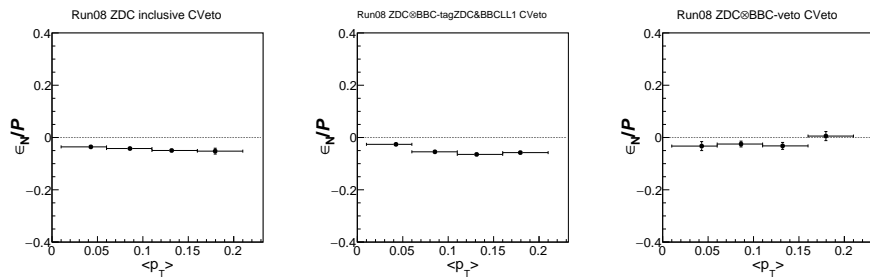


Figure 5.26: A_N^{fit} of measured p_T samples, Run-08 $p+p$ with charge veto cut.

5.9 Background subtraction

5.9.1 Proton background simulation for $p+p$

As can be seen in Fig. 5.1b, the proton background is significant without charge veto cut, which is not applicable in Run-15. sensitive to the alignment of apparatus

Therefore we developed an alternative way to subtract proton background in the asymmetry calculation based on its characteristic x -distribution in the SMD.

X-distribution of neutron and background

Figure 5.28 shows the x -distribution of the shower reconstructed by the SMD using PYTHIA6 and GEANT3 for neutrons (blue), protons (red), and all particles (black) of ZDC inclusive (left), ZDC \otimes BBC-tag (middle), and ZDC \otimes BBC-veto (right) samples.

We categorized proton background for the two types: 1) protons from elastic and single diffractive (the beam proton stays intact) scatterings, which scattered away from the beam orbit and contribute the peak on the right (or positive x , see Fig. 5.28 left); and 2) protons from the other processes, mainly hard scatterings and double diffractive processes, which give even x -distribution (see Fig. 5.28 right). We call the former as the “asymmetric” background and the latter as the “symmetric” background.

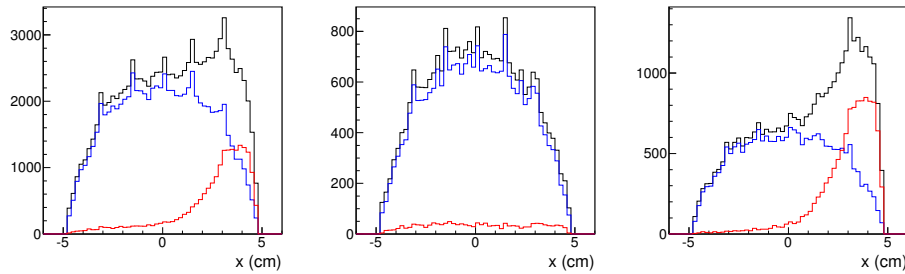


Figure 5.27: PYTHIA+GEANT simulation: x-distribution of the showers in the ZDC reconstructed by the SMD for protons (red), neutrons (blue), and all particles (black) for pp collisions in ZDC inclusive (left) ZDC \otimes BBC-tag (middle) and ZDC \otimes BBC-veto triggered samples.

Categorizing proton backgrounds - “asymmetric” and
“symmetric”

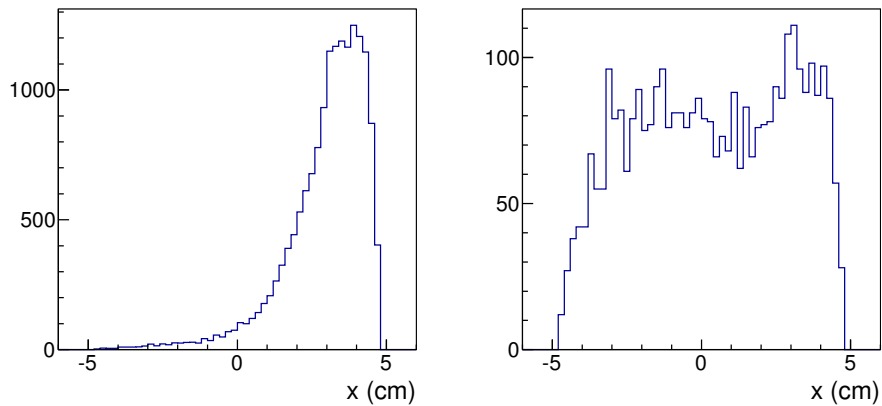


Figure 5.28: PYTHIA+GEANT simulation: x-distribution of the showers in ZDC reconstructed by the SMD for protons from elastic and single diffractive scatterings leaving beam proton intact (left), and hard scattering and double diffractive processes (right).

Background fraction evaluation

Figure 5.27 shows the x-distribution of protons (red), neutrons (blue), and all particles (black) for pp collisions in ZDC inclusive (left) ZDC \otimes BBC-tag (middle) and ZDC \otimes BBC-veto triggered samples. As shown in Fig. 5.28, contamination of the asymmetric proton backgrounds makes the peak in the right. These are prominent in the ZDC inclusive sample, even more clear in the ZDC \otimes BBC-veto sample, whereas completely suppressed in the ZDC \otimes BBC-tag sample because beam proton stays intact in both elastic and diffractive processes, therefore, asymmetric background events do not fire the north BBC.

The background fractions estimated by simulation are 19%, 6%, and 32% for the ZDC inclusive, ZDC \otimes BBC-tag, and ZDC \otimes BBC-veto, respectively. In principle, the background fraction in the ZDC inclusive and ZDC \otimes BBC-veto samples can be evaluated from the x-distributions by counting the excess of the events in the right. However, unlike in the simulation, there is an uncertainty in the SMD gain matching in the real data, therefore, the x-distribution of pure neutrons would not be symmetric either. Therefore, for fare comparison, the excess of counts in the right is evaluated by comparing the x-distribution of the ZDC \otimes BBC-tag, which is not distorted by the asymmetric background. Figure 5.29 shows the x-distribution of ZDC \otimes BBC-tag sample (red) and ZDC (ZDC \otimes BBC-veto) sample on the left (right) plot. The spectra are normalized to the same value in the range $x < 1$ cm. The right excess is 14% and 28% for the ZDC inclusive and ZDC \otimes BBC-veto samples, respectively. These values are slightly different from the background fraction because of the contribution of the symmetric background, which cannot be measured by this approach, 3% and 1.5% correspondingly, and \sim 10% underestimated asymmetric background due to the tail of the asymmetric background in the left side of the x-distribution (see Fig. 5.28 left).

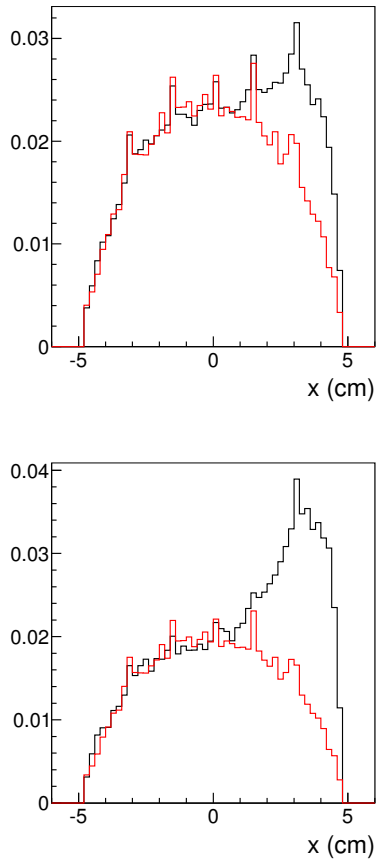


Figure 5.29: PYTHIA+GEANT simulation: x-distribution of the showers in ZDC reconstructed by SMD in ZDC \otimes BBC-tag sample (red) and ZDC (ZDC \otimes BBC-veto) sample on the top (bottom) plot; spectra are normalized to the same value in the range $x < 1$ cm.

Background evaluation procedure for the data

The background fraction of data is evaluated as follow. The asymmetric backgrounds in the ZDC inclusive and ZDC \otimes BBC-veto samples are estimated by the x-distributions of data with comparison to the ZDC \otimes BBC--tag sample. Then the tail effect is corrected by $(10\pm10)\%$. The symmetric backgrounds in all samples are estimated by the simulation. In the previous

study [3], there is an indication that the background in the data may a factor of 2 larger than that of PYTHIA. Therefore, the symmetric background fraction is corrected by a factor of 2 with conservative 100% uncertainty, $(6\pm 3)\%$, $(12\pm 6)\%$, and $(3\pm 1.5)\%$ for the ZDC inclusive, ZDC \otimes BBC-tag, and ZDC \otimes BBC-veto samples, respectively. The details and the results can be found in Sec. 5.2.

5.9.2 $p+A$ collisions

Basically, the background fractions are estimated conservatively and assigned as the systematic uncertainty without subtraction.

Asymmetric background

In contrast to $p+p$ collisions, every data sample doesn't have excess in the right within 2%. We think the asymmetric background is suppressed in $p+A$ because of different beam orbit and the horizontal relocation of ZDC. The suppression of the asymmetric background in $p+A$ can be explained in Fig. 5.30. Figure 5.30 shows the proton trajectory in pp setup (left) and in pA setup (right) for the unscattered beam proton (black), elastically scattered by 4 mrad (red), and by 5 mrad (green), with a dashed line for neutron trajectory. The minimum scattering angle to hit the ZDC is 3.8 mrad and 5.0 mrad in $p+p$ and $p+A$, correspondingly. The differential cross section of elastic and diffractive process suppresses logarithmically as the scattering angle grows, and the minimum angle to hit the ZDC is larger in $p+A$. Therefore, the suppression of such background is expected.

Figure 5.31 shows the exact calculation result, the elastic cross section as a function of scattering angle (left) and the number of elastically scattered proton contribution in the ZDC acceptance as a function of the minimal

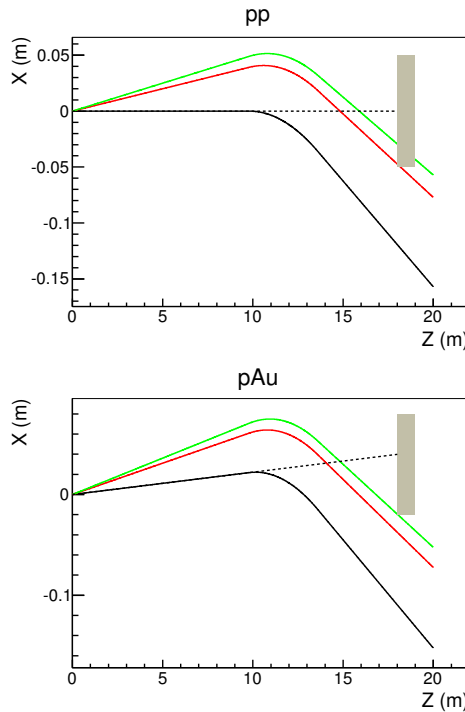


Figure 5.30: Proton trajectory in pp setup (left) and in pA setup (right) for unscattered beam proton (black), elastically scattered by 4 mrad (red), and by 5 mrad (green); dashed line is for neutron trajectory.

scattering angle (right). The cross sections are shown in an arbitrary unit. As can be seen in the right figure, the proton yield in the ZDC acceptance becomes suppressed by an order as the minimal scattering angle increases from 3.8 mrad to 5.0 mrad. This result explains our data. Therefore, the uncertainty of the asymmetric background in $p+A$ is assigned as 2% for all samples conservatively.

Symmetric background

In case of the $p+A$ collisions, an ultra peripheral collision (UPC) is expected to be increasingly important as the atomic mass increases. As to be

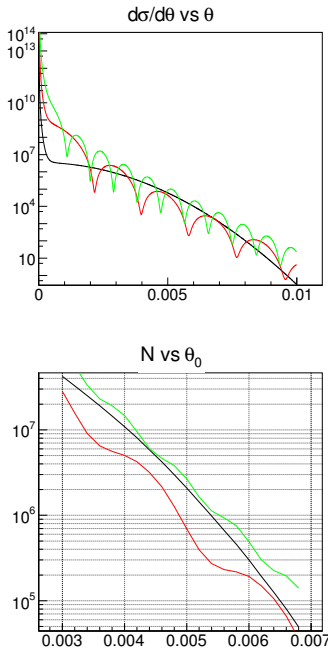


Figure 5.31: (Left) Differential cross section for proton elastic scattering vs scattering angle θ ; (Right) Elastically scattered proton contribution in ZDC acceptance, in arb. units, as a function of the minimal angle θ_0 (see text for explanation); pp (black), pAl (red) and pAu (green).

discussed in details in Sec. 7, the UPC is driven by long distance interaction, where hadronic interactions are suppressed. Therefore, the fraction of the symmetric backgrounds, which are from QCD processes, are expected to be suppressed in $p+A$ compared to $p+p$. Therefore, the uncertainty of the symmetric background fractions are conservatively assigned by 9%, 18%, and 4.5% for the ZDC inclusive, ZDC \otimes BBC-tag, and ZDC \otimes BBC-veto samples, respectively.

As in the simulation study in Sec. 5.2, the background fraction of each data sample is estimated with the x -position.

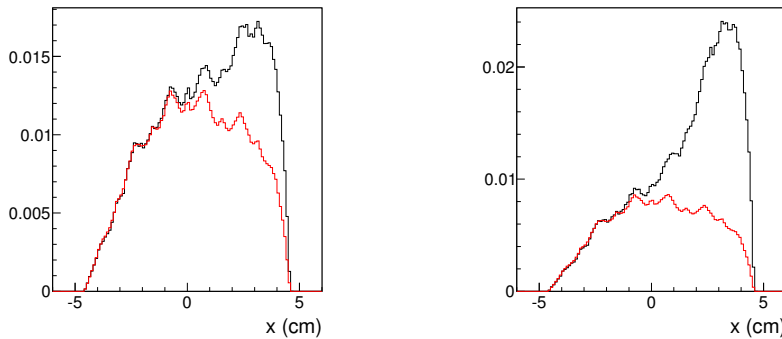


Figure 5.32: Run8 pp: x-distribution of the showers in ZDC reconstructed by SMD in BBC&ZDC sample (red) and ZDC (ZDC&noBBC) sample on the left (right) plot; spectra are normalized to the same value in the range $x < 1$ cm.

5.9.3 Background fraction

5.9.4 “Effective” background fraction

The signal asymmetry is usually calculated as

$$A^S = \frac{A_N^{\text{fit}} - r A^B}{1 - r} \quad (5.8)$$

where r is the background fraction, and A_N^{fit} is the measured asymmetry. However, in case of the signal having the asymmetric detector left-right efficiency/acceptance, like the “asymmetric” background in this analysis, this should be corrected. The correction is studied by simple toy MC by varying the detector left-right asymmetry α_{LR} to get the relation of the “effective” background fraction r_{eff} and the original background fraction r .

All relevant numbers to calculate r_{eff} used for asymmetry correction are summarized in Table 5.3.

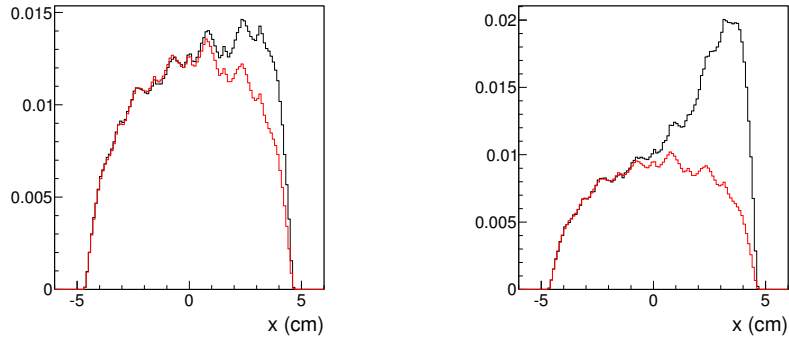


Figure 5.33: Run15 pp: x-distribution of the showers in ZDC reconstructed by SMD in BBC&ZDC sample (red) and ZDC (ZDC&noBBC) sample on the left (right) plot; spectra are normalized to the same value in the range $x < 1$ cm.

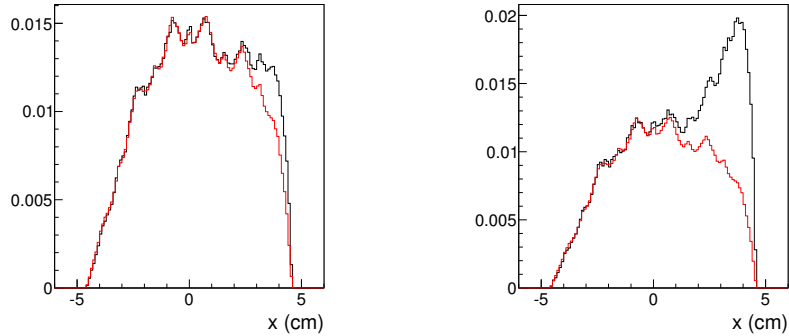


Figure 5.34: Run8 pp: x-distribution of the showers in ZDC reconstructed by SMD in BBC&ZDC sample (red) and ZDC (ZDC&noBBC) sample on the left (right) plot, after charge veto cut is applied; spectra are normalized to the same value in the range $x < 1$ cm.

Table 5.3: Summary of background fraction

| | | Run8, no ch veto | Run8, ch veto | Run15, no ch veto |
|------------------------|---------------|------------------|-------------------|-------------------|
| ZDC inclusive | r | 0.29 ± 0.07 | 0.07 ± 0.05 | 0.16 ± 0.05 |
| | r^{sym} | 0.06 ± 0.03 | 0.02 ± 0.01 | 0.06 ± 0.03 |
| | r^{asym} | 0.23 ± 0.06 | 0.055 ± 0.045 | 0.10 ± 0.045 |
| | α_{LR} | 0.74 | 0.68 | 0.58 |
| | r_{eff} | 0.26 ± 0.06 | 0.07 ± 0.05 | 0.15 ± 0.05 |
| ZDC \otimes BBC-tag | r | 0.12 ± 0.06 | 0.03 ± 0.02 | 0.12 ± 0.06 |
| | r^{sym} | 0.12 ± 0.06 | 0.03 ± 0.02 | 0.12 ± 0.06 |
| | r^{asym} | 0 | 0 | 0 |
| | α_{LR} | 0 | 0 | 0 |
| | r_{eff} | 0.12 ± 0.06 | 0.03 ± 0.02 | 0.12 ± 0.06 |
| ZDC \otimes BBC-veto | r | 0.54 ± 0.07 | 0.26 ± 0.05 | 0.38 ± 0.06 |
| | r^{sym} | 0.03 ± 0.015 | 0.008 ± 0.005 | 0.03 ± 0.015 |
| | r^{asym} | 0.51 ± 0.07 | 0.25 ± 0.05 | 0.35 ± 0.06 |
| | α_{LR} | 0.88 | 0.90 | 0.86 |
| | r_{eff} | 0.41 ± 0.05 | 0.22 ± 0.04 | 0.31 ± 0.05 |

5.9.5 Signal and background asymmetries, A^S and A^B

In order to measure signal asymmetry A^S and background asymmetry A^B , Eq. 5.8 can be modified as

$$A^S = \frac{A_N^{\text{fit}} - r_{\text{eff}} A^B}{1 - r_{\text{eff}}} \quad (5.9)$$

where r_{eff} is the effective background fraction, and A_N^{fit} is the measured asymmetry. Substituting A_N^{fit} and r_{eff} in Eq. 5.9 by measured values of with (“CV”) and without (“No CV”) charge veto cut applied samples in Tab. 5.2 and Tab. 5.3 gives two equations with two unknowns, A^S and A^B .

Tab. 5.4 shows A^S and A^B in Run-08 $p + p$.

| Sample | $A^S \pm \text{stat.}$ | <i>syst.</i> BG | $A^B \pm \text{stat.}$ | <i>syst.</i> BG |
|------------------------|------------------------|----------------------|------------------------|-----------------------|
| ZDC inclusive | -0.0483 \pm 0.0048 | \pm 0.0045 (9.3%) | 0.0141 \pm 0.0182 | \pm 0.0220 (156.2%) |
| ZDC \otimes BBC-tag | -0.0537 \pm 0.0024 | \pm 0.0021 (4.0%) | 0.0108 \pm 0.0230 | \pm 0.0436 (404.7%) |
| ZDC \otimes BBC-veto | -0.0336 \pm 0.0163 | \pm 0.0049 (14.7%) | 0.0140 \pm 0.0300 | \pm 0.0114 (81.6%) |

Table 5.4: A^S and A^B of $p + p$ Run-08.

Tab. 5.5 show A^S in Run-15 $p + p$. A^S from Run-08 and Run-15 show good agreement within statistical uncertainties.

| Sample | Run-15 $A^S \pm \text{stat.}$ | <i>syst.</i> BG |
|------------------------|-------------------------------|----------------------|
| ZDC inclusive | -0.0462 \pm 0.0011 | \pm 0.0059 (12.7%) |
| ZDC \otimes BBC-tag | -0.0548 \pm 0.0016 | \pm 0.0078 (14.2%) |
| ZDC \otimes BBC-veto | -0.0264 \pm 0.0030 | \pm 0.0146 (55.2%) |

Table 5.5: A^S of $p + p$ Run-15, with A^B from Tab. 5.4.

For p+A, background subtraction is not done. We used $A^S = A_N^{\text{fit}}$ and background fractions are assigned as systematic uncertainty.

5.10 Smearing correction

In case of the ideal detector, the measured signal asymmetry A_N^S would be the final asymmetry A_N . However, limited accuracy of realistic detectors smears the asymmetry. This effect is expressed as the smearing correction factor C_{smear} , then the final asymmetry becomes

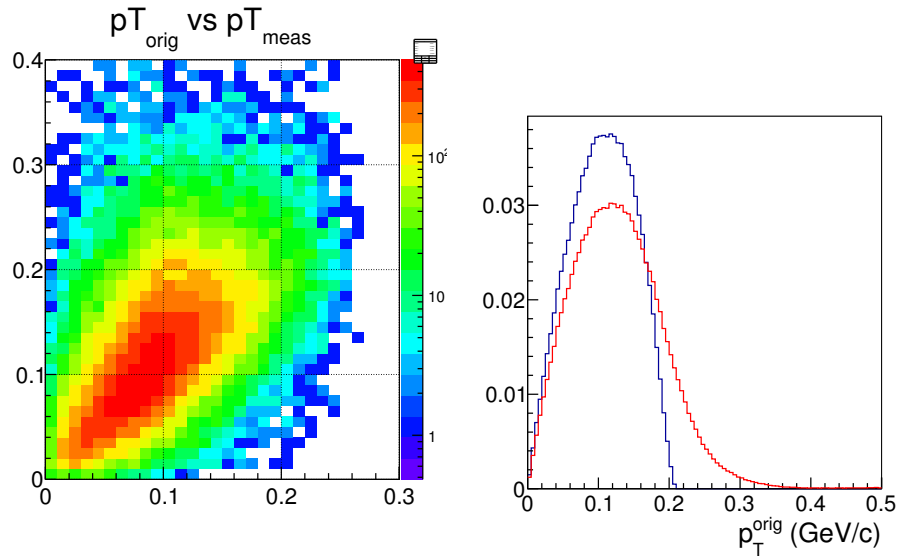
$$A_N = A_N^S / C_{smear}. \quad (5.10)$$

The C_{smear} depends on $d\sigma/dx_F$, $d\sigma/dp_T$, and $A_N(p_T)$ of the neutron production, as well as detector responses, such as energy and position resolutions, edge effects (shower leakage), and noise level. The main difference between the previous analysis [3] is that we investigated the effects of different $A_N(p_T)$ shape, whereas they were assumed to be constant functions in the previous one. In reality, our data showed more consistency with linear $A_N(p_T)$ form, which lead to different C_{smear} .

To study smearing effects, we generated single neutron events with the Monte Carlo simulation tool based on GEANT3, developed for the Run-05 publication [3].^{III} As in the previous publication [3], the $d\sigma/dx_F$ and $d\sigma/dp_T$ were parametrized by the PHENIX and ISR data, respectively.

Figure 5.35a shows the correlation between the original neutron $p_T(p_{Torig})$ value (y -axis), measured $p_T(p_{Tmeas})$ value (x -axis). Due to the shower leakage at the detector edge, the reconstructed centroid of shower can be shifted to the inner side of the detector relative to the actual one. This effect explains the overall smaller p_{Tmeas} values than p_{Torg} values, however, they still show

^{III}The reliability of this simulation for the ZDC was tested for the prototype ZDC and current PHENIX ZDC. This simulation well reproduced the energy response and resolution of the prototype ZDC for the various incident neutron positions with 100 GeV proton beam, and those of the PHENIX ZDC for 100 GeV peripheral neutrons from heavy ion collisions [3].



(a) Correlation between true p_T (b) Original p_T distribution (blue) (p_T^{orig}) and measured one (p_T^{meas}). and measured p_T distribution (red).

Figure 5.35: Comparison between original (true) p_T of neutron and measured (reconstructed) p_T .

a clear correlation.

The blue histogram in Fig. 5.35b displays the original p_T distribution of neutrons, which we want to measure. The maximum value 0.22 GeV/c corresponds to the maximum cutoff of our kinematic cuts, $p_T \sim E_n \theta = 100 \text{ GeV} \cdot 2.2 \text{ mrad} = 0.22 \text{ GeV}/c$. If we measure the reconstructed p_T values of neutrons with an ideal detector, we will obtain such distribution. However, due to the reason explained in the previous paragraph, the data sample what we collected by the analysis cuts contains some fraction of neutrons of which original p_T values are outside of what we intended to measure. As a result, the original p_T distribution of what we actually sampled follows the red histogram. To clarify, let's define the neutron sample of the former (blue histogram) as a set $O = \{\text{neutron} \mid \text{original sample}\}$, and the latter (red histogram) as a set $M = \{\text{neutron} \mid \text{measured sample}\}$.

Due to the uncertainty of left-right position, the measured asymmetry

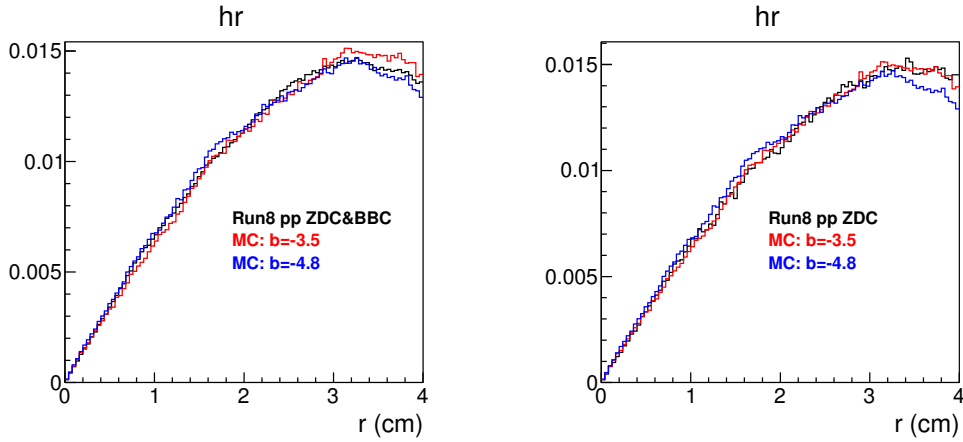


Figure 5.36: Run-08 ZDC \otimes BBC-tag (left) and (right) r distribution of data (black) and simulation with exponential p_T slope parameter $b = -3.5 \text{ (GeV}/c\text{)}^{-1}$ (red) and $b = -4.8 \text{ (GeV}/c\text{)}^{-1}$ (blue).

(A_N^S) of a given sample is smeared from the original one (A_N). This smearing mostly comes from around the low p_T area, where the left-right uncertainty is relatively large. Then the measured asymmetry is $A_N^S(M)$.

It is natural to calculate the smearing correction factor as $C_{smear}^{ideal} = A_N(O)/A_N^S(M)$. However, this value was sensitive to different assumptions particularly the assumption of the $A_N(p_T)$ form, then made the final A_N to be end up with a large uncertainty. On the other hand, $C_{smear}^{actual} = A_N(M)/A_N^S(M)$ showed much weaker dependence on different assumptions. Therefore, we adopted C_{smear}^{actual} as the correction factor.

5.10.1 $d\sigma/dp_T$ shape dependence

In the previous publication [3], the p_T distribution showed a good agreement with the ISR measurement, following $d\sigma/dp_T \sim \exp(b \cdot p_T)$ form with $b = -4.8 \text{ (GeV}/c\text{)}^{-1}$. Since neutron production mechanisms in different collision systems and BBC taggings may different, p_T distribution of each sample can be varied. The reliability of the p_T distribution of simulation input was

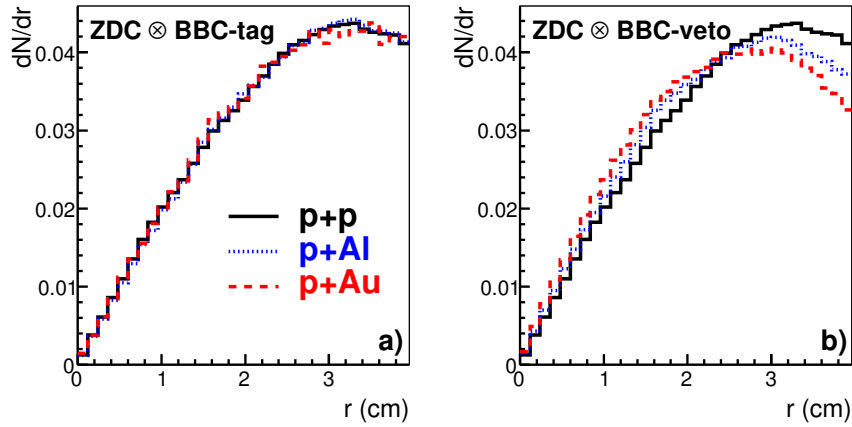


Figure 5.37: r distribution of neutron data samples of $ZDC \otimes BBC\text{-tag}$ (left) and $ZDC \otimes BBC\text{-veto}$ (right) of three collision systems.

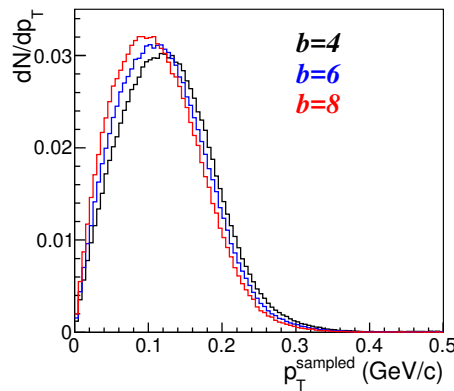


Figure 5.38: p_T distribution of neutron sample with simulation with different exponential p_T slope parameter b

tested by comparing r ($p_T = E_n r/d$) distribution with data. $r = \sqrt{x^2 + y^2}$ was defined by the shower x and y positions measured by SMD.

Figure 5.36 shows r distribution of Run-08 $p+p$. Our $p+p$ data also shows the same level of consistency as in [3] with exponential slope parameter $b = -4.8$ $(\text{GeV}/c)^{-1}$ in the simulation. However, showed better consistency with $b = -4.0$ and -3.5 $(\text{GeV}/c)^{-1}$ for $ZDC \otimes BBC\text{-tag}$ and $ZDC \otimes BBC\text{-veto}$.

veto, respectively. The flattening in ZDC \otimes BBC-veto may due to the residual proton background in ZDC inclusive, which shows peak at the right.

Figure 5.37 shows r distribution of all collision systems of different BBC taggings. ZDC \otimes BBC-tag samples of three collision systems follow similar r distributions, and best consistency with $b = -4.0$ $(\text{GeV}/c)^{-1}$. On the other hand, r distribution of ZDC \otimes BBC-veto samples varies in different collision systems, showing best consistency with $b = -4, 6, \text{and} 8$ $(\text{GeV}/c)^{-1}$ for $p+p$, $p+\text{Al}$, and $p+\text{Au}$, respectively. $b = \pm 1$ $(\text{GeV}/c)^{-1}$ uncertainty comes from SMD gain calibration and threshold.

Figure 5.38 shows p_T distribution with different p_T slope parameter. The uncertainty of slope parameter varies average p_T value up to 10%. While $C_{\text{smear}}^{\text{ideal}}$ varied by 5% when the slope parameter varied -3.5 to -8 $(\text{GeV}/c)^{-1}$, $C_{\text{smear}}^{\text{actual}}$ was stable within 0.5%.

5.10.2 $d\sigma/dx_F$ shape dependence

The x_F distribution of forward neutron at $p_T < 0.1$ GeV/c . was measured at PHENIX [3]. The result showed a good consistency with the ISR measurement. However, our data covers higher $p_T < 0.2$ GeV/c , and ISR data at $p_T \sim 0.2 \text{GeV}/c$ in Fig. 3.1 shows flatter distribution. Therefore, we compared C_{smear} for two extreme cases, one is for x_F distribution in [3], and the other for flat x_F distribution. The $C_{\text{smear}}^{\text{ideal}}$ was differ by 3%, and $C_{\text{smear}}^{\text{actual}}$ was stable within 0.5%.

5.10.3 SMD threshold dependence

The simulation tool in the previous section required the tuning for different Run-15 operational condition. The SMD threshold and resolution could be changed, therefore, compared with data. The SMD threshold was tuned based on the number of fired SMD distributions in the data. Figure 5.39 shows such

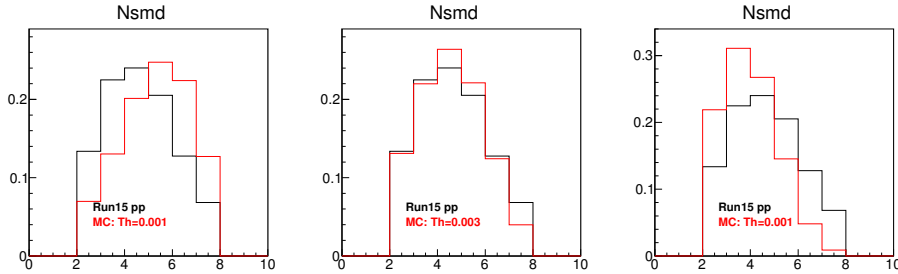


Figure 5.39: Distribution of the number of fired SMD hits in x-direction: Run15 pp data (black) vs MC (red) with SMD energy threshold 1 MeV (left), 3 MeV (middle), and 6 MeV (right).

distributions of three different threshold energy. 3 MeV threshold energy gave the best agreement between the data (black) and simulation (red), therefore, the simulation was tuned at this value. When the threshold is lower or higher, the distribution peak is shifted. The uncertainty from varying threshold was $\sim 3\%$ for both C_{smear}^{ideal} and C_{smear}^{actual} .

5.10.4 Position resolution

The position resolution affects the C_{smear} value. As studied in [3], the resolution was not only determined by the innate properties of the scintillator materials, but also affected by cross talk between SMD channels. The noise level was tested by comparing [maximum charge]/[total charge] distribution (E_{max}/E_{tot}) of SMD. Figure 5.40 left shows comparison between data (black) and simulation (red) with zero cross talk. The distribution shows inconsistency. When we introduce 10% of charge sharing to neighboring two channels (Figure 5.40 right), they shows consistency. The difference between zero and 10% of cross talk effect makes 2% and 1% of variation for C_{smear}^{ideal} and C_{smear}^{actual} , respectively.

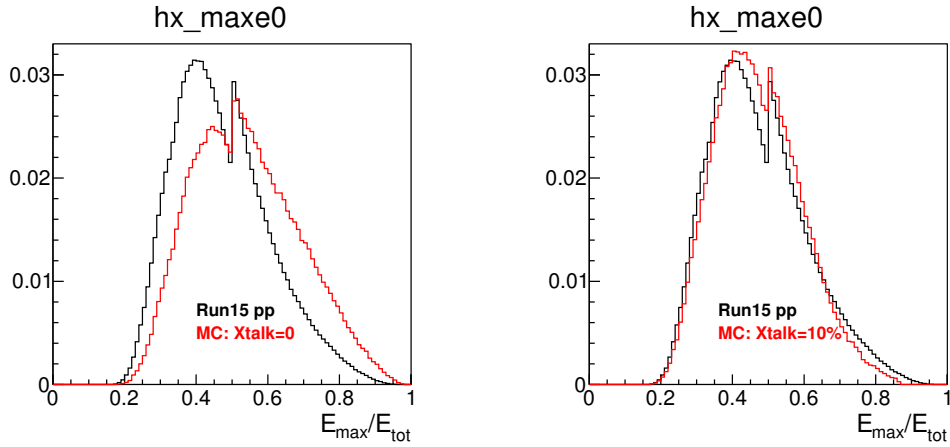


Figure 5.40: Distribution for the energy fraction in the maximal energy strip: Run15 pp data (black) vs MC (red) assuming no cross talk (left) and 10% cross talk (right).

5.10.5 $A_N(p_T)$ shape dependence

In the Run-05 analysis [3], $A_N(p_T) = \text{const}$ was assumed. However, our data shows better consistency with approximately linear function form, as can be seen later in this section. Linear form is also supported by the current theory [7]. Therefore, we studied various assumption of $A_N(p_T)$ form and their impact on C_{smear} .

We tested two input forms, one is $A_N(p_T) \sim p_T^\alpha$, where $\alpha=1$ corresponds to a linear behavior $A_N(p_T) \sim p_T$ and $\alpha=0$ corresponds to $A_N(p_T) = \text{const}$ (Fig 5.41 left), and the other is step-function function form (Fig 5.41 right). Figure 5.42 shows their measured asymmetry values, which accounts for detector smearing effects. The curves are normalized by the same averaged asymmetry value.

Figure 5.43 shows $C_{\text{smear}}^{\text{ideal}}$ (blue) and $C_{\text{smear}}^{\text{actual}}$ (red) as a function of α (left) and p_{T0} (right), respectively. While $C_{\text{smear}}^{\text{ideal}}$ varies between 0.8 and 1.4 depending on assumed $A_N(p_T)$ form, $C_{\text{smear}}^{\text{actual}}$ varied moderately.

From Fig. 5.44 to Fig. 5.49 show comparison with data. ZDC \otimes BBC-tag

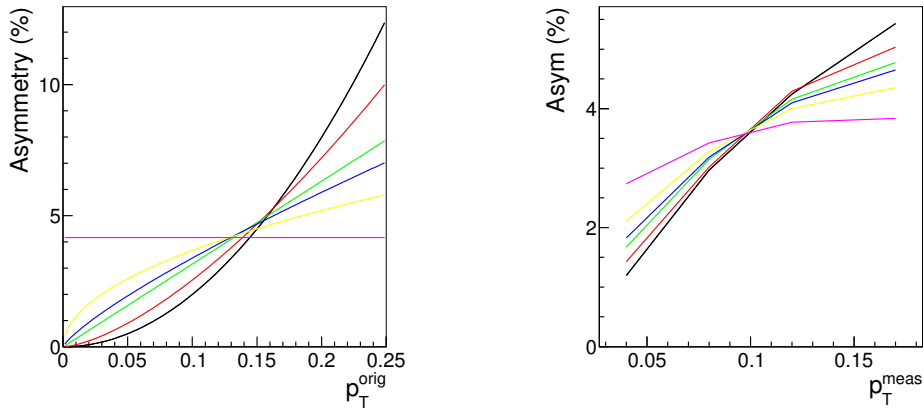


Figure 5.41: Input asymmetries. Left: parametrized as $A_N(p_T) \sim p_T^\alpha$ with $\alpha = 0$ (magenta), 0.5 (yellow), 0.8 (blue), 1.0 (green), 1.5 (red) and 2.0 (black). Right: threshold value $p_{T0} = 0.15$ (magenta), 0.12 (yellow), 0.10 (blue), 0.07 (green), 0.05 (red) and 0 (black).

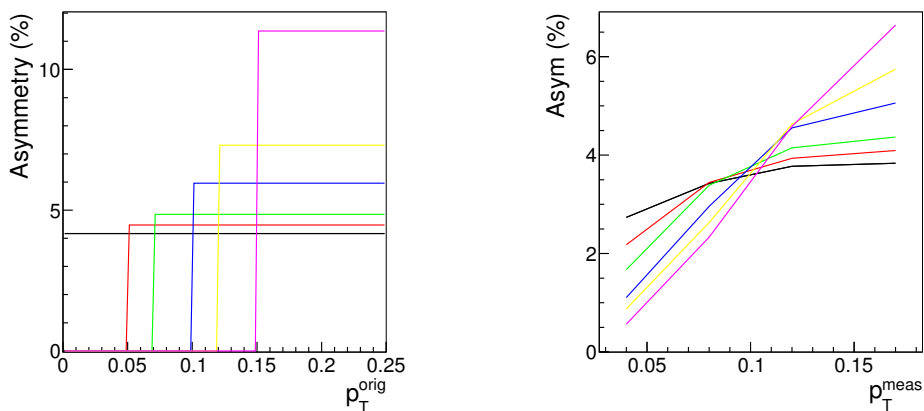


Figure 5.42: Measured asymmetries obtained from simulation.

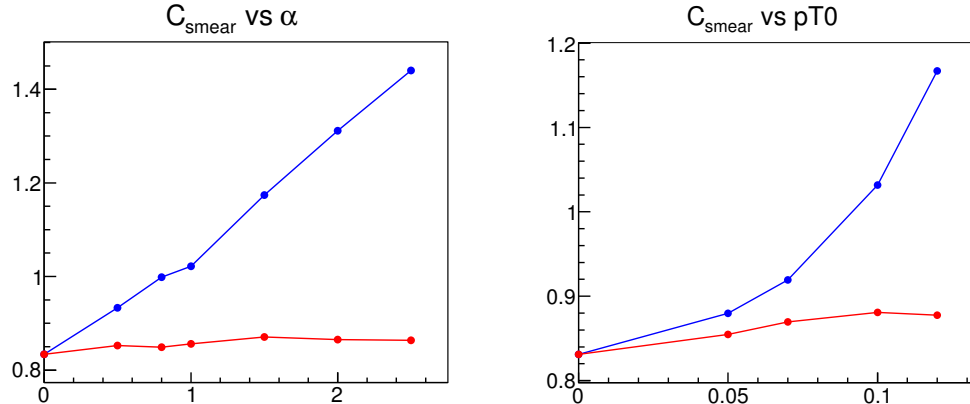


Figure 5.43: Smearing correction, $C_{\text{smear}}^{\text{ideal}}$ (blue) and $C_{\text{smear}}^{\text{actual}}$ (red) vs slope parameter α in the parameterization $A_N(p_T) \sim p_T^\alpha$ (left), and threshold parameter p_{T0} (right).

in $p+A$ and ZDC \otimes BBC-veto in $p+p$ are not shown since their statistical uncertainties are relatively large compare to their asymmetry values, therefore, data couldn't distinguish best $A_N(p_T)$ function form.

Table 5.6: $C_{\text{smear}}^{\text{ideal}} / C_{\text{smear}}^{\text{actual}}$ correction and uncertainties assuming $A_N(p_T) \sim p_T^\alpha$.

| | pp | pAl | pAu |
|------------------------|-----------------------------------|-----------------------------------|-----------------------------------|
| ZDC inclusive | $0.90 \pm 0.07 / 0.843 \pm 0.010$ | $1.25 \pm 0.35 / 0.852 \pm 0.006$ | $1.19 \pm 0.05 / 0.865 \pm 0.002$ |
| ZDC \otimes BBC-tag | $0.96 \pm 0.06 / 0.851 \pm 0.005$ | $1.25 \pm 0.35 / 0.852 \pm 0.006$ | $1.07 \pm 0.17 / 0.856 \pm 0.010$ |
| ZDC \otimes BBC-veto | $0.90 \pm 0.07 / 0.843 \pm 0.010$ | $1.48 \pm 0.13 / 0.862 \pm 0.005$ | $1.19 \pm 0.05 / 0.865 \pm 0.002$ |

The results obtained from fits are summarized in Table 5.7.

Table 5.7: $C_{\text{smear}}^{\text{ideal}} / C_{\text{smear}}^{\text{actual}}$ correction and uncertainties assuming $A_N(p_T) = \text{const}$ for $p_T > p_{T0}$ and 0 for $p_T < p_{T0}$.

| | pp | pAl | pAu |
|------------------------|-----------------------------------|-----------------------------------|-----------------------------------|
| ZDC inclusive | $0.89 \pm 0.06 / 0.85 \pm 0.02$ | $1.09 \pm 0.21 / 0.87 \pm 0.01$ | $1.01 \pm 0.03 / 0.875 \pm 0.002$ |
| ZDC \otimes BBC-tag | $0.90 \pm 0.02 / 0.865 \pm 0.005$ | $1.09 \pm 0.21 / 0.87 \pm 0.01$ | $0.96 \pm 0.08 / 0.87 \pm 0.01$ |
| ZDC \otimes BBC-veto | $0.89 \pm 0.06 / 0.85 \pm 0.02$ | $1.18 \pm 0.12 / 0.880 \pm 0.002$ | $1.01 \pm 0.03 / 0.875 \pm 0.002$ |

The results in Table 5.7 are systematically lower than in Table 5.6, particularly for pA data. This difference will be assigned as an additional syst. uncertainty for C_{smear} correction.

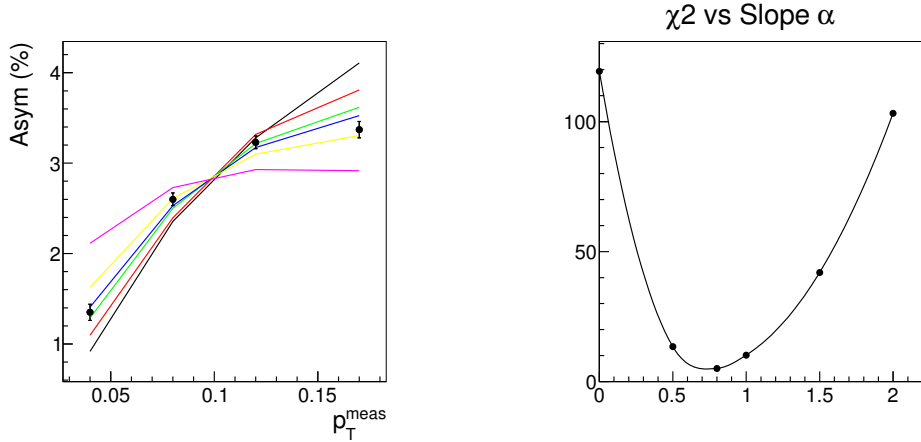


Figure 5.44: Left: asymmetry vs p_T^{meas} , data (black) vs MC calculation with different α in parameterization $A_N(p_T) \sim p_T^\alpha$: $\alpha = 0$ (magenta), 0.5 (yellow), 0.8 (blue), 1.0 (green), 1.5 (red) and 2.0 (black); MC curves are normalized to get the same average asymmetry as in data; data are Run 15 pp ZDC \otimes -BBC-tag triggered sample. Right: χ^2 vs α .

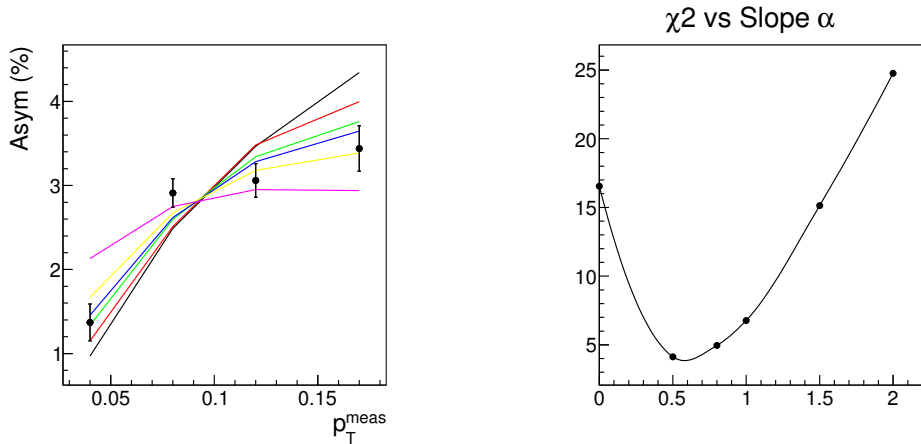


Figure 5.45: Left: asymmetry vs p_T^{meas} , data (black) vs MC calculation with different α in parameterization $A_N(p_T) \sim p_T^\alpha$: $\alpha = 0$ (magenta), 0.5 (yellow), 0.8 (blue), 1.0 (green), 1.5 (red) and 2.0 (black); MC curves are normalized to get the same average asymmetry as in data; data are Run 8 pp ZDC \otimes -BBC-tag triggered sample. Right: χ^2 vs α .

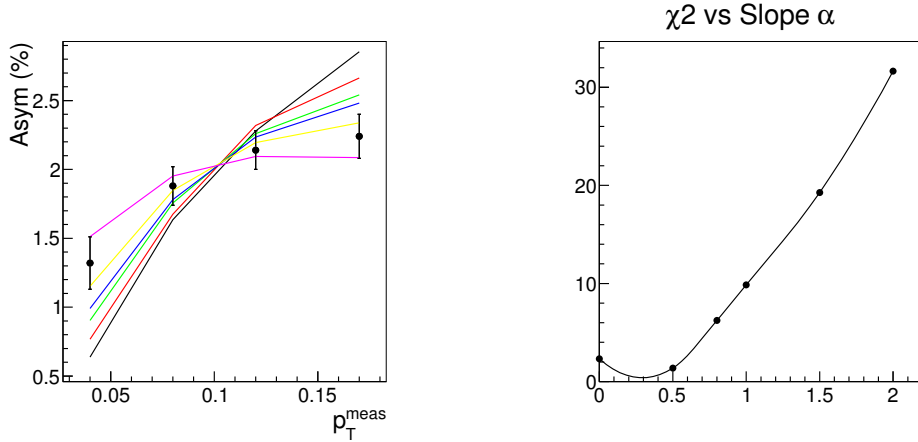


Figure 5.46: Left: asymmetry vs p_T^{meas} , data (black) vs MC calculation with different α in parameterization $A_N(p_T) \sim p_T^\alpha$: $\alpha = 0$ (magenta), 0.5 (yellow), 0.8 (blue), 1.0 (green), 1.5 (red) and 2.0 (black); MC curves are normalized to get the same average asymmetry as in data; data are Run 15 pp ZDC triggered sample. Right: χ^2 vs α .

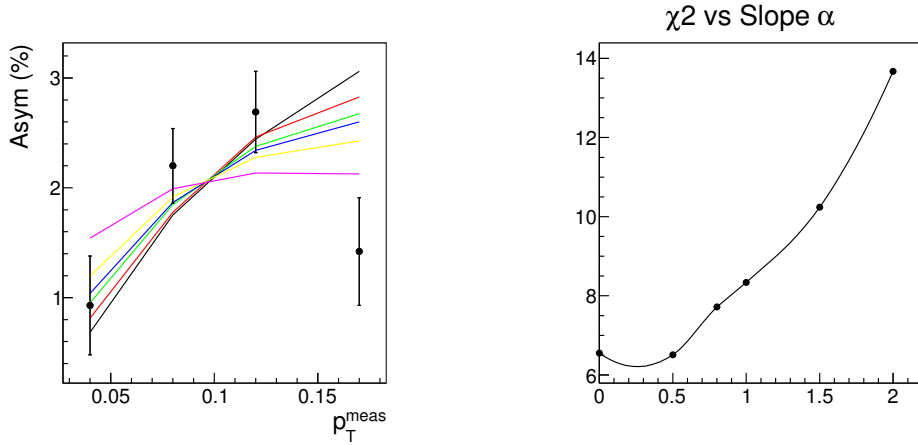


Figure 5.47: Left: asymmetry vs p_T^{meas} , data (black) vs MC calculation with different α in parameterization $A_N(p_T) \sim p_T^\alpha$: $\alpha = 0$ (magenta), 0.5 (yellow), 0.8 (blue), 1.0 (green), 1.5 (red) and 2.0 (black); MC curves are normalized to get the same average asymmetry as in data; data are Run 8 pp ZDC triggered sample. Right: χ^2 vs α .

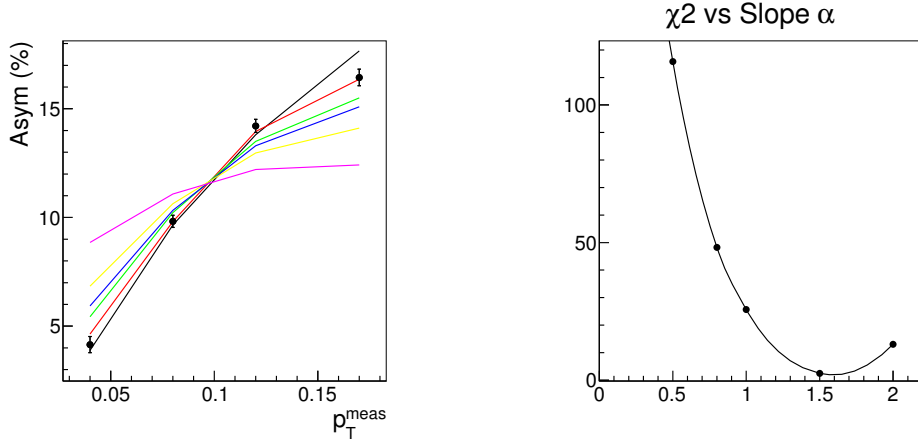


Figure 5.48: Left: asymmetry vs p_T^{meas} , data (black) vs MC calculation with different α in parameterization $A_N(p_T) \sim p_T^\alpha$: $\alpha = 0$ (magenta), 0.5 (yellow), 0.8 (blue), 1.0 (green), 1.5 (red) and 2.0 (black); MC curves are normalized to get the same average asymmetry as in data; data are Run 15 pAu ZDC- \otimes BBC-veto triggered sample. Right: χ^2 vs α .

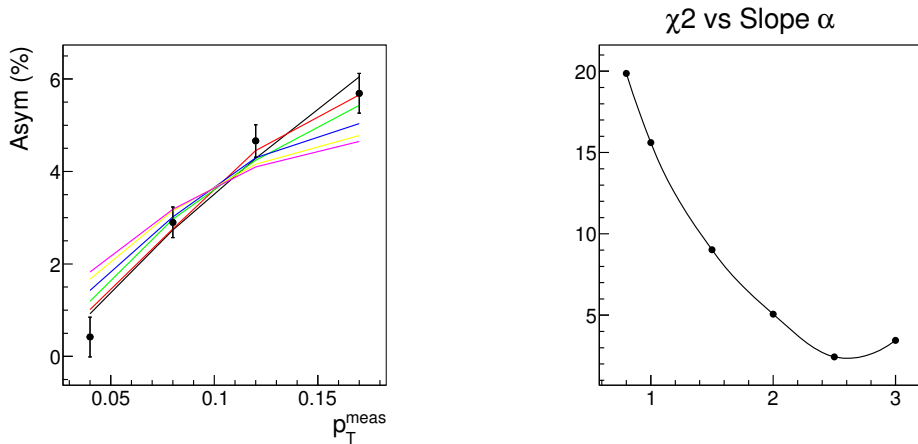


Figure 5.49: Left: asymmetry vs p_T^{meas} , data (black) vs MC calculation with different α in parameterization $A_N(p_T) \sim p_T^\alpha$: $\alpha = 0.8$ (magenta), 1.0 (yellow), 1.5 (blue), 2.0 (green), 2.5 (red) and 3.0 (black); note, the range of α here is different from all previous plots; MC curves are normalized to get the same average asymmetry as in data; data are Run 15 pAl ZDC \otimes BBC-veto triggered sample. Right: χ^2 vs α .

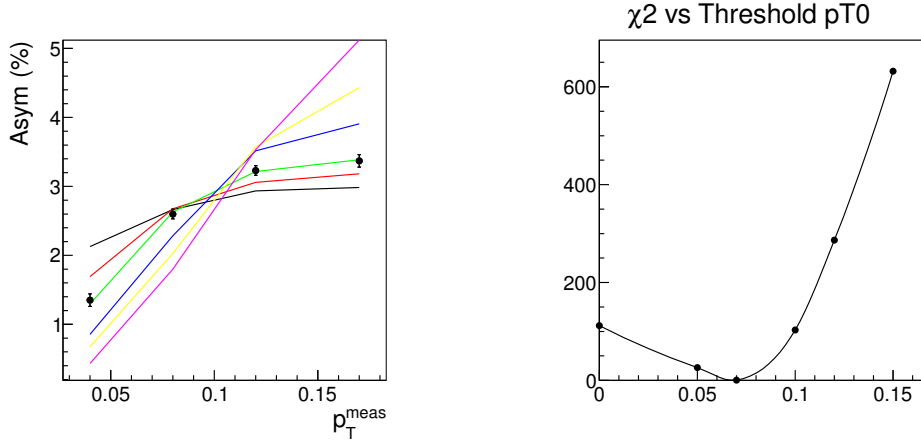


Figure 5.50: Left: asymmetry vs p_T^{meas} , data (black) vs MC calculation with different threshold value p_{T0} in representation of $A_N(p_T)$ as a step-function: $p_{T0} = 0.15$ (magenta), 0.12 (yellow), 0.10 (blue), 0.07 (green), 0.05 (red) and 0 (black); MC curves are normalized to get the same average asymmetry as in data; data are Run 15 pp ZDC \otimes BBC-tag triggered sample. Right: χ^2 vs p_{T0} .

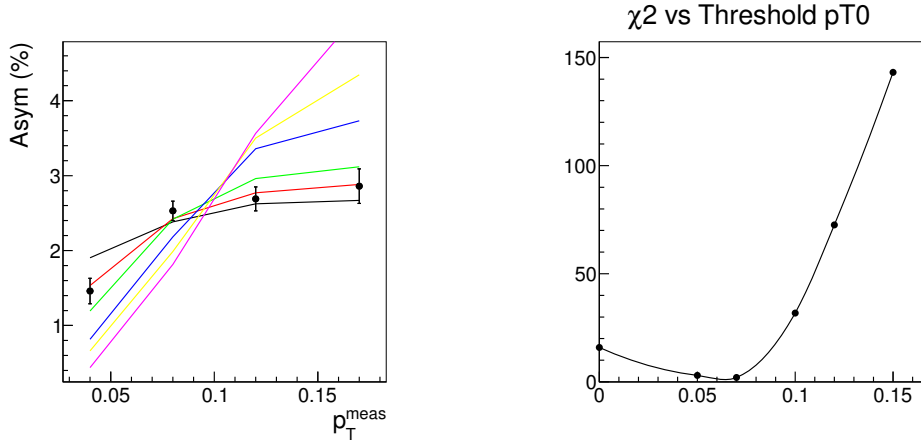


Figure 5.51: Left: asymmetry vs p_T^{meas} , data (black) vs MC calculation with different threshold value p_{T0} in representation of $A_N(p_T)$ as a step-function: $p_{T0} = 0.15$ (magenta), 0.12 (yellow), 0.10 (blue), 0.07 (green), 0.05 (red) and 0 (black); MC curves are normalized to get the same average asymmetry as in data; data are Run 8 pp ZDC \otimes BBC-tag triggered sample. Right: χ^2 vs p_{T0} .

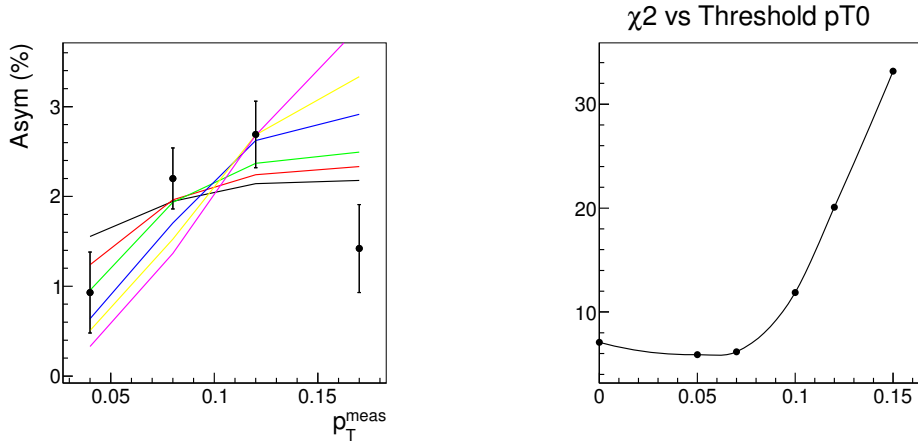


Figure 5.52: Left: asymmetry vs p_T^{meas} , data (black) vs MC calculation with different threshold value p_{T0} in representation of $A_N(p_T)$ as a step-function: $p_{T0} = 0.15$ (magenta), 0.12 (yellow), 0.10 (blue), 0.07 (green), 0.05 (red) and 0 (black); MC curves are normalized to get the same average asymmetry as in data; data are Run 8 pp ZDC triggered sample. Right: χ^2 vs p_{T0} .

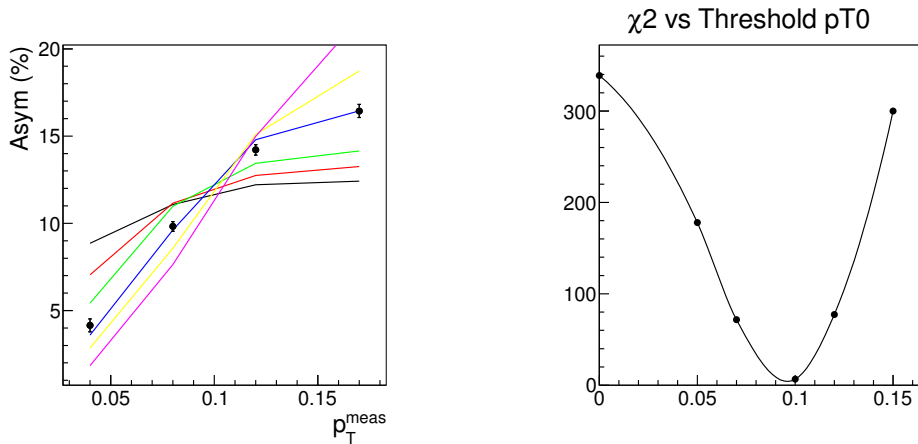


Figure 5.53: Left: asymmetry vs p_T^{meas} , data (black) vs MC calculation with different threshold value p_{T0} in representation of $A_N(p_T)$ as a step-function: $p_{T0} = 0.15$ (magenta), 0.12 (yellow), 0.10 (blue), 0.07 (green), 0.05 (red) and 0 (black); MC curves are normalized to get the same average asymmetry as in data; data are Run 15 pAu ZDC \otimes BBC-veto triggered sample. Right: χ^2 vs p_{T0} .

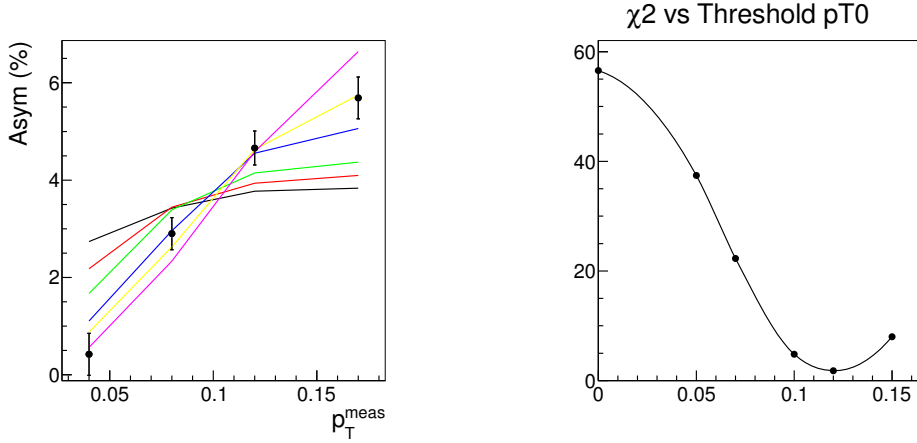


Figure 5.54: Left: asymmetry vs p_T^{meas} , data (black) vs MC calculation with different threshold value p_{T0} in representation of $A_N(p_T)$ as a step-function: $p_{T0} = 0.15$ (magenta), 0.12 (yellow), 0.10 (blue), 0.07 (green), 0.05 (red) and 0 (black); MC curves are normalized to get the same average asymmetry as in data; data are Run 15 pAl ZDC \otimes BBC-veto triggered sample. Right: χ^2 vs p_{T0} .

5.10.6 Final C_{smear} and its uncertainty

From results in Table 5.6 and Table 5.7 one can derive a few important conclusions: (1) C_{smear}^{ideal} is very sensitive to different $A_N(p_T)$ shape; (2) C_{smear}^{ideal} is very sensitive to assumption for $A_N(p_T)$ shape parametrization; (3) C_{smear}^{actual} value is very stable.

From the conclusions above, and trying to avoid any explicit derivation of $A_N(p_T)$ for different data samples, we can safely follow the approach with C_{smear}^{actual} , which only weakly depends on different assumptions for $A_N(p_T)$ shape, and hence use one common value for smearing correction with uncertainties covering the whole possible range of its variation for different collision systems and triggers, therefore, $C_{smear}^{actual} = 0.855 \pm 0.025$. The other systematic uncertainty to be included is 3% due to SMD threshold (which affects the position resolution). All others are negligible. So, summarizing, $C_{smear}^{actual} = 0.855 \pm 0.036(4.2\%)$.

5.10.7 Final asymmetry A_N

Final asymmetry A_N is calculated as follows.

$$A_N = \frac{A^S}{C_{smear}^{actual}} \quad (5.11)$$

The table shows the final asymmetries with statistical uncertainties.

| Data | A_N^n | $A_N^{n\&BBC}$ tagged | $A_N^{n\&BBC}$ vetoed |
|----------|----------------------|-----------------------|-----------------------|
| $p + p$ | -0.0540 ± 0.0012 | -0.0641 ± 0.0019 | -0.0309 ± 0.0035 |
| $p + Al$ | -0.0126 ± 0.0015 | -0.0566 ± 0.0026 | 0.0727 ± 0.0027 |
| $p + Au$ | 0.1574 ± 0.0019 | -0.0150 ± 0.0053 | 0.2342 ± 0.0024 |

Table 5.8: Forward neutron A_N values and statistical uncertainties in polarized proton-nucleus collisions.

5.11 Systematic uncertainties

5.11.1 Background

For $p + p$, background asymmetries are subtracted, and their systematic uncertainties are calculated by error propagation as Eq. A.23. For $p+A$, hard scattering background fraction of $p+p$ are assigned for the one side systematic uncertainties conservatively, 9%, 4.5%, 18% for ZDC inclusive, “ZDC \otimes BBC-veto”, and “ZDC \otimes BBC-tag” samples. Plus, 2% uncertainty from elastic background is assigned one side by quadratic sum for the ZDC inclusive and “ZDC \otimes BBC-veto” samples. Table 5.9 shows the result.

| Data set | sample | <i>syst.</i> |
|----------|------------------------|----------------------|
| p+p | ZDC Inclusive | ± 0.0069 (12.7%) |
| p+Au | ZDC Inclusive | -0.0145 (9.2%) |
| p+Al | ZDC Inclusive | +0.0012 (9.2%) |
| p+p | ZDC \otimes BBC-tag | ± 0.0091 (14.2%) |
| p+Au | ZDC \otimes BBC-tag | +0.0027 (18.0%) |
| p+Al | ZDC \otimes BBC-tag | +0.0102 (18.0%) |
| p+p | ZDC \otimes BBC-veto | ± 0.0170 (55.2%) |
| p+Au | ZDC \otimes BBC-veto | -0.0115 (4.9%) |
| p+Al | ZDC \otimes BBC-veto | -0.0036 (4.9%) |

Table 5.9: Systematic uncertainties from background.

5.11.2 Smearing

4.2% of uncertainty from C_{smear}^{actual} is assigned for all samples as shown in Tab. 5.11.2.

| Data set | BBC coincidence | <i>syst.</i> |
|----------|------------------------|---------------------|
| p+p | ZDC inclusive | ± 0.0023 (4.2%) |
| p+Au | ZDC inclusive | ± 0.0066 (4.2%) |
| p+Al | ZDC inclusive | ± 0.0005 (4.2%) |
| p+p | ZDC \otimes BBC-tag | ± 0.0027 (4.2%) |
| p+Au | ZDC \otimes BBC-tag | ± 0.0006 (4.2%) |
| p+Al | ZDC \otimes BBC-tag | ± 0.0024 (4.2%) |
| p+p | ZDC \otimes BBC-veto | ± 0.0013 (4.2%) |
| p+Au | ZDC \otimes BBC-veto | ± 0.0099 (4.2%) |
| p+Al | ZDC \otimes BBC-veto | ± 0.0031 (4.2%) |

Table 5.10: Systematic uncertainties from smearing correction.

5.11.3 Polarization

The systematic uncertainty from polarization for each data point is assigned from the statistical uncertainty of each measurement (see Tab. 5.2). Uncertainties are shown in Tab. 5.11. As the intrinsic systematic of the carbon target polarimeter, the polarization normalization uncertainty, is assigned as 3.4% of global uncertainty.

| Data set | BBC coincidence | <i>syst.</i> |
|----------|------------------------|---------------------|
| p+p | ZDC inclusive | ± 0.0004 (0.7%) |
| p+Au | ZDC inclusive | ± 0.0112 (7.1%) |
| p+Al | ZDC inclusive | ± 0.0005 (4.0%) |
| p+p | ZDC \otimes BBC-tag | ± 0.0005 (0.7%) |
| p+Au | ZDC \otimes BBC-tag | ± 0.0012 (7.7%) |
| p+Al | ZDC \otimes BBC-tag | ± 0.0022 (3.9%) |
| p+p | ZDC \otimes BBC-veto | ± 0.0007 (2.4%) |
| p+Au | ZDC \otimes BBC-veto | ± 0.0168 (7.2%) |
| p+Al | ZDC \otimes BBC-veto | ± 0.0028 (3.8%) |

Table 5.11: Systematic uncertainties from polarization.

5.11.4 Beam position

The uncertainty from the beam center ambiguity is estimated by varying the assumed beam center position ± 10 mm in x and ± 5 mm in y direction. The position survey results give a few mm deviation between the zero degree line and the ZDC center. However, for the x -direction, we assigned conservative uncertainty as 10 mm of deviation because 1 cm difference explains the different asymmetric background fraction between Run8 and Run15.

Fig. 5.55 to Fig. 5.58 show A_N^{fit} of each beam center position. The maxi-

mum difference between the asymmetry at $(0,0)$ and that of another position is assigned as the uncertainty. The values are summarized in Tab. 5.12.

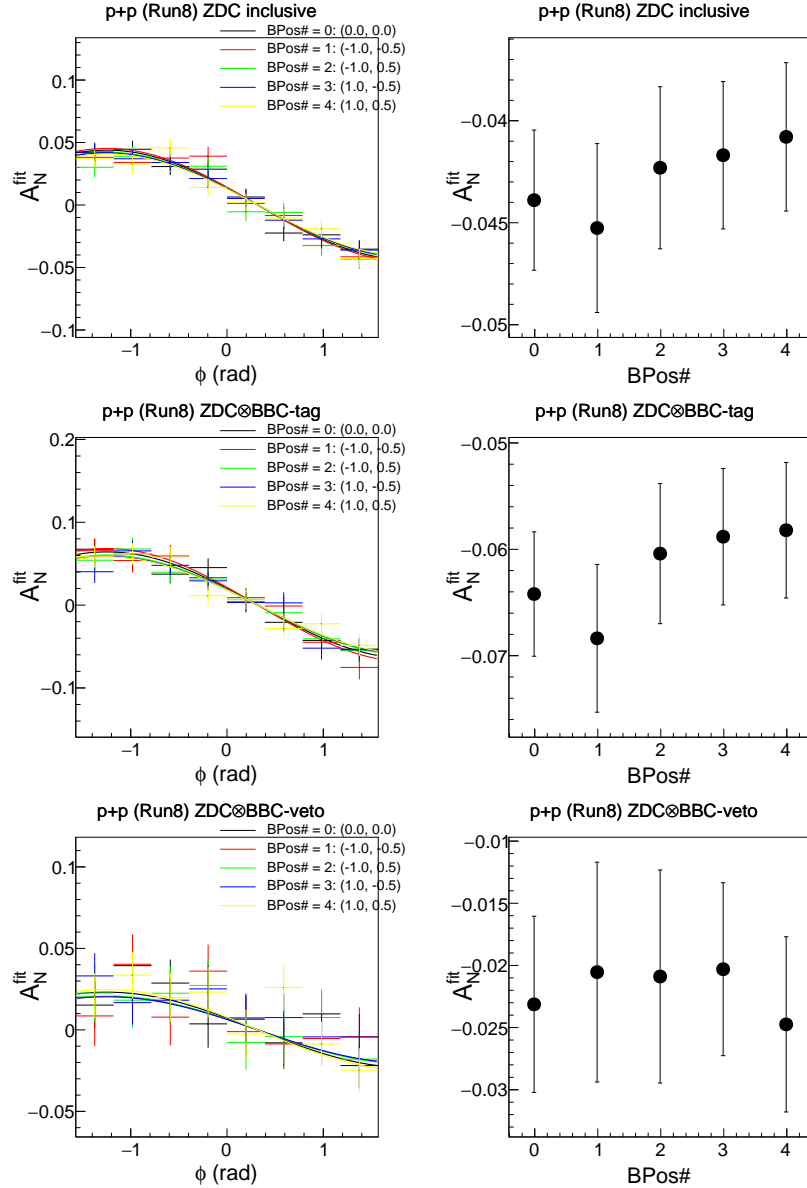
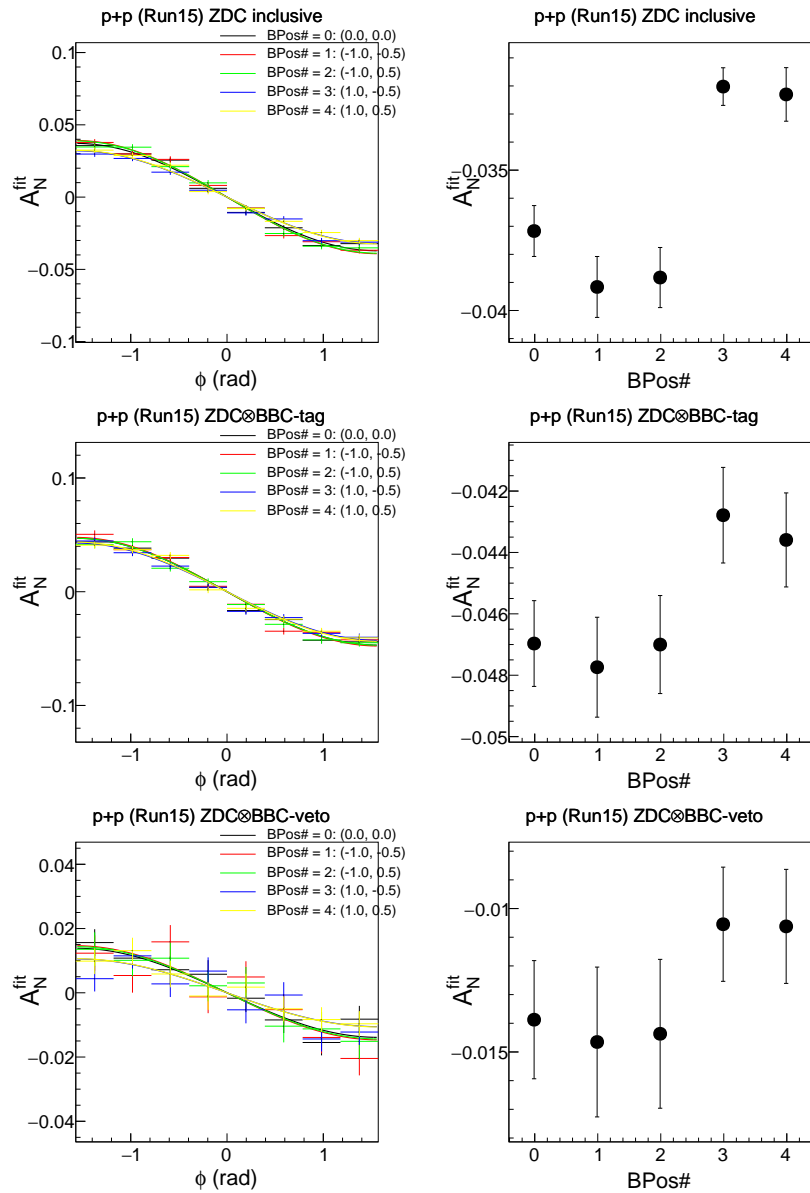
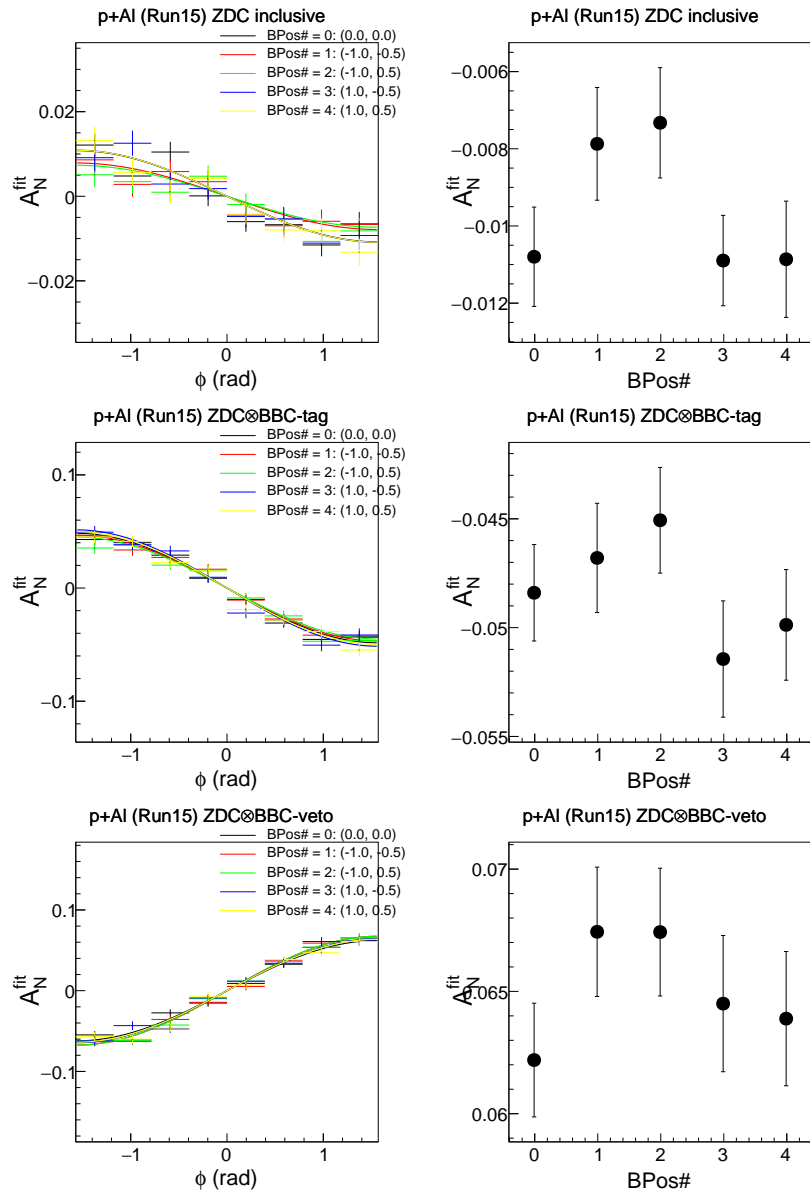
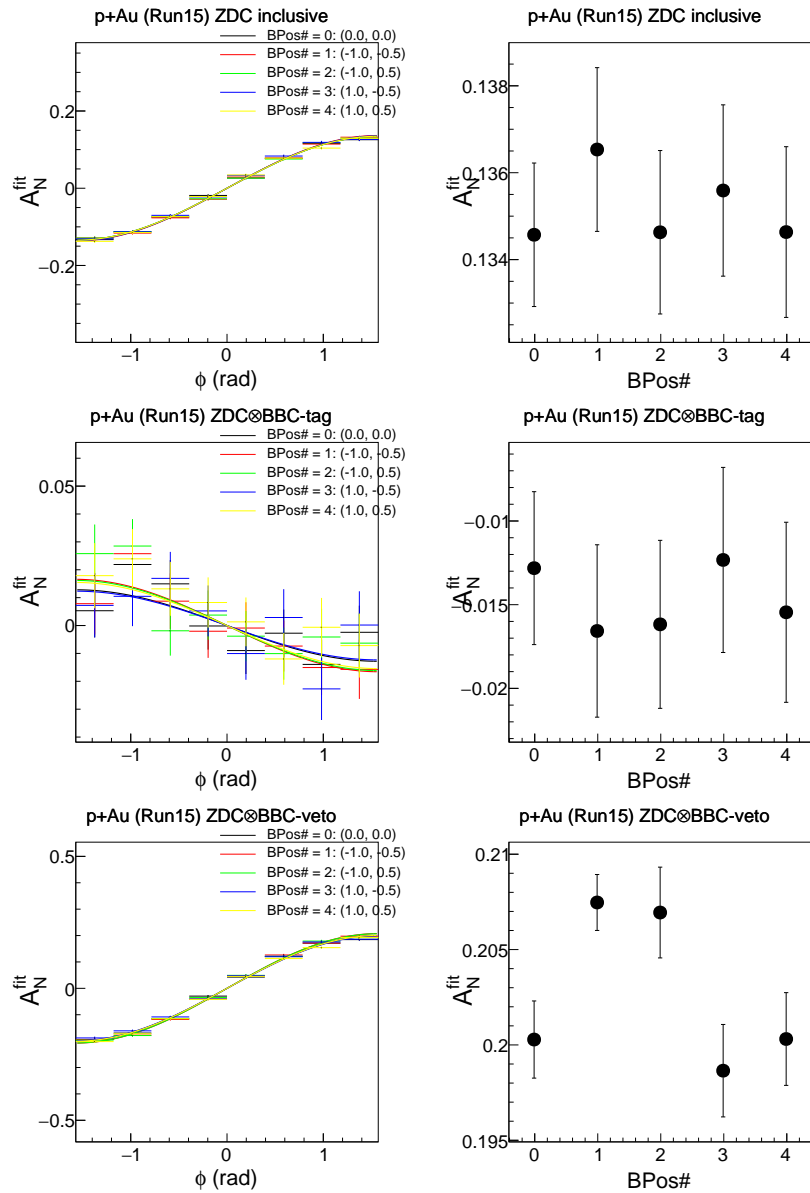


Figure 5.55: Beam position scan for Run-08 $p + p$.

Figure 5.56: Beam position scan for Run-15 $p + p$.

Figure 5.57: Beam position scan for Run-15 $p+Al$.

Figure 5.58: Beam position scan for Run-15 $p+Au$.

| Run | BBC coincidence | <i>syst.</i> |
|--------------|------------------------|----------------------|
| p+p (Run8) | ZDC inclusive | ± 0.0031 (7.6%) |
| p+p (Run8) | ZDC \otimes BBC-tag | ± 0.0060 (10.3%) |
| p+p (Run8) | ZDC \otimes BBC-veto | ± 0.0028 (11.4%) |
| p+p (Run15) | ZDC inclusive | ± 0.0051 (15.9%) |
| p+p (Run15) | ZDC \otimes BBC-tag | ± 0.0042 (9.6%) |
| p+p (Run15) | ZDC \otimes BBC-veto | ± 0.0033 (31.3%) |
| p+Au (Run15) | ZDC inclusive | ± 0.0020 (1.5%) |
| p+Au (Run15) | ZDC \otimes BBC-tag | ± 0.0038 (24.3%) |
| p+Au (Run15) | ZDC \otimes BBC-veto | ± 0.0072 (3.6%) |
| p+Al (Run15) | ZDC inclusive | ± 0.0035 (32.0%) |
| p+Al (Run15) | ZDC \otimes BBC-tag | ± 0.0033 (6.7%) |
| p+Al (Run15) | ZDC \otimes BBC-veto | ± 0.0052 (8.2%) |

Table 5.12: Systematic uncertainties from beam position.

5.11.5 Calibrations

Systematic uncertainties from the calibrations (ZDC gain, SMD gain, and SMD threshold) are studied in by varying calibration parameter. For the ZDC gain, asymmetry is measured for the 35-135 GeV and 45-145 GeV, and the difference in A_N is assigned as an uncertainty. For the SMD gain, all gain parameters are set to be equal and the change of the A_N is assigned as the systematic uncertainty. For the SMD threshold, the threshold is varied. Then the uncertainties are quadratically summed. The results are summarized in Tab. 5.13.

| Data set | sample | <i>syst.</i> |
|----------|------------------------|----------------------|
| p+p | ZDC inclusive | ± 0.0027 (5.0%) |
| p+Au | ZDC inclusive | ± 0.0042 (2.7%) |
| p+Al | ZDC inclusive | ± 0.0012 (9.2%) |
| p+p | ZDC \otimes BBC-tag | ± 0.0010 (1.5%) |
| p+Au | ZDC \otimes BBC-tag | ± 0.0085 (56.8%) |
| p+Al | ZDC \otimes BBC-tag | ± 0.0042 (7.4%) |
| p+p | ZDC \otimes BBC-veto | ± 0.0067 (21.7%) |
| p+Au | ZDC \otimes BBC-veto | ± 0.0062 (2.6%) |
| p+Al | ZDC \otimes BBC-veto | ± 0.0042 (5.8%) |

Table 5.13: Systematic uncertainties from calibrations.

Chapter 6

Result

Figure 6.1 shows the final result. The x-axis corresponds to the atomic mass number A , 1, 27, and 197 for $p+p$, $p+Al$, and $p+Au$ collisions, respectively, and the y-axis corresponds to the measured A_N . Different colors (or shapes) indicate different trigger sample, ZDC inclusive (red), ZDC \otimes BBC-tag (green), and ZDC \otimes BBC-veto (blue) samples. The color bars represent systematic uncertainties, and the statistical uncertainties are smaller than the marker size. The 3% global (scale) uncertainty for polarization is not included. For better visibility, data points are shifted horizontally. The data values with uncertainty sources are summarized in Tab 6.1.

The A_N results are consistent with the previous PHENIX publication [3] for $p+p$ collisions, $A_N = -0.061 \pm 0.010(\text{stat}) \pm 0.007(\text{syst})$ for the ZDC-inclusive sample and $A_N = -0.075 \pm 0.004(\text{stat}) \pm 0.007(\text{syst})$ for ZDC \otimes BBC-tag. The systematic uncertainties in 2015 data are larger than those of the previous publication, mainly because the charge veto counter was not operated in 2015 $p+p$ whereas it was previously. Also, the beam position uncertainty is more conservatively assigned in 2015.

Table 6.1: A_N for forward neutron production in $p+p$, $p+Al$, and $p+Au$ collisions, for ZDC inclusive, ZDC \otimes BBC-tag, and ZDC \otimes BBC-veto samples.

| | $p+p$ | | | $p+Al$ | | | $p+Au$ | | |
|---------------------|-------------|-------------|-------------|---|---|---|---|---|---|
| | Inclusive | BBC Tag | BBC Veto | Inclusive | BBC Tag | BBC Veto | Inclusive | BBC Tag | BBC Veto |
| A_N | -0.054 | -0.064 | -0.031 | -0.013 | -0.057 | 0.073 | 0.157 | -0.015 | 0.234 |
| Stat. error | ± 0.001 | ± 0.002 | ± 0.004 | ± 0.002 | ± 0.003 | ± 0.003 | ± 0.002 | ± 0.005 | ± 0.002 |
| Syst. error: | | | | | | | | | |
| <i>Background</i> | ± 0.007 | ± 0.009 | ± 0.017 | -0.001 | -0.010 | +0.004 | +0.015 | -0.003 | +0.012 |
| <i>Smearing</i> | ± 0.002 | ± 0.003 | ± 0.001 | < 0.001 | ± 0.002 | ± 0.003 | ± 0.007 | < 0.001 | ± 0.010 |
| <i>Beam pos.</i> | ± 0.009 | ± 0.006 | ± 0.010 | ± 0.004 | ± 0.004 | ± 0.006 | ± 0.002 | ± 0.004 | ± 0.008 |
| <i>Polarization</i> | < 0.001 | < 0.001 | < 0.001 | < 0.001 | ± 0.002 | ± 0.003 | ± 0.011 | ± 0.001 | ± 0.017 |
| <i>Calibration</i> | ± 0.003 | ± 0.001 | ± 0.007 | ± 0.001 | ± 0.004 | ± 0.004 | ± 0.004 | ± 0.009 | ± 0.006 |
| <i>Total syst.</i> | ± 0.012 | ± 0.011 | ± 0.021 | $\begin{array}{c} +0.004 \\ -0.004 \end{array}$ | $\begin{array}{c} +0.007 \\ -0.012 \end{array}$ | $\begin{array}{c} +0.009 \\ -0.008 \end{array}$ | $\begin{array}{c} +0.020 \\ -0.014 \end{array}$ | $\begin{array}{c} +0.009 \\ -0.010 \end{array}$ | $\begin{array}{c} +0.025 \\ -0.022 \end{array}$ |

The A_N results of the ZDC inclusive sample show a clear A dependence. Compared to $p+p$ collisions, the sign of A_N is flipped and its magnitude becomes three times larger in $p+Au$. Furthermore, the A dependence appears differently between the different trigger samples. The A dependence becomes more remarkable in the ZDC \otimes BBC-veto sample; the A_N becomes even larger for $p+Au$ collisions, and the sign of A_N becomes positive in $p+Al$. On the other hand, in the ZDC \otimes BBC-tag sample, weak A dependence is observed. The sign of A_N stays negative, and approaches to zero for heavier nuclei.

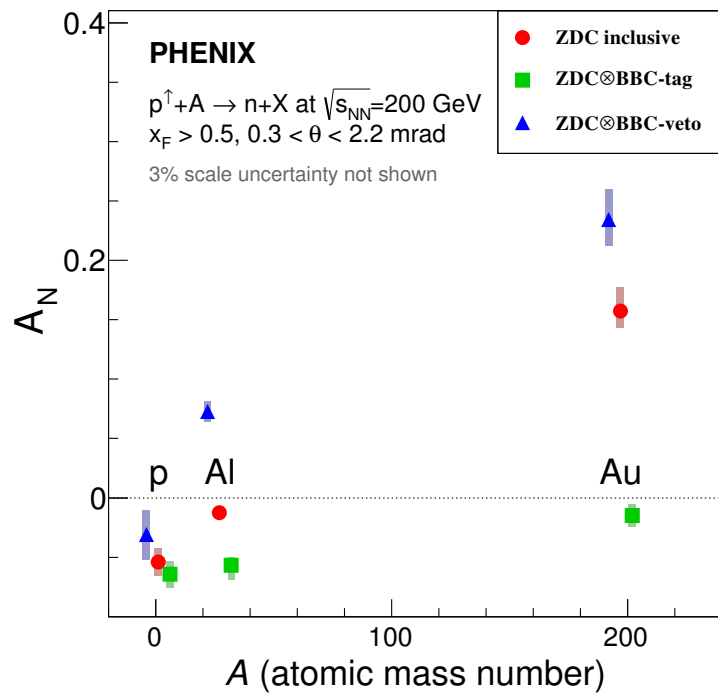


Figure 6.1: Forward neutron A_N in $p+A$ collisions for $A=1$ (p), 27 (Al) and 197 (Au), for ZDC inclusive (red), ZDC \otimes BBC-tag (green) and ZDC \otimes BBC-veto (blue) triggered samples; color bars show systematic uncertainties, statistical uncertainties are smaller than the marker size; Additional 3% scale uncertainty (not shown) is from polarization normalization. Some data points are shifted horizontally for better visibility.

Extra result without some corrections

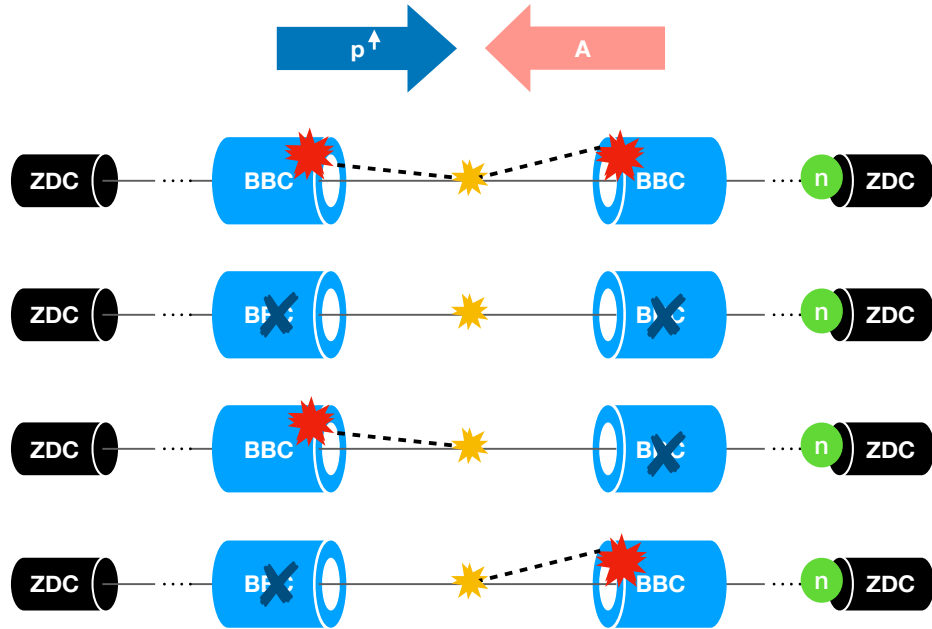


Figure 6.2: The illustration of BBC tagged samples. From the top to bottom, $ZDC \otimes BBC\text{-tag}$, $ZDC \otimes BBC\text{-veto}$, $ZDC \otimes p\text{-dir BBC-veto} \otimes A\text{-dir BBC-tag}$, and $ZDC \otimes p\text{-dir BBC-tag} \otimes A\text{-dir BBC-veto}$. The sum of these four samples becomes the ZDC inclusive sample. As indicated in the figure, the neutron A_N is analyzed by the right side ZDC, where the polarized proton beam is heading.

Figure 6.3 shows the result of two more BBC trigger samples. The $ZDC \otimes p\text{-dir BBC-veto} \otimes A\text{-dir BBC-tag}$ sample (magenta) requires a hit at only in nucleus beam going direction BBC and no hit at the proton going direction BBC, and vice versa (light blue). To clarify, the illustration of the BBC tagging is drawn in Fig 6.2. The analysis is different between the final result (Fig. 6.1) and this result (Fig. 6.3) for the smearing correction and the back-

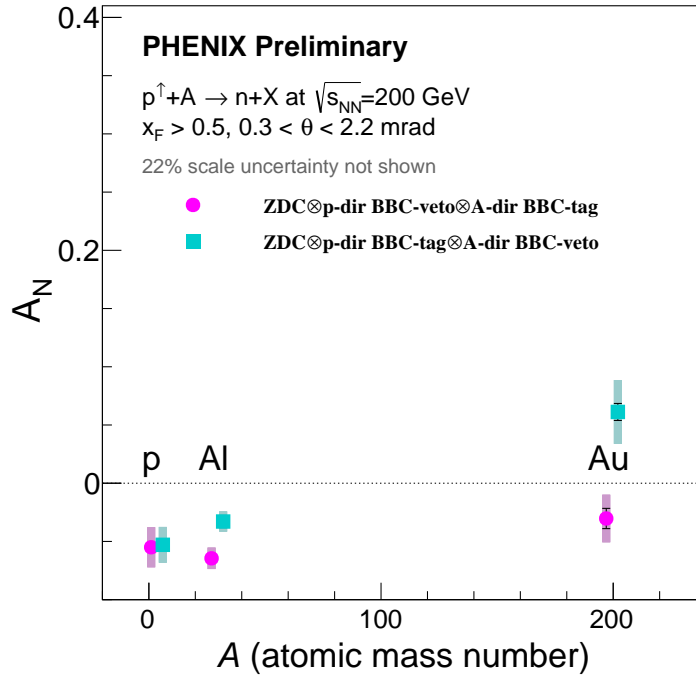


Figure 6.3: Forward neutron A_N as a function of atomic mass number in $p+A$ collisions like Fig. 6.1. Two more BBC tagged samples, ZDC \otimes p-dir BBC-veto \otimes A-dir BBC-tag (magenta) and ZDC \otimes BBC-tag (light blue) are analyzed. See the text for analysis differences.

ground subtraction. The smearing correction factor is $\sim 10\%$ smaller here for all the data points than the final value. Further charged background estimation will increase one side of the systematic uncertainty for $p+A$, and increase the magnitude of A_N for $p+p$, assuming zero A_N for background.

The A_N values of the ZDC \otimes p-dir BBC-veto \otimes A-dir BBC-tag sample is similar to those of the ZDC \otimes BBC-tag, having moderate nuclear dependence stays in negative. On the other hand, the ZDC \otimes p-dir BBC-tag \otimes A-dir BBC-veto sample shows different A dependence tendency from the other samples. The A dependence is clear. The $p+Au$ asymmetry becomes positive, but the magnitude is $\sim 30\%$ of the A_N of the ZDC inclusive sample.

Table 6.2 shows the raw yield of each sample which are used for the

| Sample | $p+p$ | $p+Al$ | $p+Au$ |
|--|-----------------------------|--------|--------|
| ZDC inclusive | 6.3 ($\times 10^6$ events) | 2.8 | 1.7 |
| ZDC \otimes BBC-tag | | 2.7 | 0.9 |
| ZDC \otimes BBC-veto | | 1.3 | 0.9 |
| ZDC \otimes p-dir BBC-veto \otimes A-dir BBC-tag | | 1.6 | 0.6 |
| ZDC \otimes p-dir BBC-tag \otimes A-dir BBC-veto | | 0.8 | 0.4 |
| | | | 0.2 |

Table 6.2: Raw yield of each sample in million. Background fractions are not subtracted. From $p+p$ to $p+Au$, one can clearly notice that the fraction of the ZDC \otimes BBC-veto sample becomes increased, whereas the fraction of the ZDC \otimes BBC-tag and the ZDC \otimes p-dir BBC-veto \otimes A-dir BBC-tag samples becomes decreased. The fraction of the ZDC \otimes p-dir BBC-tag \otimes A-dir BBC-veto sample is not changed significantly.

A_N calculation. Background fractions are not subtracted. From $p+p$ to $p+Au$, one can clearly notice that the fraction of the ZDC \otimes BBC-veto sample increases, whereas the fraction of the ZDC \otimes BBC-tag and the ZDC \otimes p-dir BBC-veto \otimes A-dir BBC-tag samples decrease. The fraction of the ZDC \otimes p-dir BBC-tag \otimes A-dir BBC-veto sample does not change significantly.

Chapter 7

Discussions

The overall result is surprising because the naive prediction based on a Regge theory model expected moderate A dependence of A_N , staying in negative sign. The requirement of the BBC-veto in A -going direction seems to play a key role to shift the A_N from negative to positive as the atomic mass goes higher. This requirement enhances the event samples which keep the nucleus stay intact in the collision process. This can be translated to some bias to low momentum transfer reactions. Such behaviors are characteristics of electromagnetic (EM) processes. Therefore, neutron production from EM processes is intensively discussed.

7.1 Regge theory model

The precise theory calculation [13] was done after this data analysis. The result is shown in Fig. 7.1. The green (red) data points and the dashed (solid) theory curve correspond to the ZDC \otimes BBC-tag (ZDC \otimes p-dir BBC-veto \otimes A--

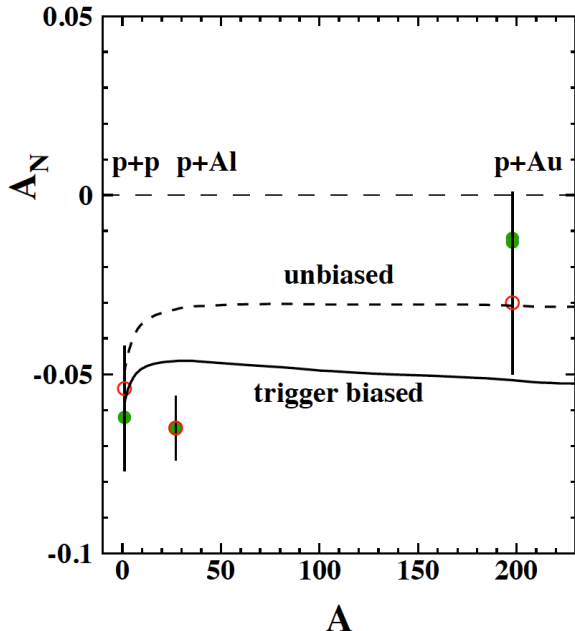


Figure 7.1: Theory calculation [13] of the forward neutron A_N as a function of atomic mass number A drawn with the data points. The green (red) data points and the dashed (solid) theory curve correspond to the ZDC \otimes BBC-tag (ZDC \otimes p-dir BBC-veto \otimes A-dir BBC-tag) sample.

dir BBC-tag) sample. The A dependence comes from the absorption of the final state neutron into the nucleus. As a result, this theory reproduces the data quite well up to tendency, however, not precisely. The inconsistency between $p+Al$ data and theory is not understood. The difference may come from nuclear effects which are not considered. However, there is no known nuclear effect which increases the A_N . The A_N also show saturated behavior as nuclear mass increases. This may imply impact of gluon saturation.

7.2 Electromagnetic process

Charged particles can collide through exchanging a virtual photon(s),

and particles can also be created as collision products of the virtual photon exchange. Since this electromagnetic (EM) interaction becomes dominant over hadronic interactions when particles collide at a distance larger than the sum of their nuclear radii, this types of collisions are called as the ultra-peripheral collision (UPC) [83]. Although neutron data in $p+p$ are explained without introducing EM processes, in case of $p+A$ collisions, as the charge Z of the nucleus increases, neutron production from EM processes should not be overlooked.

Neutron at the ZDC acceptance can be produced through the UPC [84]. In this case, the proton collides with the virtual photon emitted from the nucleus, and then the neutron is produced in the final state through nonresonant photo- π production or as a decay product of an excited state ($p+\gamma^* \rightarrow \Delta \rightarrow n + \pi^+ (+\dots)$). Since the virtual photon flux increases as Z^2 , this process occurs ~ 6400 times more frequently in case of the $p+Au$ collisions compare to the $p+p$ collisions.

Furthermore, in these processes, the nucleus does not break up, and the momentum transfer distribution decreases more rapidly compare to that of hadronic processes. As a result, neutrons from EM processes will be collected effectively in the $ZDC \otimes BBC$ -veto sample whereas vetoed in the $ZDC \otimes BBC$ -tag and $ZDC \otimes p\text{-dir}$ BBC -veto $\otimes A\text{-dir}$ BBC -tag samples. Therefore, investigating neutron A_N in EM processes will be definitely interesting.

Indeed, spin asymmetries in EM processes were measured in multiple fixed target experiments previously. In low energy photon beam experiments [16, 85, 86] with transversely polarized proton targets, asymmetries in $\gamma+p \rightarrow \pi+N$ are measured. Overall asymmetries were sensitive to the pion emitting polar angle (in the γp center of mass frame) and the beam energy. In case of $\gamma+p \rightarrow \pi^+ + n$, positive^I A_N are observed for pion [16, 86], up to $\sim 80\%$, at γp center of mass $W < 1.35\text{GeV}/c^2$. This can be found in Fig. 7.2, which

^IHere, the sign of A_N is defined according to the fixed target, therefore, it is opposite when applied to our case. So, positive pion $A_{N\text{target}} =$ negative counterpart neutron $A_{N\text{target}} =$ positive counterpart neutron $A_{N\text{protonbeam}}$.

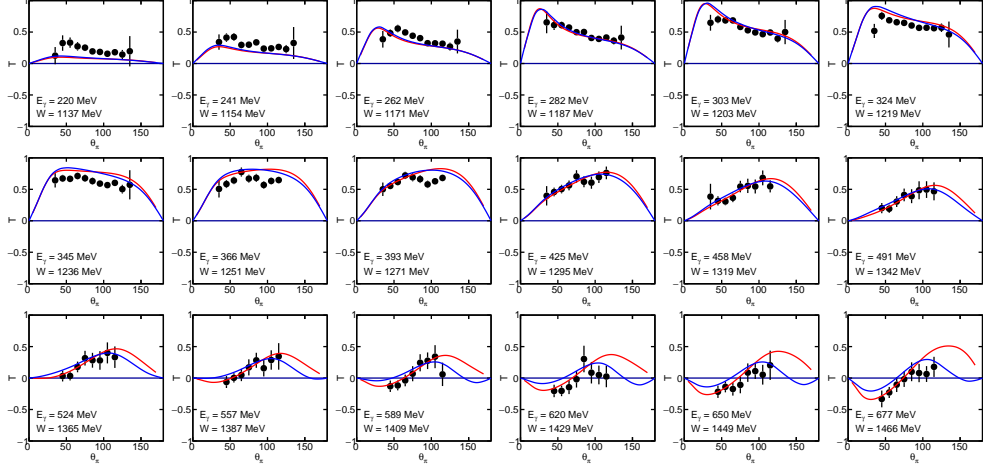


Figure 7.2: A_N ($=T$) of π^+ production in $\gamma p \rightarrow \pi^+ n$ reaction as a function of pion production polar angle in the γp center of mass frame for various photon beam energies. Plots show a comparison with the MAID2007 [14] (red) and the Osaka-Argonne [15] (blue) models with the PHOENICS data [16] (black dots).

shows the PHOENICS Data [16] drawn with two phenomenological analysis fits [14, 15]. Model dependences are only seen in high invariant mass region.

The A_N in EM processes is claimed to have observed in the 185 GeV polarized proton beam induced EM process with a fixed Pb target ($\sqrt{s} = 19$ GeV) at Fermilab [17]. In this process, the pion is produced as a decay product of a resonance which is induced when a Coulomb field of a nucleus excites the beam proton ($p + \gamma^* \rightarrow \Delta \rightarrow \pi^0 + p$). Figure 7.3 shows the invariant mass spectrum of the $\pi^0 + p$ at small $t < 10^{-3} \text{GeV}/c^2$, where EM process can play relatively important role with respect to hadronic processes. Peaks correspond to the $\Delta(1232)$ and $N(1520)$ resonances. The A_N is zero at the region I ($W < 1.36 \text{ GeV}/c^2$), whereas $A_N \sim -60\%$ at the region II ($1.36 < W < 1.52 \text{ GeV}/c^2$), interference region of those two resonances. The pion emitting angle corresponds to 60-120 degrees.

Similar behavior can be found in the low energy $\gamma + p \rightarrow \pi^0 + p$ data as shown in Fig. 7.4. The magnitudes of A_N between 1.36-1.52 GeV center

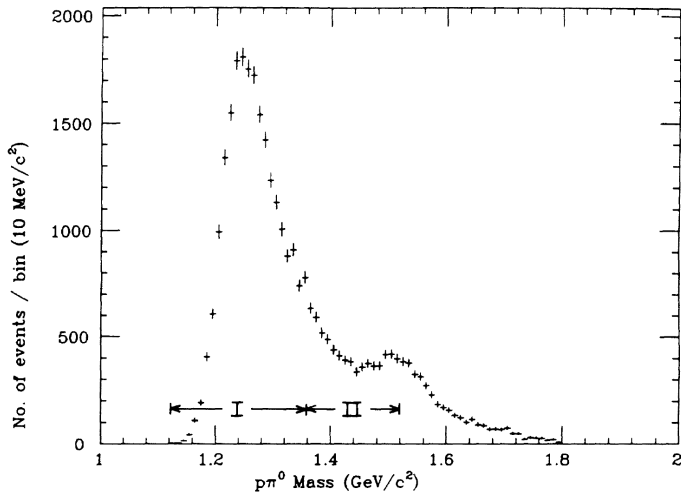


Figure 7.3: The invariant mass spectrum [17] of the $\pi^0 + p$ at $t < 10^{-3} \text{ GeV}/c^2$. Peaks correspond to the $\Delta(1232)$ and $N(1520)$ resonances. The A_N is zero at the region I ($W < 1.36 \text{ GeV}/c^2$), whereas $A_N \sim 60\%$ at the region II ($1.36 < W < 1.52 \text{ GeV}/c^2$), interference region of those two resonances.

of mass energies are significantly larger than those in the below 1.36 GeV. Therefore, since virtual photon from UPC has low virtuality, we may consider simulating the A_N result with low energy $\gamma p \rightarrow \pi^+ n$ into our kinematics.

This case is studied in a recently published paper [18]. The forward neutron production through EM processes for the $n + \pi^+$ as the final state is simulated. Here, the neutron cross sections in $p+\text{Au}$ ($p+\text{Al}$) collisions at our analysis kinematics are calculated for the EM and hadronic processes as 19.6 mb (0.7 mb) and 19.2 mb (8.3 mb), respectively. Neutrons produced through EM processes mostly come from the Δ^+ decay ($p + \gamma^* \rightarrow \Delta^+ \rightarrow n + \pi^+$). It turned out that in case of the $p+\text{Au}$ collisions, the contribution from the UPC becomes significant. Also, 94% of the final state pion flies off nearly along the beamline, passes the inner hole of the BBC detector. Therefore, the EM processes are mostly contained in the ZDC \otimes BBC-veto sample, which shows a strong A dependence. This explains some tendency of our raw neutron yield in Table 6.2. The increase of the fraction of ZDC \otimes BBC-veto samples in larger nuclei can be considered as increased contribution from the UPC,

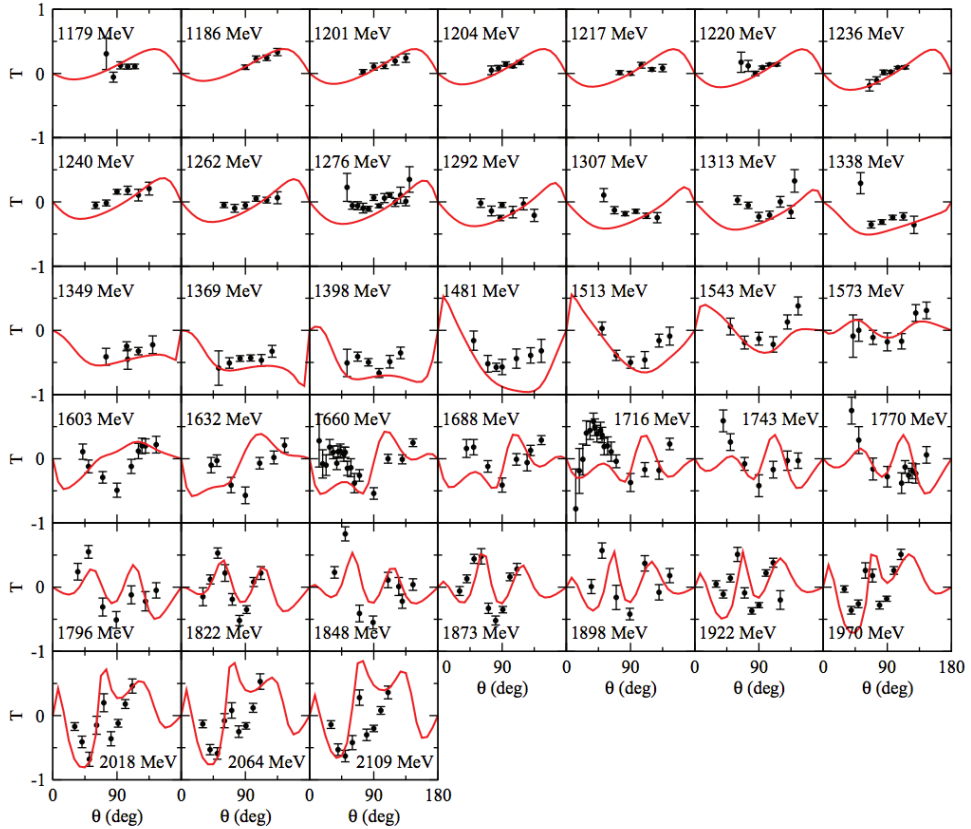


Figure 7.4: A_N ($=T$) of π^0 production in $\gamma p \rightarrow \pi^+ n$ reaction as a function of pion production polar angle in the γp center of mass frame for various photon beam energy (center of mass energy is shown in each plot). Plots show a comparison with the combined data from the particle data group (PDG) and the Osaka-Argonne model [15].

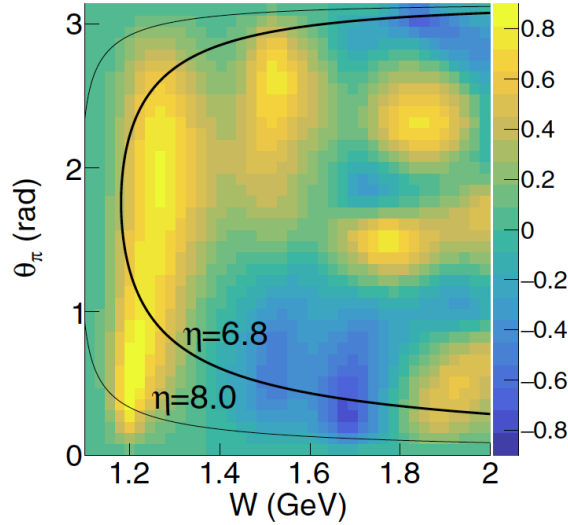
although the exact UPC fraction in each sample is not estimated yet.

The A_N of the EM processes are also calculated based on the MAID2007 model [14], a photo/electro pion production phenomenology, which well reproduces the $\gamma N \rightarrow \pi N$ experiment data as shown in Fig. 7.2. The top plot in the Fig. 7.5 shows the pion A_N as a function of W and the polar angle of π^+ in the $\gamma^* p$ center of mass frame for $Q^2 = 0$. The kinematic region corresponding to our neutron data is included between the two black curves. From this figure, one can notice that the large A_N of pion, therefore, of coun-

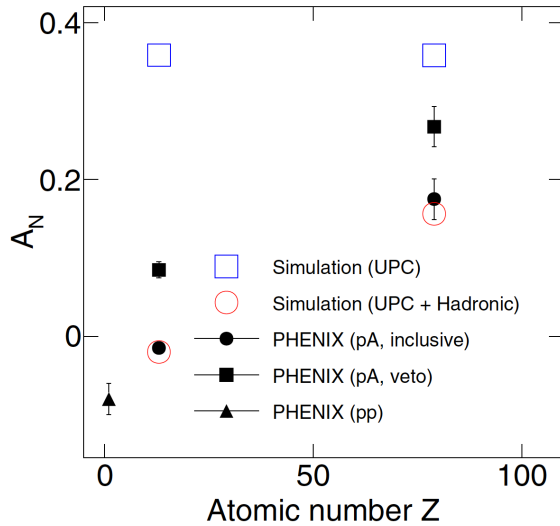
terpart neutron, comes from $W \sim 1.2$ GeV region, which is around the Δ^+ resonance. This large positive mainly A_N mainly comes from the interference between the M_{1+} transition amplitude (dominant amplitude in the Δ^+ resonance invariant mass) and the E_{0+} transition amplitude (nonresonance term) [18].

In the same paper [18], the ZDC inclusive A_N is calculated as a cross section weighted A_N sum of the hadronic process (Regge theory) and the UPC process. The A_N values for hadronic processes in $p+A$ collisions are taken from the Regge theory calculation [56]. The result is shown in Fig. 7.5. As a result, this simulation reproduces our ZDC inclusive A_N result very well. The overall uncertainty of this simulation mainly comes from two pion production (14%) and Q^2 range (10%).

Therefore, the EM process is the strongest candidate which explains the observed strong A dependence currently. In order to enhance this argument, further cross check should be done. Comparison with the cross section of data and the sum of simulated UPC and Regge theory cross sections will let us know that if our neutron sample can be explained by the Regge theory and the UPC mainly. Also, comparing the p_T dependent A_N or x_F dependent A_N shapes data with theory will be interesting because A_N from both UPC and Regge theory are expected to have different p_T and x_F dependencies. Due to steeper fall of EM amplitude as a function of p_T , steeper fall of EM A_N a function of p_T can be expected. Also, the A_N measurement as a function of x_F in $p+p$ [3] indicates almost no x_F dependence on A_N in hadronic processes, whereas neutrons from Δ decay concentrate around $x_F \sim 0.9$ [18], therefore, A_N as a function of x_F of the UPC will be largest around $x_F \sim 0.9$ and small in lower x_F .



(a) A_N of π^+ as a function of γ^*p invariant mass and pion production angle in the lab frame. Z-axis shows A_N .



(b) The predicted A_N of UPC (open square) only and UPC+hadronic (open circle). The hadronic A_N is taken from the Regge theory calculation [56]. This model reproduced the ZDC inclusive data well.

Figure 7.5: The A_N calculation from the UPC simulation ($\gamma^*p \rightarrow \pi^+n$) using the MAID2007 model [18].

7.3 Other contributors?

By separating the EM and hadronic processes, the A_N has a form as

$$A_N \propto \text{Im} [\phi_{\text{EM}}^{\text{non-flip}} \phi_{\text{EM}}^{*\text{flip}} + \phi_{\text{EM}}^{\text{non-flip}} \phi_{\text{Had}}^{*\text{flip}} + \phi_{\text{Had}}^{\text{non-flip}} \phi_{\text{EM}}^{*\text{flip}} + \phi_{\text{Had}}^{\text{non-flip}} \phi_{\text{Had}}^{*\text{flip}}], \quad (7.1)$$

where EM and Had stand for the electromagnetic (EM) and hadronic processes, and $\phi^{\text{non-flip}}$ and ϕ^{flip} represent the spin non-flip and flip amplitudes. The A_N from the Regge theory corresponds to the last term (see Fig. 7.6a), and A_N from the UPC corresponds to the first term (see Fig. 7.6b). The $p+p$ result can be explained by the last term alone. Two terms in the middle has been ignored so far.

In case of the RHIC polarimeter, as mentioned in Sec. 4.1.9, the A_N in elastic $p+p \rightarrow p+p$ scattering in the CNI region comes from the interference between the pomeron exchange and the photon exchange, which corresponds to two middle terms in Eq. 7.1 (see Fig. 7.6c). Therefore, we may investigate an interference between hadronic and EM processes as a contributor on A_N for our case. If a hadronic process has the same final state as electromagnetic processes, the nucleus (A) should remain intact, which means pomeron should be coupled to the nucleus. We can think of two cases shown in Fig. 7.7 for example. Since diffractive processes are characterized by a large rapidity gap, diffractive neutron production processes should not be overlooked.

To summarize, the observed A dependent A_N of the forward neutron production are well reproduced by the linear sum of the UPC and the hadronic processes. However their interference terms also can be contributed which were not yet addressed in the present study. Further detailed study such as x_F and p_T dependence are necessary to test the present hypothesis strictly. Further theoretical investigations are also necessary to establish complete understanding of possible competing mechanisms in the A_N .

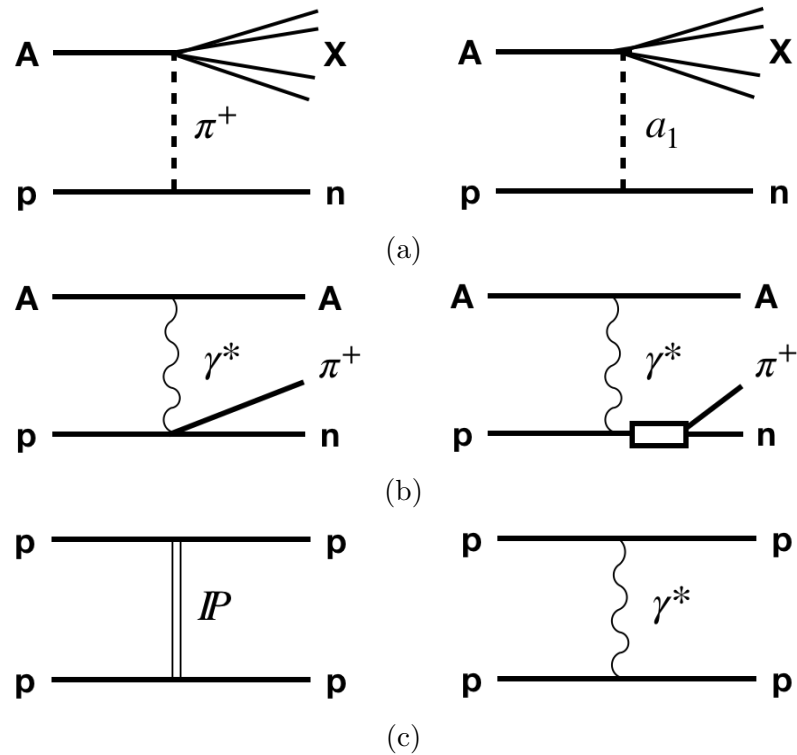


Figure 7.6: Feynman diagrams of two interfering mechanisms which generate A_N for neutron production in $p+A$ hadronic process (a), EM process (b), and for hadronic and EM processes in elastic $p+p$ scattering (c).

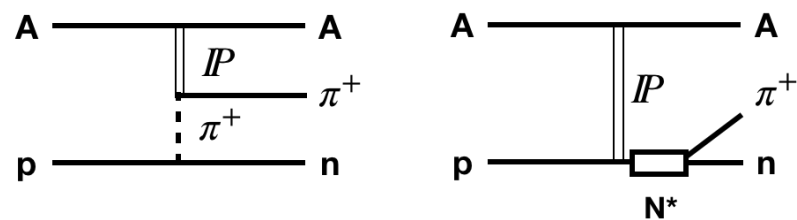


Figure 7.7: Example of hadronic processes which can have final state as same as those of EM processes, therefore may interfere.

Chapter 8

Conclusion

The forward neutron production in $p+p$ had been explained in the Regge framework. One of the Regge theory model which well explains neutron production in $p+p$ predicted moderate A dependence of A_N . In 2015, the nuclear dependence of A_N for forward neutron production was first measured in unprecedented polarized $p+A$ collisions at $\sqrt{s_{NN}} = 200$ GeV. In contrast with the Regge theory model prediction, unexpected strong nuclear dependence on A_N was observed, accompanied by sign flip. In order to pin down the unknown neutron production mechanism, we investigated a correlation between charged particle production at lower rapidity. When we require rapidity gaps, the nuclear dependence becomes even more enhanced. This behavior is a signature of low Q^2 interaction. Recent UPC study well explains our observation, its enhancement in the rapidity gap sample and A_N result. Therefore, UPC process is a strong candidate which explains the nuclear dependence of A_N . However, there are still unexplored mechanisms which can be enhanced in the rapidity gap sample. Further data analysis such as cross section measurement may confirm our current theory.

Bibliography

- [1] A. Donnachie and P.V. Landshoff. Total cross sections. *Physics Letters B*, 296(1):227 – 232, 1992.
- [2] W. Flauger and F. Monnig. Measurement of inclusive zero-angle neutron spectra at the cern isr. *Nuclear Physics B*, 109(2):347 – 356, 1976. ISSN 0550-3213.
- [3] A. Adare et al. Inclusive cross section and single transverse spin asymmetry for very forward neutron production in polarized $p+p$ collisions at $\sqrt{s} = 200$ GeV. *Phys. Rev. D*, 88(3):032006, 2013.
- [4] E. C. Aschenauer et al. The RHIC Cold QCD Plan for 2017 to 2023: A Portal to the EIC. arXiv:1602.03922.
- [5] M. M. Mondal. Measurement of the Transverse Single-Spin Asymmetries for π^0 and Jet-like Events at Forward Rapidities at STAR in $p+p$ Collisions at $\sqrt{s} = 500$ GeV. *Proc. Sci.*, DIS2014:216, 2014.
- [6] Y. Fukao et al. Single Transverse-Spin Asymmetry in Very Forward and Very Backward Neutral Particle Production for Polarized Proton Collisions at $\sqrt{s} = 200$ GeV. *Phys. Lett. B*, 650:325–330, 2007.
- [7] B. Z. Kopeliovich, I. K. Potashnikova, I. Schmidt, and J. Soffer. Single transverse spin asymmetry of forward neutrons. *Phys. Rev. D*, 84:114012, 2011.

- [8] A. Zelenski, G. Atoian, D. Raparia, J. Ritter, and D. Steski. The rhic polarized h^+ ion source. *Review of Scientific Instruments*, 87(2):02B705, 2016.
- [9] I Alekseev et al. Polarized proton collider at rhic. *Nuclear Instruments and Methods in Physics Research Section A: Accelerators, Spectrometers, Detectors and Associated Equipment*, 499(2):392 – 414, 2003.
- [10] A. Zelenski, A. Bravar, D. Graham, W. Haeberli, S. Kokhanovski, Y. Makdisi, G. Mahler, A. Nass, J. Ritter, T. Wise, and V. Zubets. Absolute polarized h-jet polarimeter development, for rhic. *Nuclear Instruments and Methods in Physics Research Section A: Accelerators, Spectrometers, Detectors and Associated Equipment*, 536(3):248 – 254, 2005.
- [11] J. Tojo et al. Measurement of analyzing power for proton-carbon elastic scattering in the coulomb-nuclear interference region with a 22– GeV/c polarized proton beam. *Phys. Rev. Lett.*, 89:052302, Jul 2002.
- [12] B. Z. Kopeliovich and T. L. Trueman. Polarized proton-nucleus scattering. *Phys. Rev. D*, 64:034004, Jun 2001.
- [13] B. Z. Kopeliovich, I. K. Potashnikova, and Ivan Schmidt. Nuclear effects in leading neutron production. [arXiv:1702.07708 \[hep-ex, physics:hep-ph, physics:nucl-ex\]](https://arxiv.org/abs/1702.07708), February 2017. arXiv: 1702.07708.
- [14] D. Drechsel, S. S. Kamalov, and L. Tiator. Unitary isobar model – maid2007. *The European Physical Journal A*, 34(1):69, Oct 2007.
- [15] H. Kamano, S. X. Nakamura, T.-S. H. Lee, and T. Sato. Nucleon resonances within a dynamical coupled-channels model of πn and γn reactions. *Phys. Rev. C*, 88:035209, Sep 2013.

- [16] H. Dutz et al. Photoproduction of positive pions from polarized protons. *Nuclear Physics A*, 601(3):319 – 332, 1996. ISSN 0375-9474.
- [17] D. C. Carey et al. Measurement of the Analyzing Power in the Primakoff Process With a High-energy Polarized Proton Beam. *Phys. Rev. Lett.*, 64:357, 1990.
- [18] Recently measured large a_n for forward neutrons in $p+a$ collisions at $\sqrt{s_{NN}} = 200$ gev explained through simulations of ultraperipheral collisions and hadronic interactions.
- [19] T. Regge. Introduction to complex orbital momenta. *Nuovo Cim*, 14: 951–976, 1959.
- [20] Alfred Tang and John W. Norbury. Properties of regge trajectories. *Phys. Rev. D*, 62:016006, Jun 2000.
- [21] Y. Nambu. The Confinement of Quarks. *Sci. Am.*, 235N5:48–70, 1976.
- [22] Leslie L. Foldy and Ronald F. Peierls. Isotopic spin of exchanged systems. *Phys. Rev.*, 130:1585–1589, May 1963.
- [23] Enrico Predazzi Vincenzo Barone. *High-Energy Particle Diffraction*. Springer-Verlag Berlin Heidelberg, 1 edition, 2002. ISBN 1864-5879.
- [24] D. d'Enterria, R. Engel, T. Pierog, S. Ostapchenko, and K. Werner. Constraints from the first LHC data on hadronic event generators for ultra-high energy cosmic-ray physics. *Astropart. Phys.*, 35(2):98, 2011.
- [25] K. H. Kampert and M. Unger. Measurements of the cosmic ray composition with air shower experiments. *Astropart. Phys.*, 35(10):660, 2012.
- [26] O. Adriani et al. Measurements of longitudinal and transverse momentum distributions for neutral pions in the forward-rapidity region with the LHCf detector. *Phys. Rev. D*, 94:032007, 2016.

- [27] J. Engler et al. Measurement of inclusive neutron spectra at the ISR. *Nucl. Phys. B*, 84(1):70, 1975.
- [28] W. Flauger and F. Monnig. Measurement of Inclusive Zero-Angle Neutron Spectra at the CERN ISR. *Nucl. Phys. B*, 109:347, 1976.
- [29] M. Derrick et al. Observation of events with an energetic forward neutron in deep inelastic scattering at hera. *Physics Letters B*, 384(1):388 – 400, 1996. ISSN 0370-2693.
- [30] S. Chekanov et al. Study of the pion trajectory in the photoproduction of leading neutrons at hera. *Physics Letters B*, 610(3):199 – 211, 2005. ISSN 0370-2693.
- [31] C. Adloff et al. Photoproduction with a leading proton at hera. *Nuclear Physics B*, 619(1):3 – 21, 2001. ISSN 0550-3213.
- [32] H1 Collaboration and C. Adloff et al. Measurement of leading proton and neutron production in deep-inelastic scattering at hera. *The European Physical Journal C - Particles and Fields*, 6(4):587–602, Jan 1999.
- [33] B. Kopeliovich, B. Povh, and I. Potashnikova. Deep-inelastic electro-production of neutrons in the proton fragmentation region. *Z. Phys. C*, 73:125, 1996.
- [34] N. N. Nikolaev, W. Schäfer, A. Szczurek, and J. Speth. Do the E866 Drell-Yan data change our picture of the chiral structure of the nucleon? *Phys. Rev. D*, 60:014004, May 1999.
- [35] A. B. Kaidalov, V. A. Khoze, A. D. Martin, and M. G. Ryskin. Leading neutron spectra. *Eur. Phys. J. C*, 47:385, 2006.
- [36] B. Z. Kopeliovich, I. K. Potashnikova, Ivan Schmidt, and J. Soffer. Damping of forward neutrons in pp collisions. *Phys. Rev. D*, 78:014031, Jul 2008.

- [37] R. D. Klem, J. E. Bowers, H. W. Courant, H. Kagan, M. L. Marshak, E. A. Peterson, K. Ruddick, W. H. Dragoset, and J. B. Roberts. Measurement of Asymmetries of Inclusive Pion Production in Proton-Proton Interactions at 6 and 11.8 GeV/ c . *Phys. Rev. Lett.*, 36:929, 1976.
- [38] W. H. Dragoset, J. B. Roberts, J. E. Bowers, H. W. Courant, H. Kagan, M. L. Marshak, E. A. Peterson, K. Ruddick, and R. D. Klem. Asymmetries in Inclusive Proton-Nucleon Scattering at 11.75 GeV/ c . *Phys. Rev. D*, 18:3939, 1978.
- [39] J. Antille, L. Dick, L. Madansky, D. Perret-Gallix, M. Werlen, A. Gonidec, K. Kuroda, and P. Kyberd. Spin Dependence of the Inclusive Reaction $p + p$ (POLARIZED) $\rightarrow \pi^0 + X$ at 24 GeV/ c for High- p_T π^0 Produced in the Central Region. *Phys. Lett. B*, 94:523, 1980.
- [40] S. Saroff et al. Single-Spin Asymmetry in Inclusive Reactions $p^\uparrow + p \rightarrow \pi^+ + X, \pi^- + X$, and $p + X$ at 13.3 and 18.5 GeV/ c . *Phys. Rev. Lett.*, 64:995, 1990.
- [41] C. E. Allgower et al. Measurement of analyzing powers of π^+ and π^- produced on a hydrogen and a carbon target with a 22-GeV/ c incident polarized proton beam. *Phys. Rev. D*, 65:092008, 2002.
- [42] D. L. Adams et al. Analyzing power in inclusive π^+ and π^- production at high $x(F)$ with a 200 GeV polarized-proton beam. *Phys. Lett. B*, 264:462, 1991.
- [43] D. L. Adams et al. First results for the two-spin parameter A_{LL} in π^0 production by 200 GeV polarized protons and antiprotons. *Phys. Lett. B*, 261:197, 1991.
- [44] D. L. Adams et al. Measurement of single spin asymmetry in η -meson production in $p^\uparrow p$ and $\bar{p}^\uparrow p$ interactions in the beam fragmentation region at 200 GeV/c. *Nucl. Phys. B*, 510:3, 1998.

- [45] I. Arsene et al. Single-Transverse-Spin Asymmetries of Identified Charged Hadrons in Polarized $p p$ Collisions at $\sqrt{s} = 62.4$ GeV. *Phys. Rev. Lett.*, 101:042001, 2008.
- [46] B. I. Abelev et al. Forward Neutral-Pion Transverse Single-Spin Asymmetries in $p + p$ Collisions at $\sqrt{s} = 200$ GeV. *Phys. Rev. Lett.*, 101: 222001, 2008.
- [47] L. Adamczyk et al. Transverse Single-Spin Asymmetry and Cross Section for π^0 and η Mesons at Large Feynman x in $p^\uparrow + p$ Collisions at $\sqrt{s} = 200$ GeV. *Phys. Rev. D*, 86:051101(R), 2012.
- [48] A. Adare et al. Measurement of transverse-single-spin asymmetries for midrapidity and forward-rapidity production of hadrons in polarized $p + p$ collisions at $\sqrt{s} = 200$ and 62.4 GeV. *Phys. Rev. D*, 90(1):012006, 2014.
- [49] S. Heppelmann et al. Large p_T Forward Transverse Single Spin Asymmetries of π^0 Mesons at $\sqrt{s} = 200$ and 500 GeV from STAR. *Proc. Sci.*, DIS2013:240, 2013.
- [50] A. Adare et al. Cross section and transverse single-spin asymmetry of η mesons in $p^\uparrow + p$ collisions at $\sqrt{s} = 200$ GeV at forward rapidity. *Phys. Rev. D*, 90:072008, 2014.
- [51] Dennis Sivers. Single-spin production asymmetries from the hard scattering of pointlike constituents. *Phys. Rev. D*, 41:83–90, Jan 1990.
- [52] John Collins. Fragmentation of transversely polarized quarks probed in transverse momentum distributions. *Nuclear Physics B*, 396(1):161 – 182, 1993. ISSN 0550-3213.
- [53] Jianwei Qiu and George Sterman. Single transverse-spin asymmetries in hadronic pion production. *Phys. Rev. D*, 59:014004, Nov 1998.

- [54] Y. Kanazawa and Yuji Koike. Chiral-odd contribution to single-transverse spin asymmetry in hadronic pion production. *Physics Letters B*, 478(1):121 – 126, 2000. ISSN 0370-2693.
- [55] M. H. Kim. Analysisstatus: A_N of very forward π^0 production, Nov 2018.
- [56] B. Z. Kopeliovich, I. K. Potashnikova, and I. Schmidt. Leading Neutrons From Polarized Proton-Nucleus Collisions. *AIP Conf. Proc.*, 1819(1):050002, 2017.
- [57] D. Boer, A. Dumitru, and A. Hayashigaki. Single transverse-spin asymmetries in forward pion production at high energy: Incorporating small- x effects in the target. *Phys. Rev. D*, 74:074018, 2006. doi: 10.1103/PhysRevD.74.074018.
- [58] D. Boer and A. Dumitru. Polarized hyperons from pA scattering in the gluon saturation regime. *Phys. Lett. B*, 556:33, 2003.
- [59] D. Boer, A. Utermann, and E. Wessels. The saturation scale and its x -dependence from λ polarization studies. *Phys. Lett. B*, 671:91, 2009.
- [60] Z.-B. Kang and F. Yuan. Single spin asymmetry scaling in the forward rapidity region at RHIC. *Phys. Rev. D*, 84:034019, 2011.
- [61] Y. V. Kovchegov and M.D. Sievert. New mechanism for generating a single transverse spin asymmetry. *Phys. Rev. D*, 86:034028, 2012.
- [62] J.-W. Qiu. Transverse Single-spin Asymmetry in pA Collisions. In *RIKEN/RBRC Workshop: Forward Physics at RHIC*, volume 111, page 741, 2012.
- [63] Anatoli Zelenski, Grigor Atoian, V Davydenko, Alexander Ivanov, Anton Kolmogorov, J Ritter, D Steski, and Vlad Zubets. The rhic polarized source upgrade. 295:012147, 05 2011.

- [64] Chris Gardner et al. Operation of the RHIC Injector Chain with Ions from EBIS. In *6th International Particle Accelerator Conference (IPAC 2015)*, 2015, page THPF046, 2015.
- [65] L.H. Thomas B.A. I. the kinematics of an electron with an axis. *The London, Edinburgh, and Dublin Philosophical Magazine and Journal of Science*, 3(13):1–22, 1927.
- [66] V. Bargmann, Louis Michel, and V. L. Telegdi. Precession of the polarization of particles moving in a homogeneous electromagnetic field. *Phys. Rev. Lett.*, 2:435–436, May 1959.
- [67] K. Adcox et al. Phenix detector overview. *Nuclear Instruments and Methods in Physics Research Section A: Accelerators, Spectrometers, Detectors and Associated Equipment*, 499(2):469 – 479, 2003. ISSN 0168-9002. The Relativistic Heavy Ion Collider Project: RHIC and its Detectors.
- [68] S.H. Aronson et al. Phenix magnet system. *Nuclear Instruments and Methods in Physics Research Section A: Accelerators, Spectrometers, Detectors and Associated Equipment*, 499(2):480 – 488, 2003. The Relativistic Heavy Ion Collider Project: RHIC and its Detectors.
- [69] M. Aizawa et al. Phenix central arm particle id detectors. *Nuclear Instruments and Methods in Physics Research Section A: Accelerators, Spectrometers, Detectors and Associated Equipment*, 499(2):508 – 520, 2003. ISSN 0168-9002. The Relativistic Heavy Ion Collider Project: RHIC and its Detectors.
- [70] L Aphecetche et al. Phenix calorimeter. *Nuclear Instruments and Methods in Physics Research Section A: Accelerators, Spectrometers, Detectors and Associated Equipment*, 499(2):521 – 536, 2003. ISSN

- 0168-9002. The Relativistic Heavy Ion Collider Project: RHIC and its Detectors.
- [71] K. Adcox et al. Phenix central arm tracking detectors. *Nuclear Instruments and Methods in Physics Research Section A: Accelerators, Spectrometers, Detectors and Associated Equipment*, 499(2):489 – 507, 2003. ISSN 0168-9002. The Relativistic Heavy Ion Collider Project: RHIC and its Detectors.
- [72] M. Allen et al. Phenix inner detectors. *Nuclear Instruments and Methods in Physics Research Section A: Accelerators, Spectrometers, Detectors and Associated Equipment*, 499(2):549 – 559, 2003. ISSN 0168-9002. The Relativistic Heavy Ion Collider Project: RHIC and its Detectors.
- [73] H. Akikawa et al. Phenix muon arms. *Nuclear Instruments and Methods in Physics Research Section A: Accelerators, Spectrometers, Detectors and Associated Equipment*, 499(2):537 – 548, 2003. The Relativistic Heavy Ion Collider Project: RHIC and its Detectors.
- [74] C. Adler, A. Denisov, E. Garcia, M. J. Murray, H. Strobele, and S. N. White. The RHIC zero degree calorimeters. *Nucl. Instrum. Methods Phys. Res., Sec. A*, 470:488, 2001.
- [75] C. Liu et al. RHIC Operation with Asymmetric Collisions in 2015. In *7th International Particle Accelerator Conference (IPAC 2016)*, 2016, page TUPMW038, 2016.
- [76] PHENIX Collaboration, C. Aidala, et al. Nuclear Dependence of the Transverse-Single-Spin Asymmetry for Forward Neutron Production in Polarized $p+A$ Collisions at $\sqrt{s_{NN}} = 200$. *Phys. Rev. Lett.*, 120(2):022001, January 2018.

- [77] T. Sjöstrand et al. High-energy-physics event generation with PYTHIA6.1. *Comp. Phys. Comm.*, 135(2):238, 2001.
- [78] R. Brun et al. GEANT Detector Description and Simulation Tool. CERN-W-5013, Geneva (1994).
- [79] K. Imai N. Saito K.Tanida M. Togawa G. Bunce, Y. Goto and S. White. Measurements of the leading neutron production in polarized pp collision at $\sqrt{s} = 200$ GeV. PHENIX Analysis Note.
- [80] RHIC polarization for Runs 9–12. RHIC Polarimetry Group, RHIC/CAD Accelerator Physics Note 490 (2013).
- [81] W. Schmidke, private communication.
- [82] John Koster Seishi Dairaku, Yuji Goto. Phenix local polarimeter analysis in polarized proton-proton collisions at $\text{sqrt}s = 200$ gev from rhic run-6 and run-8. PHENIX analysis note an929, 2010.
- [83] Carlos A. Bertulani, Spencer R. Klein, and Joakim Nystrand. Physics of ultra-peripheral nuclear collisions. Annual Review of Nuclear and Particle Science, 55(1):271–310, 2005.
- [84] G. Mitsuka. Forward hadron production in ultra-peripheral proton-heavy-ion collisions at the LHC and RHIC. Eur. Phys. J. C, 75(12):614, 2015.
- [85] M. Fukushima, N. Horikawa, R. Kajikawa, H. Kobayakawa, K. Mori, T. Nakanishi, C.O. Pak, S. Suzuki, T. Matsuda, N. Tokuda, M. Daigo, and T. Ohshima. Measurement of polarized target asymmetry on $\hat{1}^3\text{p}$ – $\hat{1}^1\text{o}$ p below 1 gev. Nuclear Physics B, 136(2):189 – 200, 1978. ISSN 0550-3213.
- [86] M. Fukushima, N. Horikawa, R. Kajikawa, H. Kobayakawa, K. Mori, T. Nakanishi, C.O. Pak, S. Suzuki, T. Matsuda, N. Tokuda, M. Daigo,

and T. Ohshima. Measurement of polarized target asymmetry in $\hat{1}^3p \rightarrow \hat{1}+n$ below 1.02 gev. Nuclear Physics B, 130(3):486 – 504, 1977. ISSN 0550-3213.

Appendix A

Appendix

A.1 Asymmetry calculations

A.1.1 Fill/run raw asymmetry ϵ_N

$\epsilon_N(\phi)$, raw asymmetry of neutrons to azimuthal angle ϕ and $\phi+\pi$ is calculated as

$$\epsilon_N(\phi) = \frac{\sqrt{N_\phi^\uparrow N_{\phi+\pi}^\downarrow} - \sqrt{N_\phi^\downarrow N_{\phi+\pi}^\uparrow}}{\sqrt{N_\phi^\uparrow N_{\phi+\pi}^\downarrow} + \sqrt{N_\phi^\downarrow N_{\phi+\pi}^\uparrow}} \quad (\text{A.1})$$

where N_ϕ^\uparrow ($N_{\phi+\pi}^\downarrow$) is the number of events which passed analysis cuts, measured at angle ϕ ($\phi + \pi$) with the proton beam polarization up (down).

Its statistical uncertainty is calculated as

$$\sigma_{\epsilon_N}(\phi) = \frac{\sqrt{N_\phi^\uparrow N_{\phi+\pi}^\downarrow N_\phi^\downarrow N_{\phi+\pi}^\uparrow}}{(\sqrt{N_\phi^\uparrow N_{\phi+\pi}^\downarrow} + \sqrt{N_\phi^\downarrow N_{\phi+\pi}^\uparrow})^2} \sqrt{\frac{1}{N_\phi^\uparrow} + \frac{1}{N_{\phi+\pi}^\downarrow} + \frac{1}{N_\phi^\downarrow} + \frac{1}{N_{\phi+\pi}^\uparrow}} \approx \frac{2\sqrt{2}}{\sqrt{N_{total}}} \quad (\text{A.2})$$

where N_{total} is total number of neutron (≈ 2 (spin) $\times 16$ (ϕ) $\times N_\phi^\uparrow$) used for asymmetry calculation.

Figure 5.17 shows hit ϕ and $\phi + \pi$ acceptance for each $\epsilon_N(\phi)$ calculation. Measured asymmetry $\epsilon_N(\phi)$ is fitted to

$$\epsilon_N(\phi) = \varepsilon_N \sin(\phi - \phi_0) \quad (\text{A.3})$$

where ϕ_0 is a free parameter to get maximum ε_N .

A.1.2 Fill/run polarization P

Polarization P is read from spin table in the spin database. For Run8, fill P , $\sigma_P^{stat.}$, and $\sigma_P^{syst.}$ are provided whereas for Run15, run P and $\sigma_P^{stat.}$ are provided. We use $\sigma_P = \sqrt{(\sigma_P^{stat.})^2 + (\sigma_P^{syst.})^2}$ for Run8 fill A_N^{fit} calculation, and $\sigma_P = \sigma_P^{stat.}$ for Run15 run A_N^{fit} calculation.

A.1.3 Measured asymmetry A_N^{fit}

For convenience of representation, we define variables for raw asymmetry divided by polarization as

$$\mathcal{A}_N^{\text{fit}}(\phi) \equiv \frac{\epsilon_N(\phi)}{P}, \quad (\text{A.4})$$

and

$$A_N^{\text{fit}} \equiv \frac{\varepsilon_N}{P}. \quad (\text{A.5})$$

Then in the same fill/run,

$$\mathcal{A}_N^{\text{fit}}(\phi) = A_N^{\text{fit}} \sin(\phi - \phi_0). \quad (\text{A.6})$$

We assumed A_N^{fit} should be independent of fill/run. However, we calculated

A_N^{fit} separately for Run8 and Run15 $p+p$ as they can be different because of different running condition, such as 1 dead channel of SMD during Run8, and different background ratio from different beam condition.

We calculated fill/run averaged A_N^{fit} and uncertainties as follows.

1. Average $\mathcal{A}_N^{\text{Meas.,}i}(\phi)$

For i -fill/run, we calculated $\mathcal{A}_N^{\text{Meas.,}i}(\phi)$ as follows (i : fill/run index):

value as

$$\mathcal{A}_N^{\text{Meas.,}i}(\phi) = \frac{\epsilon_N^i(\phi)}{P^i} \quad (\text{A.7})$$

fill/run non-correlated statistical uncertainty (from PHENIX data statistics) as

$$\sigma_{\mathcal{A}_N^{\text{Meas.,}i}}^{\text{stat.}}(\phi) = \frac{1}{P^i} \sigma \epsilon_N^i(\phi) \quad (\text{A.8})$$

fill/run non-correlated systematic uncertainty (from fill/run polarization statistics (and systematic)) as

$$\sigma_{\mathcal{A}_N^{\text{Meas.,}i}}^{\text{syst.}}(\phi) = \frac{|\epsilon_N^i(\phi)|}{(P^i)^2} \sigma P^i \quad (\text{A.9})$$

fill/run total non-correlated uncertainty as

$$\sigma_{\mathcal{A}_N^{\text{Meas.,}i}}^{\text{non-corr.}}(\phi) = \sqrt{(\sigma_{\mathcal{A}_N^{\text{Meas.,}i}}^{\text{stat.}}(\phi))^2 + (\sigma_{\mathcal{A}_N^{\text{Meas.,}i}}^{\text{syst.}}(\phi))^2}, \quad (\text{A.10})$$

and weight for average $\mathcal{A}_N^{\text{fit}}(\phi)$ calculation as

$$w^i(\phi) = \frac{1}{(\sigma_{\mathcal{A}_N^{\text{Meas.,}i}}^{\text{non-corr.}}(\phi))^2} \quad (\text{A.11})$$

Then, we calculated average $\mathcal{A}_N^{\text{fit}}(\phi)$ as

$$\mathcal{A}_N^{\text{fit}}(\phi) = \frac{\sum_i w^i(\phi) \mathcal{A}_N^{\text{Meas.,} i}(\phi)}{\sum_i w^i(\phi)}, \quad (\text{A.12})$$

$$\sigma_{\mathcal{A}_N^{\text{fit}}}^{\text{stat.}}(\phi) = \sqrt{\frac{1}{N} \frac{\sum_i w^i(\phi) (\sigma_{\mathcal{A}_N^{\text{Meas.,} i}}^{\text{stat.}}(\phi))^2}{\sum_i w^i(\phi)}}. \quad (\text{A.13})$$

and

$$\sigma_{\mathcal{A}_N^{\text{fit}}}^{\text{syst.}}(\phi) = \sqrt{\frac{1}{N} \frac{\sum_i w^i(\phi) (\sigma_{\mathcal{A}_N^{\text{Meas.,} i}}^{\text{syst.}}(\phi))^2}{\sum_i w^i(\phi)}}. \quad (\text{A.14})$$

2. Average A_N^{fit}

We fit $\mathcal{A}_N^{\text{fit}}(\phi) \pm \sigma_{\mathcal{A}_N^{\text{fit}}}^{\text{stat.}}(\phi)$ histogram to a sine (equation A.5) to obtain A_N^{fit} , $\sigma_{A_N^{\text{fit}}}^{\text{stat.}}$, ϕ_0 , and σ_{ϕ_0} .

Then $\sigma_{A_N^{\text{fit}}}^{\text{syst.}}$ is calculated as

$$\sigma_{A_N^{\text{fit}}}^{\text{syst.}} = \frac{\pi}{16 \cos(\phi_0)} \sum \sigma_{\mathcal{A}_N^{\text{fit}}}^{\text{syst.}}(\phi) \quad (\text{A.15})$$

for 8 ϕ bins.

A.1.4 Charged background subtracted asymmetry A_N^S for Run-08

$$\text{Charge veto : } A_{N, cv}^{\text{fit}} = (1 - r_{cv}) A_N^S + r_{cv} A_N^B \quad (\text{A.16})$$

$$\text{Nocharge veto : } A_{N, x}^{\text{fit}} = (1 - r_x) A_N^S + r_x A_N^B \quad (\text{A.17})$$

where r is r_{eff} in section.

Then

$$A_N^S = \frac{r_x A_{N,cv}^{\text{fit}} - r_{cv} A_{N,x}^{\text{fit}}}{r_x - r_{cv}} \quad (\text{A.18})$$

$$A_N^B = \frac{-(1 - r_x) A_{N,cv}^{\text{fit}} + (1 - r_{cv}) A_{N,x}^{\text{fit}}}{r_x - r_{cv}} \quad (\text{A.19})$$

and uncertainties are

$$(\sigma_{A_N^S}^{\text{stat.}})^2 = \frac{(r_x \sigma_{A_{N,cv}^{\text{fit}}}^{\text{stat.}})^2 + (r_{cv} \sigma_{A_{N,x}^{\text{fit}}}^{\text{stat.}})^2}{(r_x - r_{cv})^2} \quad (\text{A.20})$$

$$(\sigma_{A_N^S}^{\text{syst.}})^2 = \frac{(A_{N,x}^{\text{fit}} - A_{N,cv}^{\text{fit}})^2 [(r_x \sigma_{r_{cv}})^2 + (r_{cv} \sigma_{r_x})^2]}{(r_x - r_{cv})^4} \quad (\text{A.21})$$

$$(\sigma_{A_N^B}^{\text{stat.}})^2 = \frac{[(1 - r_x) \sigma_{A_{N,cv}^{\text{fit}}}^{\text{stat.}}]^2 + [(1 - r_{cv}) \sigma_{A_{N,x}^{\text{fit}}}^{\text{stat.}}]^2}{(r_x - r_{cv})^2} \quad (\text{A.22})$$

$$(\sigma_{A_N^B}^{\text{syst.}})^2 = \frac{(A_{N,x}^{\text{fit}} - A_{N,cv}^{\text{fit}})^2 \{ [(1 - r_x) \sigma_{r_{cv}}]^2 + [(1 - r_{cv}) \sigma_{r_x}]^2 \}}{(r_x - r_{cv})^4}. \quad (\text{A.23})$$

A.1.5 Run-15 A_N^S

For Run-15, using A_N^B of Run-08,

$$A_{N,15}^S = \frac{A_{N,15}^{\text{fit}} - r_{15} A_N^B}{1 - r_{15}} \quad (\text{A.24})$$

and uncertainties are

$$(\sigma_{A_{N,15}^S}^{\text{stat.}})^2 = \frac{1}{(1 - r_{15})^2} (\sigma_{A_{N,15}^{\text{fit}}}^{\text{stat.}})^2 \quad (\text{A.25})$$

$$(\sigma_{A_{N,15}^S}^{syst.})^2 = \frac{(A_{N,15}^{\text{fit}} - A_N^B)^2}{(1 - r_{15})^4} (\sigma_{r_{15}}^2)^2 + \frac{(r_{15})^2}{(1 - r_{15})^2} (\sigma_{A_N^B}^{syst.})^2 + \frac{(r_{15})^2}{(1 - r_{15})^2} (\sigma_{A_N^B}^{stat.})^2 \quad (\text{A.26})$$

A.1.6 A_N

For point-to-point A_N ,

$$A_N = \frac{A^S}{C_{smear}}, \quad (\text{A.27})$$

$$\sigma_{A_N}^{stat.} = \frac{\sigma_{A_N^S}^{stat.}}{C_{smear}}, \quad (\text{A.28})$$

and

$$\sigma_{A_N}^{syst.} = |A_N| \frac{\sqrt{\sum_i (\sigma_{i-th syst.}^{\text{percent value}})^2}}{100} \quad (\text{A.29})$$

where i is an index runs over sources of systematic uncertainties.

국문초록

고에너지 강입자(hadron) 충돌시 대부분의 에너지는 충돌하는 입자가 향하던 방향 근처(전방: forward)에 생성되는 입자(들)가 가져간다. 그러므로 전반적인 입자 생성 과정을 이해하는데에 있어 전방 입자 생성 과정의 연구는 매우 중요하다. 그러나, 전방 입자의 경우 운동량 이동이 적은 충돌에서 생성되었기 때문에 양자색역학(Quantum Chromodynamics: QCD)의 적용이 어려워 그 생성과정을 잘 모르고 있다. 이렇게 운동량 이동이 적은 고에너지 충돌에서 일어나는 현상은 레제(Regge) 이론으로 활발히 연구하고 있다.

양성자-양성자 충돌에서 생성되는 전방 중성자의 경우 ISR과 PHENIX에서 생성 단면적(cross-section)이 측정되었고, IP12와 PHENIX에서 횡단-단일-스핀 비대칭도(A_N , -1과 1사이)가 측정되었다. 실험 결과는 레제 이론에서 양성자가 파이온(pion)이나 $a_1(1260)$ 을 교환하여 중성자를 생성하는 것으로 측정값을 잘 설명해왔다. 같은 이론이 양성자-원자핵 충돌의 경우, 중성자 생성의 A_N 가 원자핵의 종류에 따라 크게 변하지 않을 것으로 예상하였다.

2015년, RHIC에서 세계 최초로 스핀 편광된 양성자-원자핵(알루미늄, 금) 충돌 실험을 진행하였다. 이 실험에서 최초로 중성자 생성시 A_N 의 원자핵 상관성을 PHENIX에서 측정한 결과를 보고한다. 측정 결과는 놀랍게도 기존의 레제 이론과 완전히 달리, 강한 원자핵 상관성을 보였다. 양성자-금 충돌시의 A_N 값은 양성자-양성자 충돌시 A_N 값과 반대 부호를 가지며 그 크기도 세배나 되었다. 알려지지 않은 중성자 생성의 원리를 이해하기 위한 추가적인 측정과 결과를 설명할 수 있는 새로운 중성자 생성 과정에 대한 논의도 소개한다.

주요어: 전방 중성자, 스핀 비대칭, 양성자-원자핵 충돌, 릭, 피닉스, 레제, UPC

학번: 2014-30999

Acknowledgement

I think most people will understand that giving an exhaustive acknowledgement is nearly impossible. Especially those who spent tremendous time together and gave lots of supports won't have enough gratitude as I admit, and I may forget to mention very important people. Anyway, I will try.

First of all, I appreciate my thesis supervisors at Seoul National Univ. (SNU), Dr. Kiyoshi Tanida and Prof. Seonho Choi. Dr. Tanida gave me an opportunity to participate in the PHENIX experiment, always gave a support I need. Whenever we had a discussion, I could learn a lot from his knowledge with his clear explanation. After he left SNU, he continued to supervise my research regularly. Prof. Choi became my supervisor at SNU after Dr. Tanida left. Although I didn't spend lots of time with him, he provided me support and advice whenever I needed.

I also appreciate people from the RIKEN radiation lab. Dr. Hideto En'yo gave me an opportunity to join his group through the International Program Associate program of RIKEN. He led the group and provided great support for research life. Also, I appreciate current and former RIKEN PHENIX spin group members, Dr. Yuji Goto, Dr. Itaru Nakagawa, Dr. Ralf Seidl, Dr. Seyoung Han, Mr. Takeru Iguri, Dr. Taebong Moon, Mr. Toru Nagashima, Dr. Chong Kim, Mr. Minho Kim, Mr. Junsang Park, Dr. Sanghwa Park, and Dr. Inseok Yoon for having discussions and spending a lot of time together. I wouldn't complete my thesis without valuable comments from this group.

Especially, I spent the most of time with Dr. Nakagawa. He supervised my thesis and gave a lot of essential comments. I could learn a lot not only from his knowledge of research, but also from his attitude. I appreciate his encouragement and care of students. Dr. Goto gave me a lot of useful comments from his previous experiment of forward neutron research. I could learn a lot from Dr. Seidl's about spin physics from his comments in meetings. I give a special thank to Ms. Keiko Suzuki for her great assistance for life at RIKEN.

I appreciate two PPG members which are not mentioned in the above. I appreciate Dr. Alexander Bazilevsky for his significant contribution in this research. His comments in various aspect of research was very precious. Without him, I don't know how much more time would be spent to finish this analysis. I appreciate Prof. Doug Fields for his great leadership as a run coordinator in Run-15. Frequent and casual communication with him could accelerate this discovery.

I cannot miss these ZDC people from the acknowledgement. I'm more than glad that I could work with Dr. John Haggerty. I learned a lot about operation from his explanation in details. I also appreciate useful comments about ZDC hardware from Dr. Mickey Chiu and Dr. Cheng-Yi Chi, and Dr. Manabu Togawa.

I also appreciate to PHENIX computing experts. I appreciate Dr. Martin Purschke, Dr. Chris Pinkenburg, and Dr. Edmond Desmond for their tremendous 24 hours of help. Without their help, I wouldn't get a preliminary result that fast and life at 1008 would be tougher.

I appreciate Dr. Chuyu Liu and CAD crews for providing special stores for dedicate local pol runs. Their success was a crucial contribution of this research.

I also appreciate those who involves in theoretical discussion or giving an introduction. I appreciate Dr. Boris Kopeliovich, Dr. Kazunori Itakura, and Dr. Laszlo L. Jenkovszky for their explanation of the Regge theory. Especially, Dr. Kopeliovich is the one who calculated the forward neutron

asymmetry of PHENIX. Discussion with him was crucial to find a direction. I appreciate Dr. Aron M. Bernstein for his more than crucial comment of A_N from electromagnetic process. I appreciate Dr. Gaku Mitsuka for his excellent study of electroproduction of forward neutron. His research was very crucial in the discussion part.

I also appreciate Dr. Ciprian Gal and Dr. Sanghoon Lim for helping me settle down to PHENIX. I appreciate Dr. Seongbae Yang, Mr. Jaeyong Lee, and Mr. Taejin Moon to help me practice thesis defense.

Finally, I appreciate my grand mother and parents, who raised me with their best efforts.